SIGNATURES OF PLANETS IN THE OBSERVABLE STRUCTURE OF CIRCUMSTELLAR DEBRIS DISKS

By

MARK C. WYATT

A DISSERTATION PRESENTED TO THE GRADUATE SCHOOL
OF THE UNIVERSITY OF FLORIDA IN PARTIAL FULFILLMENT
OF THE REQUIREMENTS FOR THE DEGREE OF
DOCTOR OF PHILOSOPHY

UNIVERSITY OF FLORIDA

1999

ACKNOWLEDGMENTS

The first person I would like to acknowledge is my supervisor, Stan Dermott, not only for his advice, encouragement, and influence on my work, but also for enticing me over to Florida in the first place — it has been a tremendous experience. Equally I would like to thank my supervisor at Queen Mary and Westfield College, Carl Murray, for inspiring me to continue with a career in Astronomy. Thanks are also due to the Fulbright commission for supporting me in my first year in Florida.

This dissertation is essentially an extension of the work that Stan Dermott and his Solar System Dynamics group have accomplished over the past 15 or so years in their efforts to model the zodiacal cloud. It is fair to say that this dissertation could not have been achieved without this foundation. I wish to thank all members of the group, past and present, especially Keith Grogan, for countless useful discussions.

Another person to whom I am indebted is Charlie Telesco, both for his direct input to the dissertation through our work on the HR 4796 disk, and for providing me with the opportunity to go observing with his Infrared Astrophysics group. The perspective I gained from this observing experience has been an essential part of my Ph.D. education. I acknowledge all of the members of the OSCIR observing team, especially Robert Piña and Scott Fisher, for taking the time to teach me the observing lore.

On a personal level, I would like to thank my parents for nourishing the gift of life in me. Most of all, I want to thank my fiancée, Maxine, with whom I have shared the last 8 years, and whose love and support throughout I could not have lived without. This dissertation is dedicated to her.

TABLE OF CONTENTS

Abstract of Dissertation Presented to the Graduate School
of the University of Florida in Partial Fulfillment of the
Requirements for the Degree of Doctor of Philosophy

SIGNATURES OF PLANETS IN THE OBSERVABLE STRUCTURE OF CIRCUMSTELLAR DEBRIS DISKS

By

Mark C. Wyatt

December 1999

Chairman: Stanley F. Dermott
Major Department: Astronomy

Recent advances in astronomical instrumentation have led to a vast increase in our knowledge of the environments of nearby stars. In particular, we are now able to image the thermal emission from the disks of dust around main sequence stars that may be the fossil remnants of planetary formation. These observations imply that the distribution of dust in the debris disks is neither smooth nor symmetrical; e.g., mid-infrared images of the disk of dust around the young A0V star HR 4796A show two lobes of emission, one of which may be $\sim 5\%$ brighter than the other. The observed structure of the debris disk in the solar system, i.e., the zodiacal cloud, also contains asymmetries: it has an offset center of symmetry, it is warped, and there is an asymmetric ring of dust co-orbiting with the Earth. Since the zodiacal cloud's asymmetries have been shown to be signatures of the gravitational perturbations of the solar system's planets, it is hoped that it may be possible to indirectly detect extrasolar planetary systems by their signatures in debris disk observations.

This dissertation uses the physical processes that affect the evolution of debris material in the solar system to create a generalized model for the evolution of circumstellar debris material. It then shows how planetary perturbations affect that evolution, thereby causing the signatures of planets seen in the structure of the zodiacal cloud. This model can be used to provide a quantitative interpretation of debris disk observations, and the necessary modeling techniques are demonstrated by their application to observations of the HR 4796 disk. As well as determining the large scale structure of the HR 4796 disk, the modeling shows how a small body ($> 10 M_{\oplus}$) in the HR 4796 system that is on an orbit with an eccentricity larger than 0.02 could be the cause of the observed brightness asymmetry. The modeling also shows that the disk's mid-IR emitting particles are hotter than black body (and therefore small), and discusses whether they are in the process of being blown out of the system by radiation pressure.

CHAPTER 1
INTRODUCTION

1.1 Motivation

One of the most consistent human endeavors since the dawn of time has been to understand the nature of the universe in which we live. We are constantly questioning how the universe, and especially life on Earth, came to be as it is. Essentially this is a search for an understanding of our place in the universe, which inevitably leads us to ponder whether life could exist elsewhere in the cosmos. Ever since the middle of the sixteenth century when the Copernican heliocentric model of the universe superseded the geocentric view, this search has been a humbling experience as we begin to grasp the gargantuan scale of the universe. The observational data obtained over the previous 450 years paints a picture of the universe as we see it today that places the Earth in a far more insignificant role than was previously imagined — we now know that not only is the Earth not the center of the universe, but neither is the Sun, since it is just one of an estimated 400 billion stars that make up the Milky Way, which is itself just one galaxy out of at least ~ 80 billion others in the universe.

However much we have learned about the nature of the universe, the search for life outside the confines of the Earth has so far proved fruitless. Even in the corner of the universe about which we have the most information, the solar system, the debate continues as to whether there is (or indeed has been) life in some form or another on Mars. The ocean under the frozen ices of Jupiter's moon Europa and the surface of Saturn's moon Titan also provide potential habitats for life in the solar system, possibilities that remain to be tested. However, the solar system is but a small portion of the universe. Since stars are supposed to have formed in the same manner as the Sun, and the solar system's planets are thought to be a byproduct of that formation process, this has led us to speculate that some of the $O(10^{22})$ stars in the universe could also have planets orbiting them, some of which may (past, present, or future) harbor life. Thus, it has been one of the holy grails of recent astronomy to find habitable planets (i.e., ones that could potentially support life) orbiting stars other than the Sun.

1.2 The Search for Extrasolar Planets

From an observational point of view, the direct detection of habitable planets around even the closest stars is beyond our current technological capabilities (Backman 1998; Woolf & Angel 1998). There are two reasons for this. First, technological constraints mean that until recently telescopes did not have the resolving power to see the regions around the stars where it was expected that planets would have formed. Even now, the regions close to the star (~ 1 AU) where we anticipate that terrestrial planets would form are obscured from view by the diffraction halo of the stellar image. Second, planets by definition do not have an internal source of energy, which means that they are not very bright — any light observed from them is either reflected or reprocessed starlight. Thus, planets are far dimmer than the photospheric emission from star about which they are orbiting and are too dim to be detected directly at present (Woolf & Angel 1998).

This led to the development of some ingenious techniques to indirectly detect the presence of planets around stars. The most productive of these techniques uses the gravitational effect of a planetary system on the position of a star relative to the barycenter of the star/planet system. This causes a wobble in the motion of the star relative to the Sun. This wobble can be detected in three ways: astrometric detection, by measuring the change in position of a star on the sky

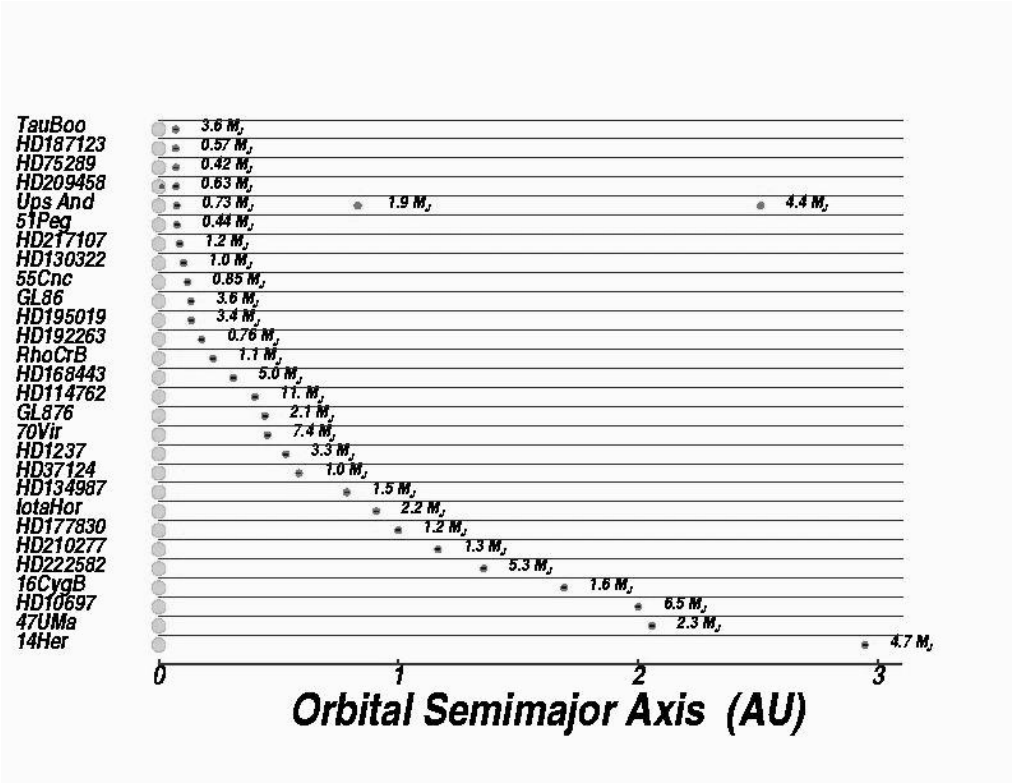

Figure 1.1: Known extrasolar planet candidates around Sun-like stars (Marcy et al. 1999).

(e.g., Gatewood 1987); doppler shift detection, by measuring the variation in the radial velocity of star (e.g., Mayor & Queloz 1995; Marcy & Butler 1998); by measuring variations in the time arrival of periodic signals, such as those from pulsars (e.g., Wolszczan & Frail 1992). There are also indirect detection methods that rely on the occurrence of specific events such as: the transit of a planet in front of a star that causes a reduction in the brightness of the star (e.g., a planet was recently discovered around the G0V star HD 209458 using this technique, Henry et al. 2000); and gravitational lensing of a background star by a foreground star/planet system. A complete review of all techniques is given in NASA's Road Map for the Exploration of Neighboring Planetary Systems (Beichman 1996).

The first extrasolar planetary system that was detected was that around a billion year old neutron star, the 6.2 ms pulsar PSR 1257+12 (Wolszczan & Frail 1992). This was followed three years later by the doppler shift detection of a 0.5 Jupiter mass planet orbiting 0.05 AU from the G2IVa star 51 Peg (Mayor & Queloz 1995). There have since been many other detections (not all of them confirmed), mostly using the doppler shift technique (e.g., Marcy & Butler 1998); there are currently 27 confirmed detections of extrasolar planets (see Fig. 1.1), with the number growing every month. However, none of these detections are of habitable planets. The doppler shift technique is biased towards detecting very massive planets (to get a wobble that is large enough to detect) that are also very close to the star (to detect the variation on a short enough timescale). All of the planets detected using this technique are larger than 0.4 Jupiter masses and most are found to orbit closer than 0.5 AU to the star (see Fig. 1.1). This means that this technique excludes the detection of systems like the solar system which we know to contain life. The planets that were detected around PSR 1257+12 are terrestrial mass planets. However, they are unlikely to harbor life due to the intensity of radiation from the pulsar.

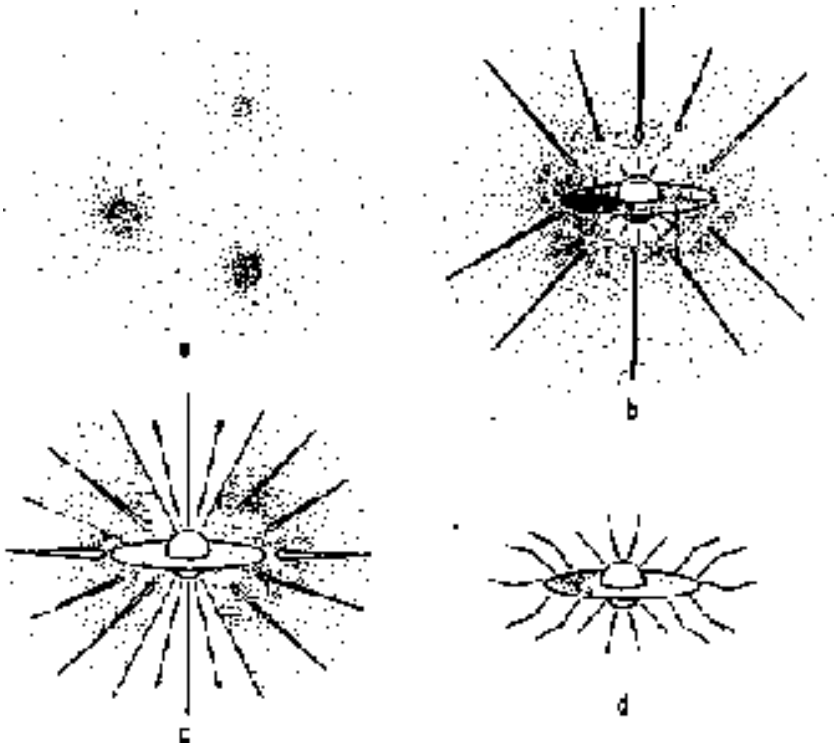

Figure 1.2: The four stages of star formation (Shu et al. 1987). (**a**) Clumps of gas and dust within molecular clouds collapse to form slowly rotating cloud cores. (**b**) A protostar with a surrounding nebula disk forms at the center of the cloud core collapsing from inside-out. (**c**) A stellar wind breaks out along the rotational axis of the system, creating a bipolar outflow. (**d**) The infall terminates, revealing a newly formed star with a circumstellar disk.

These detections have shown us that a solar planetary system-like configuration is not the only possible planetary system configuration, and they demand an explanation of how this diversity of planetary systems arose. Essentially we want to be able to answer questions like: How did these planetary systems form? Is a planetary system a likely outcome of stellar evolution? What are the other potential planetary systems like and what else is in the systems (such as asteroids and comets)? What are the implications for life in these systems? Since a planetary system is the end state of a long process that starts with the formation of a star from a cloud of gas and dust, this ultimately comes down to understanding how stars and their environments form and evolve. The following sections describe our current understanding of the physics behind the formation and evolution of both stars and their environments.

1.3 Paradigm of Star Formation

Star formation is relatively well-understood. Spectral energy distributions (SEDs) and images of young (pre main-sequence) stars, as well as observations of star forming regions provide a broad paradigm that describes how stars like the Sun formed from molecular clouds (e.g., Shu et al. 1987). This paradigm is outlined here; for further information on the nuances of this process, the reader is referred to the literature. Shu et al. (1987) describe four stages in the formation of a star from a molecular cloud (see Fig. 1.2). In the first stage (Fig. 1.2a), clumps of gas and dust in the cloud collapse to form slowly rotating cloud cores. When the mass of the clump exceeds a critical stability limit, the second stage is reached (Fig. 1.2b). This is characterized by dynamical

collapse of the clump from inside-out to form a central protostar with a surrounding accretion disk, both of which are deeply embedded within an infalling envelope of dust and gas. In the third stage (Fig. 1.2c), a stellar wind driven by convection in the protostar (which has by now started to burn deuterium) breaks out along the channels of weakest resistance, along the rotational axis of the system, causing collimated jets and bipolar outflows. The protostar is still accreting matter in this stage from the disk. Eventually, the infall terminates when the stellar wind has managed to sweep out the full 4π sr, leaving the fourth stage of the evolution (Fig. 1.2d): a star (e.g., a T-Tauri star) with a surrounding nebula disk. This disk then decays (possibly through the formation of planets or other stellar companions) as the star evolves onto the main sequence.

It is the latter stages that we are most interested in, since it is in these stages and in the nebula disk that the process of planetary formation is thought to occur. A variety of observations of nebula disks can provide important clues as to the physical conditions of these systems at the onset of planetary formation. Most inferences about the existence and nature of disks around young stars comes from observations of their SEDs. A strong infrared excess above that expected to arise from the stellar photosphere is an indication of thermal emission from dust grains in the disk that are heated by illumination from the star. There are several classes of SED, all of which can be accounted for using current models of the radiative transfer in nebula disks with different structures (see, e.g., Beckwith 1999). It turns out that to fit the SEDs, most of the disks need to have a cut-off both close to (a few stellar radii) and far from (O(100 AU)) the star, and to be flared. Some SEDs require an additional component to the star and disk (e.g., a remnant halo from the molecular cloud). Recently, there has been striking confirmation of these models of nebula disk structure from images of the disks (Burrows et al. 1996; Padgett et al. 1999); e.g., near-IR images of HH30 (Burrows et al. 1996), a star in the third stage of its evolution, show reflected starlight from the jets perpendicular to a dark disk seen edge-on with a gently flared shape, which causes illumination of the top edge of the disk.

The fraction of young stars with infrared excesses shows that $\sim$ 50% of young stars have disks (e.g., Strom et al. 1989), and sub-millimeter observations show that the mass of most disks is between 0.01 and $0.1 M_\odot$ (e.g., Beckwith et al. 1990). The minimum mass needed in the solar nebula to create the solar planetary system is $0.01 - 0.02 M_\odot$ (Hayashi 1981), thus if planets are formed in disks, there appears to be enough mass in the disks from which to make them (Beckwith & Sargent 1996). Observations of the fractions young stars with disks based on both their near-IR and far-IR excesses show that both the inner and outer regions of the disks dissipate between a few Myr and 10 Myr (see Beckwith 1999). Thus, any planetary formation should take place within this timescale. There is, however, little observational evidence of ongoing planetary formation in the disks, although authors have used SED observations to try to infer particle growth in these disks (see, e.g., Dent et al. 1998; Beckwith et al. 1999).

1.4 Paradigm of Planetary Formation

The planetary formation process is more poorly understood than star formation, since there is little observational evidence with which to test the theories. Most theories concentrate on describing how the current state of the solar system — i.e., the masses, orbits, bulk composition, and rotation of the planets, and the distribution of comets, asteroids, and meteoroids — resulted from the supposed conditions in the primitive solar nebula that are derived both from observations of other nebula disks, and from the current state of the solar system (Hayashi 1981). The theories also have to concur with information about the evolution of the young solar system from current observations, e.g., of cratering records. The current paradigm that explains how the solar system formed from the protosolar nebula is outlined here (for a good review, see Lissauer 1993).

The first stage of planetary formation is the formation of the stable protoplanetary disk, described in §1.3, which takes $\sim 10^5$ years from the onset of cloud collapse (Shu et al. 1993). This disk is a mixture of gas and solid matter, which is a mixture of interstellar grains and nebula condensates, both of which are small (submicron-sized). The composition of these condensates

depends on the temperature and composition of the gaseous disk (e.g., Pollack et al. 1994; Henning & Stognienko 1996). In the second stage, the microscopic grains settle towards the midplane of the disk due to gravity. During this sedimentation process, the grains collide and grow via pairwise accretion, which accelerates the settling process (Weidenschilling & Cuzzi 1993). The mechanical and chemical processes related to grain agglomeration are poorly understood, since they depend on sticking probabilities under conditions that are difficult to simulate in the laboratory. It is thought that the grains grow as fractal, or fluffy aggregates (e.g., Blum et al. 1999) similar to the interplanetary particles found in the solar system (Gustafson 1994). Collisions between cm-sized aggregates, however, can provide some compaction to the structure of the aggregates (Dominik & Tielens 1997). Small particles are coupled to the gas in the disk, but the large particles are not. The gas drag on meter-sized bodies is such that the material that survives to form planets completes the transition from cm- to km-size within $\sim 10^4$ years, which is the settling timescale.

In the third stage, gravitational interactions between pairs of km-sized planetesimals cause the planetesimals to conglomerate. These interactions result in coagulation because the orbits of the planetesimals have been circularized by gas drag resulting in low relative velocity collisions. Runaway growth of the largest planetesimal in an accretion zone occurs until protoplanets are dynamically isolated from one another. These protoplanets can merge further if their orbits are affected by either mutual gravitational interactions, or by tidal interactions with the gas disk (Goldreich & Tremaine 1980). Models of this phase of planetary formation show that accretion is not complete until $\sim 10^8$ years, but that planets attain a sizeable fraction of their mass within $\sim 10^7$ years (Wetherill 1980; Lissauer 1993). A fourth stage of evolution occurs for the planetesimals that are large enough to accrete substantial amounts of gas from the disk, thus forming Jovian gas giant planets. The existence of these giant planets, and their size and location, depend on how fast they grow relative to the dissipation of the gas disk, and their potential to halt (or enhance) their own growth via tidal interactions with this disk (e.g., Lin & Papaloizou 1979; Papaloizou & Terquem 1999). The formation of gas giants and the observed dissipation of the protoplanetary disks (Beckwith 1999) imply that protoplanetary cores probably develop within the first $\sim 10^6$ years. Current theories indicate that gas giants only form > 4 AU from the star due to the abundance of ice grains there (Boss 1995), while terrestrial rocky planets form inward of this.

While this paradigm is sufficient to explain the formation of the solar system, including the formation of the minor bodies (Lissauer 1993), it does not predict the formation of giant planets in orbits close to the star like those detected in exosolar systems (e.g., Marcy & Butler 1998; see Fig. 1.1). To explain these observations, the paradigms have to include more complicated physical processes. For example, a common theory is that these giant planets actually formed at ~ 5 AU from the star, but then suffered radial migration due to their gravitational interaction with the disk (Trilling et al. 1998; Papaloizou & Terquem 1999). It is evident, therefore, that the current theories of planetary formation are far from finalized, and that further observations of developing and developed planetary systems are needed to tell us how planets are really built. It is interesting to speculate, however, that if the paradigms of star and planetary formation hold true, then each star could have its own planetary system, or at least a failed planetary system.

1.5 Circumstellar Debris Disks

Observations of young stars showed that protoplanetary disks dissipate within $\sim 10^7$ years, supposedly due to planetary formation. This process was thought to leave a bare main sequence star, possibly with a planetary system orbiting it, and nothing but a very tenuous disk of debris material that was unable to form planets, if any at all. That all changed in 1983 when IRAS took routine calibration observations of the A0V star Vega[1]. The SED of Vega, just like those of younger stellar objects, showed a far-infrared excess above that expected from the stellar photosphere (Aumann et al. 1984; see Fig. 1.3). Limited spatial information about the 60 μm emission showed it to come

[1]The A0 is the star's temperature classification and V is its luminosity classification. An A0 star has $T_{eff} \approx 9500$ K and the V implies that the star is on the main sequence

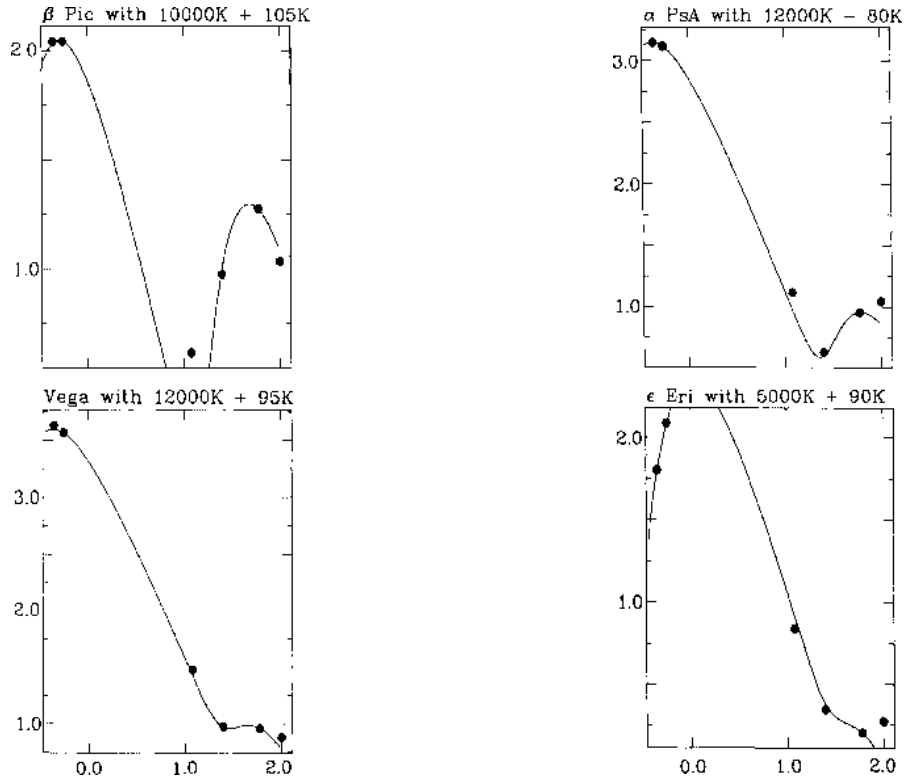

Figure 1.3: Observed energy distributions and black body fits to the photospheric emission and the infra-red excess emission for the four prototype debris disk stars (Walker & Wolstencroft 1988). Log (flux density in Jy) is plotted against log(wavelength in μm) for β Pictoris (top left), Fomalhaut (top right), Vega (bottom left), and ϵ Eridani (bottom right).

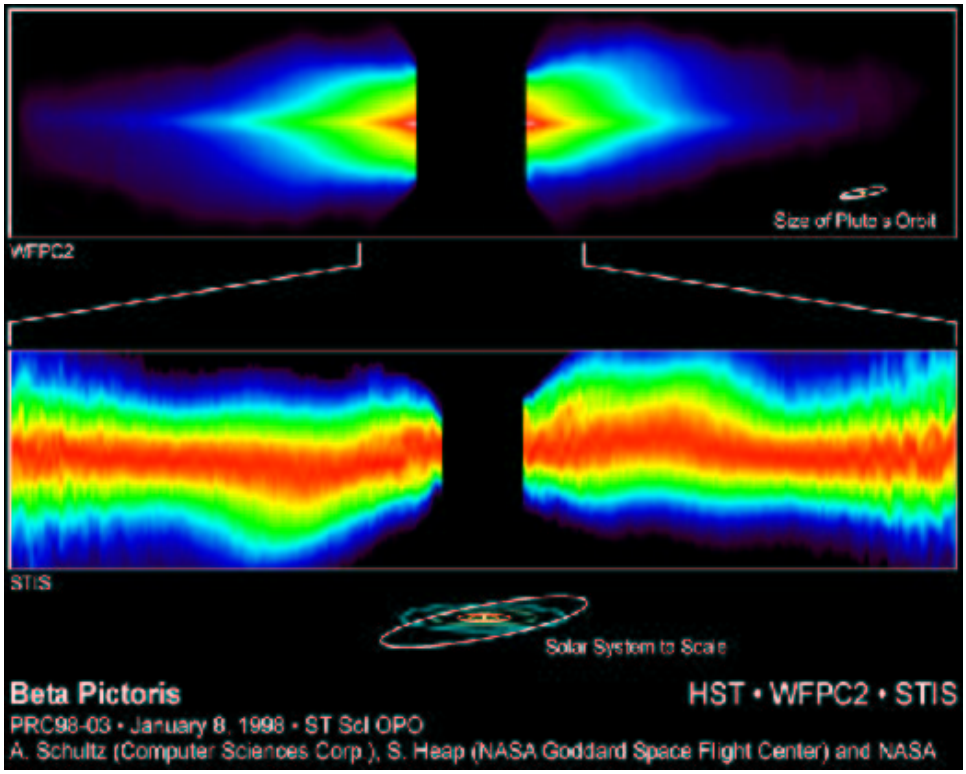

Figure 1.4: Hubble Space Telescope visible-light views of the edge-on disk of dust around the star β Pictoris (Schultz & Heap 1998).

from a region of diameter ~ 20 arcseconds (160 AU at 8 pc, the distance to Vega) around the star. Further, the shape of the SED was shown to be consistent with thermal emission from mm-sized material at 85 AU from the star that has been heated to $85 - 95$ K by the stellar radiation field. Subsequent IRAS observations of other main sequence stars in the solar region revealed that many of them have IR excesses similar to that of Vega (e.g., Aumann 1985; Walker & Wolstencroft 1988). After Vega, the next discoveries of infrared excesses were associated with the stars β Pictoris (A5V), Fomalhaut (A3V), and ϵ Eridani (K2V+), and these 4 stars have been dubbed the prototypes of this class (see Fig. 1.3). Recent analysis of the IRAS data found 108 stars with Vega-type excesses (Mannings & Barlow 1998). Thus it was shown that cool ($50-125$ K) solid matter is not uncommon around main sequence stars of a variety of ages and spectral types.

Stunning confirmation that this excess emission comes from material in orbit around the stars came soon after the IRAS observations with ground-based optical imaging of β Pictoris (Smith & Terrile 1984; see Fig. 1.4 for more recent images of the β Pictoris disk). Optical images taken using a coronographic spot to mask the bright stellar emission showed scattered light from a disk of material seen edge-on. Our understanding of the Vega-type disks as it stood in 1993 was summarized by Backman & Paresce (1993) who concentrated on interpreting observations of Vega, β Pictoris, and Fomalhaut. They concluded that the properties of these systems are very suggestive of planetary systems. The reasons they gave are: the infrared emitting grains are larger than interstellar grains; the material is orbiting, rather than falling into or away from, the star; the material is arranged in disks in the stellar equatorial planes; central regions similar in size to the solar planetary system are relatively lacking in small grains; and the rapid removal of the small grain population implies a reservoir of larger undetected parent bodies. There is, however, no direct evidence of planets in these systems.

Our understanding of the planetary formation process can easily be invoked to explain these observations. Consider the solar system. Apart from the planets, there are several minor bodies orbiting the Sun on stable orbits that can be explained as remnants of the planetary formation process (Lissauer 1993): the asteroids in the asteroid belt between 2 and 4 AU, that are planetesimals that were inhibited from growth into a planet by gravitational perturbations from Jupiter; the Kuiper belt (see, e.g., Jewitt 1999), which lies beyond the orbit of Neptune (i.e., beyond 30 AU), is a reservoir of icy bodies that were unable to form into planets due to the long accretion timescales there; the short period comets, which have orbits that are more eccentric and inclined than the asteroids, that are probably scattered Kuiper belt objects (Levison & Duncan 1997); and the Oort cloud of comets, which extends out beyond 1000 AU, which are probably scattered planetesimals formed in the Saturn-Neptune region (Hahn & Malhotra 1999). It is also known that in the early solar system there was probably a lot more debris material that has since been either ejected from the system (e.g., into the Oort cloud) or accreted onto the planets, since both lunar and martian cratering records show that the first 800 Myrs of the solar system was an era of heavy bombardment. Collisions between debris material in regions in the Vega-type disks that are analogous to the Kuiper belt in the solar system could provide an ample reservoir of small particles with which to cause an infrared excess.

However, the planetary formation process is not well defined, and just because emission is seen from Kuiper belt regions, one cannot automatically assume that there is a solar-like planetary system interior to that (Kalas 1998) — we could be seeing either failed planetary systems, or systems quite unlike our own. It is evident, therefore, that observations of this class of object can reveal much information about the state of the planetary formation process in these systems. Combined with information about the age of the systems[2], this will help to refine the paradigm of planetary formation. This fact has not gone unnoticed by the astronomical community and there has been a wealth of observations (and consequent modeling) of the stars found by IRAS to have Vega-type excesses. The disk that has attracted the most attention is the β Pictoris disk, because until the 10 μm images of the K2 star SAO 26804 (Skinner et al. 1995), it was the only Vega-excess star with dust confirmed to be confined to a disk geometry. A variety of observational techniques spanning the electromagnetic spectrum have provided a wealth of information about the β Pictoris system (for a recent review, see Artymowicz 1997), but perhaps the most intriguing result is that there is mounting suggestive evidence for planets in the disk. Images of the disk in both optical (Kalas & Jewitt 1995; Schultz & Heap 1998, see Fig. 1.4) and mid-IR (Pantin et al. 1997) wavebands show asymmetries in the outer disk, and a warp in the inner disk, that have been shown by various authors to be possible consequences of planets embedded in the disk (Roques et al. 1994; Lazzaro et al. 1994; Mouillet et al. 1997b). A further indication of planets is the spectroscopic variability of the star (Lagrange et al. 1987) which has been attributed to the conversion of km-sized solid bodies into hot plasma near the star. There is also evidence of photometric variability of β Pictoris that may be due to the passing of a giant planet in front of the stellar image (Lecavelier des Etangs et al. 1995).

One of the fundamental goals of the observing programs has been to obtain resolved images of the material causing the IR excesses observed by IRAS, since these images provide crucial information about the spatial distribution of the emitting material. The reason it took so long for disks other than β Pictoris to be resolved is that the other Vega-excess disks were either too dim or too distant to be resolved with available technology. The technology is now available and this field is going through a very exciting time as disks are being resolved at a steady rate in the near-IR (e.g., Schneider et al. 1999), the mid-IR (e.g., Telesco et al. 2000; Fisher et al. 2000), and the sub-mm (e.g., Holland et al. 1998; Greaves et al. 1998). The potential of these observations to reveal information suggestive of planets in the systems, which was previously shown with the β Pictoris disk, was confirmed with

[2]Note that age estimates for stars that are on the main sequence are notoriously imprecise (Lachaume et al. 1999); e.g., estimates for the age of β Pictoris based on isochrone fitting gave ages from zero age main sequence, 8 Myr, to a more mature 100 Myr (the best current estimate based on a variety of techniques is 20 Myr; Barrado Y Navascués et al. 1999).

Figure 1.5: A picture of the zodiacal light obtained at Mt. Mauna Kea, Hawaii (Ishiguro 1999). The zodiacal light is sunlight scattered by the interplanetary dust cloud (i.e., the zodiacal cloud).

observations of an apparent asymmetry in the disk around the A0V star HR 4796A (Telesco et al. 2000). This asymmetry was shown to be a possible indicator of planets in the system (Wyatt et al. 1999). Another link between these debris disks and planets was made when a disk was observed around 55 Cancri (Trilling & Brown 1998), which is one of the stars with a planetary companion as inferred from radial velocity measurements (see Fig. 1.1).

1.6 The Zodiacal Cloud

At the moment, what is needed is a firm physical model with which to interpret observations of circumstellar debris disks. As with the paradigm for planetary formation process, it is most instructive to start with the system about which we have the most information: the solar system. Not only does the solar system contain debris material, it also contains a tenuous disk of dust, the zodiacal cloud. The zodiacal cloud is visible to the naked eye from suitable viewing locations as the zodiacal light, caused by the scattering of sunlight by the dust particles (see Fig. 1.5). From the shape and color of the zodiacal light, it was inferred that the disk is comprised of 1-1000 μm dust particles extending from a region beyond the asteroid belt into the Sun forming a disk with a flattened lenticular shape (see, e.g., Leinert & Grün 1990). This disk is very tenuous; it has an optical depth of $\sim 10^{-7}$ at 1 AU, and the total mass of the disk is estimated to be $10^{16} - 10^{17}$ kg, equivalent to the mass of one large comet (Leinert & Grün 1990). Further evidence as to the nature of the dust particles in the disk came from stratospheric dust collection experiments, impact craters on the Moon, and deep-sea sediment records. These confirmed the size range of the disk particles and showed some evidence as to their elemental composition and morphology (Leinert & Grün 1990; Gustafson 1994). Meteor observations showed that there is also a population of particles in the disk that are larger than those responsible for the zodiacal light.

Because the zodiacal cloud resides in the solar system, we have a lot of information available as to the possible sources of this dust. The zodiacal cloud is generally accepted to be caused by a combination of the grinding down of the asteroid belt (e.g., Dermott et al. 1984; Durda & Dermott 1997) and the break-up of comets (Sykes et al. 1986; Liou et al. 1995). There is also a small proportion of interstellar grains (Grogan et al. 1996) and there is an as yet undetermined amount of Kuiper belt material (Backman et al. 1995; Liou et al. 1996; Gurnett et al. 1997). However, the exact contribution of each of these sources is still unknown. The theory is that the small particles that are responsible for the zodiacal light are continuously being created from these sources, and evolve into the inner solar system due to radiation drag forces (Burns et al. 1979). This explains why the zodiacal cloud extends all the way in to the Sun, while the orbits of the sources do not, and also accounts for the detailed structure of the cloud (see next paragraph), as well as the size and composition of the constituent particles.

Much of our information about the structure of the zodiacal cloud has come from observations of the disk's thermal emission. The infrared satellites IRAS and COBE mapped the large-scale structure of the zodiacal cloud with unprecedented detail: the observations have an extremely high resolution because of the proximity of the cloud; they also have a high signal-to-noise ratio because the zodiacal cloud is the primary source of infrared flux in most directions except that of the Galactic plane. Such observations are particularly useful for studying the disk's structure, since the observations change throughout the year as the Earth moves through the disk. These observations proved that the structure of the zodiacal cloud, which was initially thought to be smooth, actually contains asymmetries: low level bands of emission were found above the emission of the smooth background cloud both above and below the ecliptic (Low et al. 1984); the center of symmetry of the cloud was shown to be offset from the Sun (Dermott et al. 1999); the cloud was shown to be warped (Dermott et al. 1999); and an asymmetric ring of dust was discovered that co-orbits with the Earth (Dermott et al. 1994; Reach et al. 1995).

To provide a successful interpretation of these observations, techniques were developed that model the structure of the zodiacal cloud based on an understanding of the dynamical evolution of the constituent particles from their source in the asteroids and comets, to their sink at the Sun (Dermott et al. 1992). Such physically-based modeling techniques provided a quantitative method for probing the structure of the zodiacal cloud, and were proven to be extremely successful. These techniques showed that the first asymmetry, the dust bands, are caused by the break-up of individual asteroids (Dermott et al. 1984; Grogan et al. 1997), while the remaining asymmetries are a direct consequence of the secular and resonant gravitational perturbations of the solar planetary system (e.g., Dermott et al. 1994; Dermott et al. 1999); i.e., these last asymmetries are the planets' signatures.

Thus, our understanding of the structure of the zodiacal cloud tells us that if it were seen from afar, asymmetries in its observed structure could be used to infer the existence of planets in the solar system. Actually, even at a distance of 1 pc, the zodiacal cloud would be too dim and its structure too close to the Sun to be detected with current technology (Backman 1998). Observations of debris dust originating in the Kuiper belt, however, would be on a much larger scale, and these too could be used to infer information about the solar planetary system (Liou & Zook 1999). The density of such a population is undetermined as yet and it may also be too dim to detect. Regardless of whether the solar debris disk is detectable, there are debris disks that are dense enough to have been observed, and our understanding of the structure of the zodiacal cloud shows that if there are any planets in these systems then their signatures could be imprinted on the observed disk structures. Furthermore, the zodiacal cloud modeling techniques provide a method for modeling those structures in a quantitative manner.

1.7 Aims and Outline

Just as recent technological accomplishments have unveiled a new era in the study of circumstellar debris disks, so they have for the fields of extrasolar planetary detection and the study of

the protoplanetary disks around young stars. This means that we are amassing an unprecedented amount of information about all stages of a star's evolution, and our concepts of that evolution are continually being challenged, since we want to be able to fit all observational evidence into a coherent picture of stellar evolution that explains both the similarities and the dissimilarities between different systems. The broad theme that this dissertation aims to contribute to is our quest to understand how stars and their environments evolve. More specific questions that the dissertation aims to answer are: What are the signatures of a planetary system in a circumstellar debris disk observation? What can we infer from debris disk observations about the stellar environment? Can we infer the existence of planets in the systems that might otherwise remain undetected?

The observations that are dealt with in this dissertation are images of a disk's thermal emission. The physics behind these observations and the role of modeling in their interpretation is discussed in Chapter 2. Chapter 3 then gives a comprehensive discussion of the physical processes that govern the evolution of a disk's particles and uses this to provide a physical model for the evolution of circumstellar debris disks. This model is equally valid for the physics of the zodiacal cloud as for the physics of most debris disks (within the limitations of the model). Chapter 4 shows quantitatively how the presence of planets in a disk affects its structure, causing the offset, warp and resonant structures observed in the zodiacal cloud. Chapter 5 discusses possible models for the disk particle's optical properties. The theory of Chapters 2 to 5 can be combined to model observed debris disk structure. Such modeling is demonstrated by its application to the observations of one particular disk, the HR 4796 disk. Chapter 6 gives a literature review of previous work on the HR 4796 disk; Chapter 7 describes a model of the disk using these techniques; and Chapter 8 discusses its interpretation. The dissertation is summarized in Chapter 9, where recommendations for future work are also given.

CHAPTER 2
DISSECTION OF A CIRCUMSTELLAR DISK OBSERVATION

The observed brightness of a circumstellar debris disk comes from two sources: starlight that has been absorbed by the disk particles and re-emitted as thermal radiation (primarily at mid-IR, far-IR, and submillimeter wavelengths at $\lambda > 5$ μm), and starlight that has been scattered by the disk particles (primarily at optical and near-IR wavelengths at $\lambda < 2$ μm). This dissertation deals only with a disk's thermal emission.

2.1 Disk Particle Thermal Emission

A particle of diameter D, that is at a distance r from a star, is heated by the stellar radiation to a temperature T that can be calculated from the equilibrium between the energy that the particle absorbs and that which it re-emits as thermal radiation. This temperature depends on the particle's optical properties (Gustafson 1994):

$$T(D,r) = [\langle Q_{abs}\rangle_{T_\star} / \langle Q_{abs}\rangle_{T(D,r)}]^{1/4} * T_{bb}, \tag{2.1}$$

where this equation must be solved iteratively, since the particle's temperature appears on both sides of the equation, $\langle Q_{abs}\rangle_{T_\star}$ and $\langle Q_{abs}\rangle_{T(D,r)}$ are the particle's absorption efficiency averaged over the stellar spectrum (which can be approximated as that of a black body radiating at the star's effective temperature $T_\star$) and the spectrum of a black body radiating at a temperature T, and T_{bb} is the equilibrium temperature of the particle if it were a black body:

$$T_{bb} = 278.3\sqrt{a_\oplus / r} * (4\sigma/A)(L_\star/L_\odot)^{1/4}, \tag{2.2}$$

where T_{bb} is given in K, σ/A is the ratio of the particle's cross-sectional area to its surface area (e.g., spherical particles have $\sigma = \pi D^2/4$ and $A = \pi D^2$, giving $\sigma/A = 1/4$), and $L_\star$ and $L_\odot$ are the luminosities of the star and the Sun.

If this particle is at a distance $R_\oplus$ from the Earth, the contribution of its thermal emission to the flux density at a wavelength, λ, received at the Earth is given by:

$$F_\nu(\lambda, D, r) = Q_{abs}(\lambda, D) B_\nu[\lambda, T(D,r)]\Omega(D), \tag{2.3}$$

where B_ν is the Planck function, and $\Omega = \sigma/R_\oplus^2$ is the solid angle subtended at the Earth by the cross-sectional area of the particle.

2.2 Disk Structure Definition

A circumstellar disk consists of particles with a range of sizes, compositions and morphologies. Throughout this dissertation, however, disk particles are assumed to have the same composition and morphology, and a particle's size is characterized by its diameter, D. Disk particles span a range of sizes from D_{min}, the smallest (probably submicron-sized) particles sustainable for a given disk, up to D_{max}, the largest (probably kilometer-sized) members of the disk that were formed from the protoplanetary disk. The spatial distribution of these particles can be defined by $n(D, r, \theta, \phi)$, where $n(D, r, \theta, \phi)dD$ is the volume density (number per unit volume) of particles in the size range $D \pm dD/2$ at a location in the disk defined by r, the radial distance from the star, θ, the longitude relative to an arbitrary direction, and ϕ, the latitude relative to an arbitrary reference plane. However, since it is a particle's cross-sectional area that is apparent in an observation (eq. [2.3]), a disk's

observable structure is better defined in terms of $\sigma(D,r,\theta,\phi) = n(D,r,\theta,\phi)\sigma$, the cross-sectional area per unit volume per unit diameter.

The definition of a disk's structure can be simplified by assuming the size distribution of its particles to be independent of θ and ϕ:

$$\sigma(D,r,\theta,\phi) = \bar{\sigma}(D,r)\sigma(r,\theta,\phi), \tag{2.4}$$

where $\bar{\sigma}(D,r)dD$ is the proportion of the total cross-sectional area of the disk at r that is in particles in the size range $D \pm dD/2$, and

$$\sigma(r,\theta,\phi) = \int_{D_{min}}^{D_{max}} \sigma(D,r,\theta,\phi)dD \tag{2.5}$$

is the spatial distribution of cross-sectional area of particles of all sizes in the disk.

2.3 Line of Sight Brightness

To determine the observed brightness of a circumstellar disk in, for example, one pixel of an image of the disk, two components of the observation must be defined: the vector, $\mathbf{R}$, which extends from the observer to the disk, and which describes how the line of sight intersects the disk in terms of r, θ, and ϕ; and the solid angle of the observation, Ω_{obs}, where $\Omega_{obs} = d_{pix}^2$ for pixels of width d_{pix} radians.

Consider a volume element along this line of sight that is at a location in the disk defined by r,θ,ϕ, and that has a length $\mathbf{dR}$; the element volume is $dV = \Omega_{obs}R_{\oplus}^2\mathbf{dR}$. The contribution of the thermal emission of the particles in this element to the disk's brightness in the observation is given by:

$$\begin{aligned} dF_\nu(\lambda,r,\theta,\phi)/\Omega_{obs} &= \int_{D_{min}}^{D_{max}} Q_{abs}(\lambda,D)B_\nu[\lambda,T(D,r)]\sigma(D,r,\theta,\phi)dD\mathbf{dR}, & (2.6)\\ &= P(\lambda,r)\sigma(r,\theta,\phi)\mathbf{dR}, & (2.7) \end{aligned}$$

where equation (2.7) uses the simplification for the disk structure given by equation (2.4), and

$$P(\lambda,r) = \int_{D_{min}}^{D_{max}} Q_{abs}(\lambda,D)B_\nu[\lambda,T(D,r)]\bar{\sigma}(D,r)dD. \tag{2.8}$$

Thus, the brightness of this element is not affected by the solid angle of the observation, neither is it affected by the distance of the element from the Earth.

Equation (2.8) can also be written as:

$$P(\lambda,r) = \langle Q_{abs}(\lambda,D)B_\nu[\lambda,T(D,r)]\rangle_{\sigma(D,r)}; \tag{2.9}$$

i.e., $P(\lambda,r)$ is simply $Q_{abs}(\lambda,D)B_\nu[T(D,r),\lambda]$ (which is a combination of the particles' optical properties) averaged over the disk's cross-sectional area distribution, $\sigma(D,r)$. Thus, $P(\lambda,r)$ can also be given by:

$$P(\lambda,r) = Q_{abs}(\lambda,D_{typ})B_\nu[\lambda,T(D_{typ},r)], \tag{2.10}$$

where D_{typ} is the size of disk particle that characterizes (and hence dominates) the disk's emission. This characteristic particle size could be different in different wavebands, as well as at different distances from the star, but always lies in the range $D_{min} < D_{typ} < D_{max}$; its value can be found by considering the relative contribution of particles of different sizes to $P(\lambda,r)$. Unless the optical properties of the particles prevent it, the particles that dominate a disk's mid-IR ($\lambda = 10 - 20$ μm) emission are also those that contribute most to its cross-sectional area, i.e., they are those that dominate the disk's structure, $\sigma(r,\theta,\phi)$ (see, e.g., §7.2).

The total brightness of the disk in this observation is the integral of equation (2.6) over $\mathbf{R}$.

2.4 Observing Procedure: Real Images

It is not in the remit of this dissertation to describe actual observing procedures in detail (for an example of which, see Telesco et al. 2000). This section merely aims to point out that real observations are far more complicated than equation (2.7) might imply. Consider an image of a disk that is made up of many pixels. The disk's brightness along the line of sight, **R**, of each pixel is given by equation (2.7). This describes a "pure" image of the disk emission; i.e., the best image possibly attainable, albeit in unrealistic observing conditions.

Consider this image (which is never actually observed) as it travels from the disk to the detector. First of all, it is joined by the photospheric emission from the point-like star. Before arriving at the Earth, the disk+star emission is subject to extinction by the interstellar medium, and before arriving at the detector, it suffers further extinction in the Earth's atmosphere, as well as in the telescope and detector optics. This extinction image is joined by an emission image, which includes the extra emission along the path from the interstellar medium, the sky, and the telescope and detector optics. The combined extinction+emission image is smoothed by the observational point spread function (PSF), a combination of the seeing conditions and the telescope and instrumental optics, which, in the diffraction-limited case, for an ideal instrument, can be approximated as gaussian smoothing with FWHM $= \lambda/D$, where this D is the diameter of the telescope. The observed image also contains random noise fluctuations from the detector array, and suffers systematic variations from pixel to pixel due to flat field effects (e.g., due to pixel responsivity or dust in the instrument).

Luckily, observing procedures are able to recover a useful image of the disk from the mess described in the last paragraph: a procedure called chopping and nodding removes the sky and telescope emission (although it cannot eliminate the random sky noise); the calibration method of looking at nearby standard stars, the flux densities of which are well-known, removes extinction errors; the image of the star is subtracted by obtaining the PSF from observations of point sources and using knowledge of the stellar flux density (usually extrapolated from visual or near-IR observations assuming the photospheric emission to fall off like a black body); and the flat field is corrected for using observations of blank pieces of sky. There are three potential worries about the image: (1) The image still contains noise. If this noise is above the level of disk emission, the disk emission cannot be unambiguously detected. Noise in an image can be reduced for the purposes of presentation or analysis by further smoothing, although this results in a loss of spatial resolution. (2) The stellar image cannot be completely removed from the image, because neither the PSF nor the stellar flux density are known with infinite precision. If the disk emission lies within the wings of the diffraction image of the star, and it is not bright enough relative to the stellar image, detection of the disk emission might again be ambiguous. (3) Even if the disk is detected, the image obtained has still been convolved with the PSF. This effect can be removed by deconvolution techniques, but these do not provide unique solutions.

2.5 Modeling Disk Images

Thus, a disk observation has four components: the disk's structure, the optical properties of the disk particles, the orientation of the disk to the line of sight, and the observing procedure. The first three combine to produce a "pure" image of the disk emission, which is then modified by the observing procedure. The observing procedure is designed such that its effect on the pure disk image can be modeled (e.g., the PSF is found by taking observations of point-like stars). To model a disk observation, a model of the disk's structure and a model of the optical properties of the particles are needed. These models should accurately reflect the physics of the disk, and will have some free parameters that relate to the physical properties of the disk. These free parameters can be constrained by comparing the real observations with observations of the pure model images at different orientations. Thus the models can be shown either to be contradictory, in which case they need revision, or consistent, in which cases they can be seen as one possible solution, and their free parameters can be interpreted on a physical basis. It is usually the case when studying circumstellar

debris disks that there is too little information to constrain the models with any absolute certainty; i.e., it is easy to find a solution that fits the observation, but harder to find the right one. This is true even to some extent when studying the zodiacal cloud.

Observations of a disk in just one waveband cannot constrain any information about the disk particles' optical properties. Equation (2.7) shows us that the optical properties of the disk particles only show up in the brightness of a disk in a given waveband due to the radial dependence of $P(\lambda, r)$ (which is caused by the radial dependence of the temperature and size distribution). When modeling a disk image in just one waveband, this radial dependence must be fixed if the model for the disk's structure is to be constrained. The optical properties of a disk's particles can be constrained using observations in different wavebands. Ideally this is done using disk images in different wavebands, but it is sometimes done using the disk's SED, with little or no information about the spatial distribution of disk material. The focus of this dissertation is on the interpretation of images of disk structure. The next two chapters are devoted to the development and discussion of a model for debris disk structure, and a model for the disk particle optical properties is discussed in Chapter 5.

CHAPTER 3
THE STRUCTURE OF A DYNAMIC DEBRIS DISK

This chapter outlines the theoretical framework upon which later discussion of circumstellar disk structure (such as how planetary perturbations affect this structure) is based. A disk is a dynamic entity, the constituent particles of which are undergoing constant dynamical and physical evolution. §§3.1 - 3.3 give an extensive discussion of the physical processes acting on disk particles. §3.4 then summarizes our understanding of the dynamic disk by showing how disk particles can be categorized according to the dominant physical processes affecting their evolution. §3.5 expands on this theme to give a tentative paradigm for debris disk evolution.

If we are to make generalizations about the physical processes relevant to debris disk evolution, then the zodiacal cloud is the best example of a debris disk on which to base this understanding, since its properties have been determined with a certain degree of confidence. This confidence stems from the wealth of observational, theoretical, and physical evidence describing its present state, its evolutionary history, and the physical environment of the system it is in. The physical processes that are described in this section are those thought to have dominated the evolution of the zodiacal cloud, supposedly since the Sun reached the main sequence (e.g., Leinert & Grün 1990; Gustafson 1994). These processes should serve as an adequate basis for an understanding of the evolution of debris disks around other main sequence stars that may be at different evolutionary stages.

There is, however, one obvious distinction between the zodiacal cloud and exosolar dust disks. The emission observed from the zodiacal cloud is dominated by that from dust in the inner solar system (within 5 AU of the Sun), which has its origins in the asteroid belt (Dermott et al. 1984; Grogan et al. 1997) and the short period comets (Sykes et al. 1986). In contrast, the emission observed from exosolar dust disks is dominated by that originating from dust in regions analogous to the Kuiper belt in the solar system, i.e., > 30 AU from the star (e.g., Backman & Paresce 1993). Relatively little is known about the Kuiper belt, but, like the inner solar system, it appears to be populated with many asteroid- or comet-like objects that are probably the remnants of the solar system's planetary formation phase (e.g., Jewitt 1999). Also, it is debatable, how far back in time a zodiacal cloud-like model is applicable, since the evolution of very young disks could be dominated by quite different physical processes such as gas drag, self-gravitational perturbations, coagulation, or effects induced by planetary radial migration. Such a model should be valid back to the end of the planetary formation process at $\sim 10^7$ years.

3.1 Gravity

The dominant force acting on all but the smallest disk particles is the gravitational attraction of the star:

$$F_{grav} = GM_{\star}m/r^2, \tag{3.1}$$

where G is the gravitational constant, $M_{\star}$ is the mass of the star, m is the mass of the particle, and r is the distance of the particle from the star. All material is assumed to orbit the star on Keplerian (elliptical) orbits, with other forces acting as perturbations to these orbits. The orbit of a particle is defined by the following orbital elements: the semimajor axis, a, and eccentricity, e, that define the radial extent and shape of the orbit; the inclination, I, and longitude of ascending node, Ω, that define the plane of the orbit (relative to an arbitrary reference plane); and the longitude of pericenter, $\tilde{\omega}$, that defines the orientation of the orbit within the orbital plane (relative to an

arbitrary reference direction). The orbital period of the particle is given by:

$$t_{per} = \sqrt{(a/a_\oplus)^3 (M_\odot/M_\star)}, \tag{3.2}$$

where t_{per} is given in years, $a_\oplus = 1$ AU is the semimajor axis of the Earth's orbit, and $M_\odot$ is the mass of the Sun. At any instant, the location of the particle in its orbit is defined by the true anomaly, f, where $f = 0°$ and $180°$ at the pericenter and apocenter, respectively, and its distance from the star, r, and its velocity, v, are defined by:

$$r = a(1-e^2)/(1+e\cos f), \tag{3.3}$$

$$v = \sqrt{GM_\star(2/r - 1/a)}. \tag{3.4}$$

Since at any given time a particle could be at any point along its orbit, its contribution to the distribution of material in a disk can be described by the elliptical ring that contains the mass of the particle spread out along its orbit, the line density of which varies inversely with the particle's velocity (eq. [3.4]). Each disk particle has an orbit defined by a different set of orbital elements, with a contribution to the spatial distribution of material in the disk that can be described by a corresponding elliptical ring. Thus, a disk's structure can be defined by the distribution of orbital elements of its constituent particles, $n(D, a, e, I, \Omega, \tilde{\omega})$, where $n(D, a, e, I, \Omega, \tilde{\omega}) dD da de dI d\Omega d\tilde{\omega}$ is the number of disk particles with sizes in the range $D \pm dD/2$, and orbital elements in the range $a \pm da/2, e \pm de/2, I \pm dI/2$, $\Omega \pm d\Omega/2, \tilde{\omega} \pm d\tilde{\omega}/2$. A disk's orbital element distribution can be quantified in terms of the evolutionary history of the system and the physical processes acting on the disk's particles. Using techniques such as those described in §7.1.2, the resulting structure can then be compared with the disk's observable structure, $\sigma(D, r, \theta, \phi)$, to link a disk observation with the physics of the particles in that disk. It is often convenient to discuss the dependence of the orbital element distribution on the different parameters separately; e.g., the distribution of semimajor axes, $n(a)$, is defined such that $n(a)da$ is the total number of particles with orbital semimajor axes in the range $a \pm da/2$.

3.2 Collisions

3.2.1 Collisional Cascade

A typical disk particle is created by the break-up of a larger parent body, either as the result of a collision with another body, or simply by its disintegration. This parent body could have been created by the break-up of an even larger body, and the particle itself will most likely end up as a parent body for particles smaller than itself. This collisional cascade spans the complete size range of disk material, excluding the planets[1], and the particles that share a common ancestor are said to constitute a "family" of particles.

The size distribution that results from this collisional cascade can be found from theoretical arguments (Dohnanyi 1969):

$$n(D) \propto D^{2-3q}, \tag{3.5}$$

where $q = 11/6$. This distribution is expected to hold for disk particles that are large enough not to be affected by radiation forces (§3.3). A disk with this distribution has its mass, $m(D) = n(D)m$, concentrated in its largest particles, while its cross-sectional area, $\sigma(D) = n(D)\sigma$, is concentrated in its smallest particles. Collisions in such a disk are mostly non-catastrophic (see eqs. [3.7]-[3.11]), and a particle in this disk is most likely to be broken up by a particle that has just enough mass (and hence energy) to do so. This in turn means that collisional fragments have velocities, and hence orbital elements, that are almost identical to those of the original particle; i.e., in the absence of other forces, all members of the same family have identical orbits. Due to the interaction of the

[1] The planets are the result of runaway accretion (Lissauer 1993) and are far larger than the bodies impacting them. This means that all collisions that they suffer result in accretion of the impacting body onto the planet. Collisions between planets, however, can be destructive, and this may explain the origin of the Moon (see, e.g., Cameron 1997).

competing physical processes, the size distribution of disk particles that are affected by radiation forces is only really understood qualitatively (§§3.3 and 3.4.2). Their distribution is particularly important, since, in general, a disk's cross-sectional area (and hence its observable structure) is concentrated in these smaller particles.

3.2.2 Collisional Lifetime

The importance of collisions in determining a particle's evolution depends on its collisional lifetime. Consider a collision between two disk particles, the larger of which is denoted by the subscript 1, and the smaller by the subscript 2. For this collision to be catastrophic, that is, for it to result in the break-up of the larger particle, the impact energy of the collision must be large enough both to overcome the tensile strength of the larger particle, and to impart enough energy to the collisional fragments to overcome its gravitational binding energy. In the asteroid belt this limit means that a collision is only catastrophic if $m_2/m_1 \geq 10^{-4}$ (Dohnanyi 1969). Since the impact energy of a collision is $\propto m_2 v_{rel}^2$, assuming that exosolar disk particles have similar tensile strengths to the solar system's asteroids, this limit can be scaled to exosolar disks by the square of the ratio of the mean relative velocity of collisions in the asteroid belt (at ~ 3 AU), $v_{rel} \approx 5$ km/s (Vedder 1998), to that of collisions in the exosolar disk. The mean relative velocity of collisions in exosolar disks can be described by:

$$v_{rel}(r) = f(e, I) v(r), \tag{3.6}$$

where $f(e, I)$ is some function of the disk particles' eccentricities and inclinations, and $v(r) = 30\sqrt{(M_\star/M_\odot)(a_\oplus/r)}$ km/s is the average velocity of particles at r (eq. [3.4] with a replaced by r). Thus, assuming $f(e, I) \approx 0.3$ as for collisions in the asteroid belt, an exosolar disk particle of diameter $D \propto m^{1/3}$, would only suffer a catastrophic collision if the other particle in the collision had a diameter $\geq D_{cc}(D)$, where

$$D_{cc}(D) = 0.03[(M_\odot/M_\star)(r/a_\oplus)]^{1/3} D. \tag{3.7}$$

The collisional lifetime, i.e., the mean time between catastrophic collisions, of a particle of diameter D, at a location in a disk denoted by r, θ, and ϕ, is the inverse of its catastrophic collision rate (Kessler 1981):

$$t_{coll}(D, r, \theta, \phi) = [R_{coll}(D, r, \theta, \phi)]^{-1}, \tag{3.8}$$

where

$$R_{coll}(D, r, \theta, \phi) = \sigma_{cc}(D, r, \theta, \phi) v_{rel}(r), \tag{3.9}$$

$\sigma_{cc}(D, r, \theta, \phi)$ is the catastrophic collision cross-section seen by the particle, and $v_{rel}(r)$ is the mean encounter velocity of disk particles at r (eq. [3.6]). Using the definition of a disk's structure given by equation (2.4), this catastrophic collision cross-section is:

$$\sigma_{cc}(D, r, \theta, \phi) = f_{cc}(D, r) \sigma(r, \theta, \phi), \tag{3.10}$$

where

$$f_{cc}(D, r) = \int_{D_{cc}(D)}^{D_{max}} (1 + D/D')^2 \bar{\sigma}(D', r) dD', \tag{3.11}$$

and $D_{cc}(D)$ is the smallest particle with which a catastrophic collision could occur (eq. [3.7]).

However, unless $t_{coll} \ll t_{per}$, the particle's orbit takes it through a range of θ and ϕ before a collision occurs (there is also a variation of r along the particle's orbit due to the eccentricity of its orbit). Thus, it is more appropriate to calculate the particle's collisional lifetime using the mean catastrophic collision rate of the particles in the size range $D \pm dD/2$ that are in the spherical shell of

radius, r, and width dr. Consider an element of this shell that has a volume, $dV = r^2 dr d\theta \cos\phi d\phi$. The number of particles in the diameter range $D \pm dD/2$ in this element is given by $n(D, r, \theta, \phi) dD dV$, and each of these particles has a catastrophic collision rate given by equation (3.9). Integrating over the whole shell gives:

$$t_{coll}(D, r) = \frac{\int_{-I_{max}}^{+I_{max}} \int_0^{2\pi} \sigma(r, \theta, \phi) d\theta \cos\phi d\phi}{\int_{-I_{max}}^{+I_{max}} \int_0^{2\pi} [\sigma(r, \theta, \phi)]^2 d\theta \cos\phi d\phi * f_{cc}(D, r) v_{rel}(r)}, \tag{3.12}$$

where I_{max} is the maximum inclination of the disk particles' orbits to the reference plane.

Equation (3.12) can be simplified by considering a cylindrical shell, defined by r, θ, and z, rather than a spherical one. An element of the cylindrical shell has a volume $dV = r dr d\theta dz$, and the corresponding collisional lifetime of a particle in the shell is given by equation (3.12), but with ϕ, $\cos\phi d\phi$ and $\pm I_{max}$, replaced by z, dz, and $\pm h$, where $h = r \sin I_{max}$. Here we introduce the parameter τ_{eff}, the disk's face-on effective optical depth:

$$\tau_{eff}(r) = \int_{-h}^{+h} \sigma(r, \theta, z) dz, \tag{3.13}$$

where the dependence on θ has been dropped since orbits sample the full range of θ. This is not a true optical depth, since that would include a consideration of the particles' extinction coefficients ($Q_{ext} = Q_{abs} + Q_{sca}$); rather, it is the disk's face-on surface density of cross-sectional area, which is equal to its true optical depth if its particles had $Q_{ext} = 1$. Assuming that $\sigma(r, \theta, z)$ is independent of z, so that $\int_{-h}^{+h} [\sigma(r, \theta, z)]^2 dz = 0.5 \tau_{eff}(r)^2 / h$, and that the encounter speed is determined by the vertical motion of particles in the disk, so that $f(e, I) \approx \sin I_{max}$, equation (3.12) can be simplified to:

$$t_{coll}(D, r) = \frac{t_{per}(r)}{\pi f_{cc}(D, r) \tau_{eff}(r)}, \tag{3.14}$$

where $t_{per}(r)$ is the average orbital period of particles at r (eq. [3.2] with a replaced by r).

A disk's effective optical depth, τ_{eff}, can be estimated observationally from equation (2.6):

$$\tau_{eff}(r) \approx (F_\nu(\lambda, r)/\Omega_{obs})/P(\lambda, r), \tag{3.15}$$

where F_ν/Ω_{obs} is the disk's face-on unsmoothed brightness. The disk's face-on unsmoothed brightness can be calculated either from the observed brightness, making corrections to account for both the disk's orientation, as well as for the PSF smoothing, or from the disk's total flux density, $F_\nu(\lambda)$, and assuming the disk material to be evenly distributed between $r \pm dr/2$:

$$F_\nu(\lambda, r)/\Omega_{obs} = F_\nu(\lambda) C_f R_\star^2 / r dr, \tag{3.16}$$

where $C_f = 6.8 \times 10^9$ AU^2/pc^2/sr, and $R_\star$ is the distance of the star from the observer.

3.2.2.1 Collisional Lifetime of Particles with the Most Cross-sectional Area

Consider the particles in a disk that make up most of the disk's cross-sectional area, i.e., those that have diameters close to D_{typ} and that are expected to characterize the disk's mid-IR emission (§2.3). By definition, these particles are most likely to collide with each other (a collision that would definitely be catastrophic), and so their collisional lifetime can be found from equation (3.12) using the approximation:

$$f_{cc}(D_{typ}, r) \approx 4. \tag{3.17}$$

Applying this approximation to equation (3.14) gives:

$$t_{coll}(D_{typ}, r) = t_{per}(r)/4\pi\tau_{eff}(r). \tag{3.18}$$

This is also the collisional lifetime derived by Artymowicz (1997) for particles in β Pictoris.

3.2.2.2 Collisional Lifetime of a Disk's Large Particles

The collisional lifetime of particles of different sizes in a disk differ only by the factor $f_{cc}(D,r)$. This factor can be ascertained by making assumptions about the disk particles' size distribution. Assuming that the size distribution of equation (3.5) holds for disk particles between D_{min} and D_{max}, the normalized cross-sectional area distribution is given by:

$$\bar{\sigma}(D) = (3q-5)D^{4-3q}/D_{min}^{5-3q}. \tag{3.19}$$

Substituting into equation (3.11) gives:

$$f_{cc}(D) = \left(\frac{XD}{D_{min}}\right)^{5-3q}\left[1+\frac{6q-10}{(3q-4)X}+\frac{3q-5}{(3q-3)X^2}\right], \tag{3.20}$$

where $X = D_{cc}(D)/D$ for $D_{cc}(D) > D_{min}$, and $X = D_{min}/D$ for $D_{cc}(D) \leq D_{min}$; the collisional lifetime of particles in a disk with this distribution is a minimum for particles for which $D_{cc}(D) = D_{min}$. The size distribution of particles in a real disk is more complicated than equation (3.19), however, equation (3.20) can be used to give a crude approximation for the collisional lifetime of a disk's large particles:

$$t_{coll}(D,r) \approx t_{coll}(D_{typ},r) * (D_{cc}(D)/D_{typ})^{3q-5}. \tag{3.21}$$

Thus, the collisional lifetime of particles with $D > D_{typ}$ can be considerably longer than that of equation (3.18), and a disk's largest particles, those for which $t_{coll}(D,r) > t_{sys}$, may not have suffered any catastrophic collisions since they were first created; such particles are primordial particles. The cascades of very young disks may still contain a significant proportion of primordial particles; i.e., their cascades may not be fully evolved.

3.2.2.3 Other Considerations for a Particle's Collisional Lifetime

If there is a significant change in r along a particle's orbit due to the eccentricity of its orbit, this can be taken into account when calculating its collisional lifetime. By considering the washer-like disk of particles on orbits with a, e, and random $\tilde{\omega}$ (Sykes 1990): $t_{coll}(a,e) = \pi[\int_q^{q'}(r/a)/[t_{coll}(r)\sqrt{(r-q)(q'-r)}]dr]^{-1}$, where $q = a(1-e)$ is this disk's inner edge, and $q' = a(1+e)$ is its outer edge.

3.2.3 Evidence from the Zodiacal Cloud

The collisional cascade theory is well-supported by evidence from the zodiacal cloud. The size distribution of the largest ($D > 3$ km) members of the zodiacal cloud's collisional cascade, the observable asteroids, is well-approximated by equation (3.5) (Durda & Dermott 1997; Durda et al. 1998; see Fig. 3.1). The distribution of the very largest ($D > 30$ km) asteroids deviates from this distribution, however, because of the transition from strength-scaling to gravity-scaling for asteroids larger than ~ 150 m (Durda et al. 1998). The size distribution of the zodiacal cloud's medium-sized (1 mm $< D <$ 3 km) members is also expected to follow equation (3.5) (Durda & Dermott 1997), but there is no observational proof of this, since these members are too faint to be seen individually, and too few to be studied collectively (Leinert & Grün 1990). There is, however, proof that the zodiacal cloud's collisional cascade extends from its largest members down to its smallest dust particles: the dust band thermal emission features (Low et al. 1984) correspond to those expected from the small ($1-1000$ μm) particles resulting from the break-up, some time ago, of a few very large asteroids, the largest fragments of which are still observable as the asteroids in the Themis, Koronis, and, possibly, Eos families (Dermott et al. 1984; Grogan et al. 1997; Grogan et al. 2000; see Fig. 3.2). The size distribution of the zodiacal cloud's smallest ($D < 1$ mm) dust particles (e.g., Leinert & Grün 1990; Love & Brownlee 1993) can be explained qualitatively (e.g., Grün et al. 1985; see also §3.3).

Analysis of the collision rates of objects in the Kuiper belt (Stern 1995) shows that a collisional cascade should exist here too. There is also evidence to suggest that the Kuiper belt was

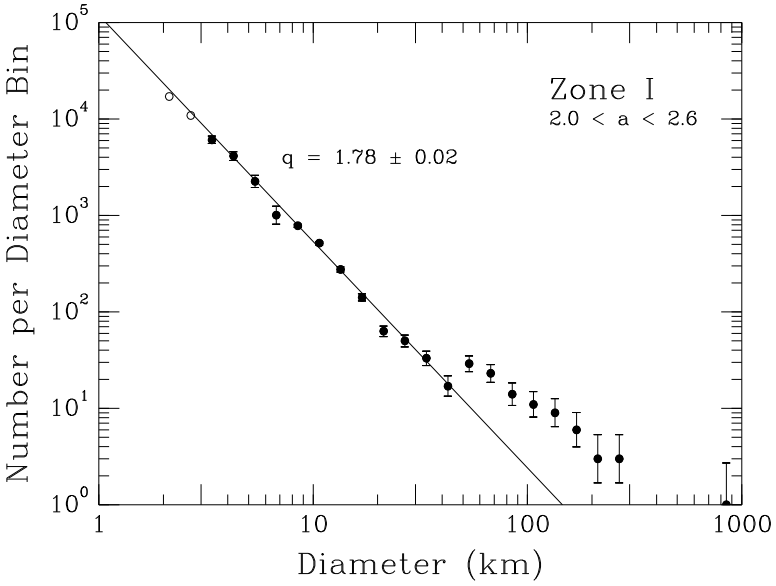

Figure 3.1: Magnitude-frequency diagram of mainbelt asteroids with semimajor axes between 2.0 AU and 2.6 AU (Durda & Dermott 1997).

once more massive than it is today (Jewitt 1999), meaning that in the past collisions would have played a much larger role in determining its structure than they do today, maybe even causing the supposed mass loss (Stern & Colwell 1997). The size distribution of the observed Kuiper belt objects appears to be slightly steeper than that in the inner solar system ($q > 11/6$, Jewitt 1999), while observations have been unable, as yet, to determine its dust distribution (Backman et al. 1995; Gurnett et al. 1997),

3.3 Radiation Forces, β

For most of the collisional cascade, gravity can be considered to be the only significant force acting on disk particles. The smallest particles, however, are significantly affected by their interaction with the photons from the star.

3.3.1 Radiation Pressure

Radiation pressure is the component of the radiation force that points radially away from the star. It is inversely proportional to the square of a particle's distance from the star, and is defined for different particles by its ratio to the gravitational force of equation (3.1) (Gustafson 1994):

$$\beta(D) = F_{rad}/F_{grav} = C_r(\sigma/m)\langle Q_{pr}\rangle_{T_\star}(L_\star/L_\odot)(M_\odot/M_\star), \tag{3.22}$$

where $C_r = 7.65 \times 10^{-4}$ kg/m^2, σ/m is the ratio of the particle's cross-sectional area to its mass (e.g., $\sigma/m = 1.5/\rho D$ for spherical particles of density ρ), and $\langle Q_{pr}\rangle_{T_\star} = \int Q_{pr}(D,\lambda)F_\lambda d\lambda / \int F_\lambda d\lambda$ is the particle's radiation pressure efficiency[2] averaged over the stellar spectrum, F_λ.

An approximation for large particles is that $\langle Q_{pr}\rangle_{T_\star} \approx 1$. Thus, large spherical particles have:

$$\beta(D) \approx (1150/\rho D)(L_\star/L_\odot)(M_\odot/M_\star), \tag{3.23}$$

[2] A particle's radiation pressure efficiency is related to its absorption and scattering efficiencies by $Q_{pr} = Q_{abs} + Q_{sca}(1 - \langle\cos\theta\rangle)$, where $\langle\cos\theta\rangle$ accounts for the asymmetry of the scattered radiation.

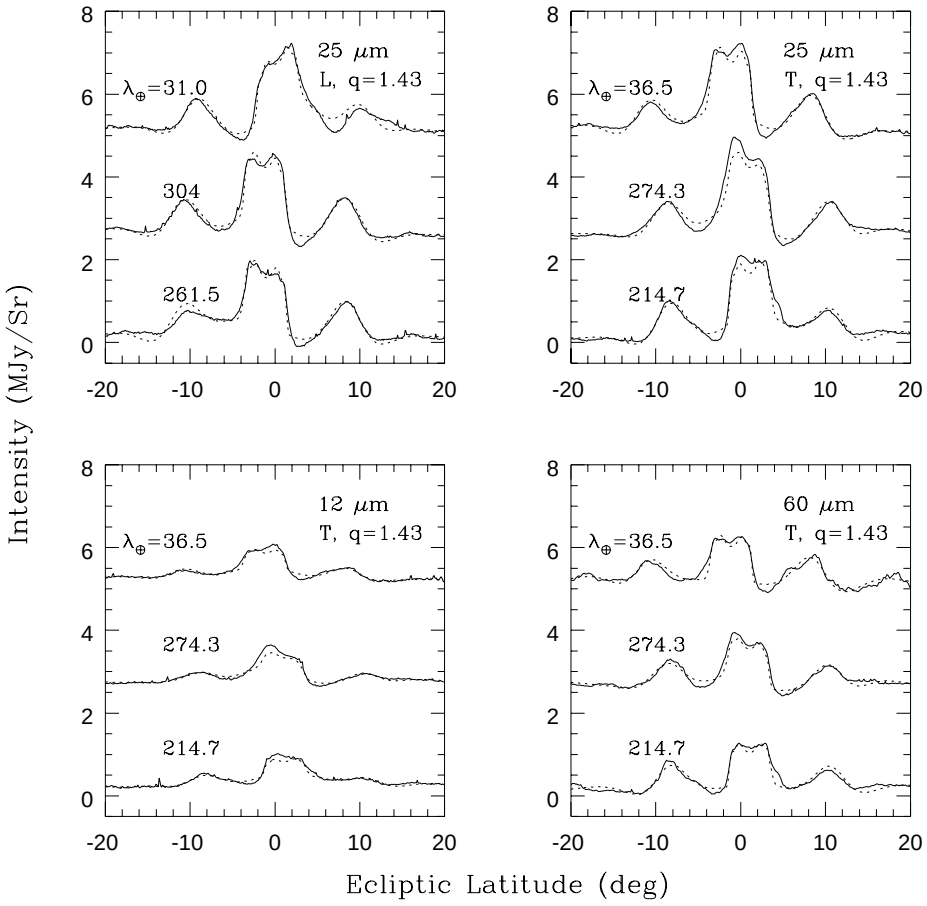

Figure 3.2: Figure showing the fit between IRAS observations of the dust band residuals and a model of this observation (Grogan et al. 2000). The observations are scans at a constant elongation angle in directions both leading (L) and trailing (T) the direction of the Earth's motion at three times throughout the year in the 12, 25, and 60 μm wavebands. The smooth background emission has been subtracted by a Fourier filtering process. The model includes contributions from particles in the size range $1 - 100$ μm from the Eos, Themis, and Koronis asteroid families that have evolved into the inner system by P-R drag, and that have a size distribution that is described by $q = 1.43$.

where ρ is measured in kg/m^3, and D in μm. This approximation is valid for particles in the solar system with $D > 20$ μm (Gustafson 1994). For particles in exosolar systems, this limit scales with the wavelength at which the star emits most of its energy, $\lambda_\star \propto 1/T_\star$; i.e., equation (3.23) is valid for spherical particles with $D > 20(T_\odot/T_\star)$ μm, where $T_\odot = 5785$ K is the effective temperature of the Sun. Since $\beta \propto 1/D$, this means that the smaller a particle, the larger its β. This holds down to micron-sized particles, smaller than which β decreases to a level that is independent of the particle's size (Gustafson 1994).

The effect of radiation pressure is equivalent to reducing the mass of the star by a factor $1-\beta$. This means that a particle for which $\beta \neq 0$ moves slower around the same orbit by a factor of $\sqrt{1-\beta}$ than one for which $\beta = 0$ (eq. [3.4]). It also means that daughter fragments created by the break-up of a parent body move on orbits that can differ substantially from that of the parent. The reason for this, is that while the positions and velocities of a parent and its daughter fragments are the same at the moment of break-up (apart from a small velocity dispersion), their β are different, and so the daughter fragments move in effective potentials that are different from that the parent moved in. Daughter fragments created in the break-up of a parent particle that had $\beta = 0$, and for which orbital elements at the time of the collision were $a, e, I, \Omega, \tilde{\omega}$, and f, move in the same orbital plane as the parent, $I^{'} = I$ and $\Omega^{'} = \Omega$, but on orbits with semimajor axes, $a^{'}$, eccentricities, $e^{'}$, and pericenter orientations, $\tilde{\omega}^{'}$, that are given by (Burns et al. 1979):

$$a^{'} = a(1-\beta)/\left[1 - 2\beta(1 + e\cos f)/(1-e^2)\right], \tag{3.24}$$

$$e^{'} = (1-\beta)^{-1}\sqrt{e^2 + 2\beta e\cos f + \beta^2}, \tag{3.25}$$

$$\tilde{\omega}^{'} - \tilde{\omega} = f - f^{'} = \arctan\left[\beta\sin f/(\beta\cos f + e)\right]. \tag{3.26}$$

Analysis of equations (3.24)-(3.26) shows that the orbits of the largest fragments, those for which $\beta < 0.1$, are similar to that of the parent. On the other hand, the smallest fragments, those for which $\beta > 0.5(1-e^2)/(1+e\cos f)$, have hyperbolic orbits ($e^{'} > 1$). These particles are known as "β meteoroids"[3]. Since β meteoroids are lost from the system on the timescale of the orbital period of the parent (eq. [3.2]), the diameter of particle for which $\beta > 0.5$ essentially defines the lower end of the collisional cascade. However, there may also be a population of submicron particles that have $\beta < 0.5$ (Gustafson 1994). The intermediate-sized fragments, those for which $0.1 < \beta < 0.5$, that we call "β critical" particles, have orbits that differ substantially from that of the parent. However, the point of closest approach to the star of the orbits of all daughter fragments, irrespective of their size, is the same as that of the parent: combining equations (3.24) and (3.25) gives the pericenter distance of daughter fragments, $r_p^{'} = a^{'}(1-e^{'})$, as

$$r_p^{'}/r_p = 1 + e(1-\cos f) + O(e^2). \tag{3.27}$$

The orbits of collisional fragments with different β from a parent particle that was on a circular orbit are shown in Fig. 3.3.

3.3.2 Poynting-Robertson (P-R) Light Drag

The component of the radiation force tangential to a particle's orbit is called the P-R drag force.

3.3.2.1 Basic Equations

Like the radiation pressure force, the P-R drag force is proportional to β. It results in an evolutionary decrease in both the semimajor axis and eccentricity of the particle's orbit (Burns et al. 1979):

$$\dot{a}_{pr} = -(\alpha/a)(2 + 3e^2)/(1-e^2)^{3/2} = -2\alpha/a + O(e^2) \tag{3.28}$$

$$\dot{e}_{pr} = -(\alpha/a^2)2.5e/(1-e^2)^{1/2} = -2.5\alpha e/a^2 + O(e^2), \tag{3.29}$$

[3]Note that particles with $\beta > 1$ are β meteoroids even if they were not created collisionally, since they "see" a negative mass star.

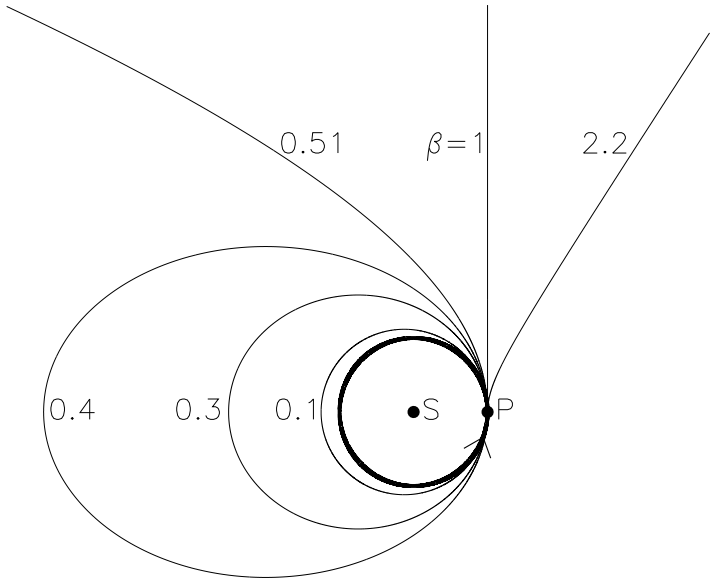

Figure 3.3: Figure showing the new orbits of the fragments of a collision in which a large parent particle P, that was on a circular orbit around a star S, was broken up. Fragments of different sizes have different radiation pressure forces, characterized by a particle's β, acting on them, and so have different orbits: those with $\beta < 0.1$, the "large" particles, have orbits that are close to that of the parent; those with $0.1 < \beta < 0.5$, the "β critical" particles, have orbits that have the same pericenter distance as the parent, but larger apocenter distances; and those with $\beta > 0.5$, the "β meteoroids", have hyperbolic orbits. Since when they are created, the velocity vector of all fragments is perpendicular to the stellar direction, this is the point of their orbit's closest approach to the star. The orbits of fragments with $\beta = 0$, 0.1, 0.3, 0.4, 0.51, 1.0, and 2.2 are shown here. The thick circular line denotes both the orbit of the parent particle and that of collisional fragments with $\beta = 0$. All particles are orbiting the star counterclockwise.

where $\alpha = 6.24 \times 10^{-4}(M_\star/M_\odot)\beta$ AU^2/year. P-R drag does not change the plane of the particle's orbit, $\dot{I}_{pr} = \dot{\Omega}_{pr} = 0$; neither does it affect the orientation of the particle's pericenter, $\dot{\tilde{\omega}}_{pr} = 0$. For a particle with zero eccentricity, equation (3.28) can be solved to find the time it takes for the particle to spiral in from a radial distance of r_1 to r_2:

$$t_{pr} = 400(M_\odot/M_\star)[(r_1/a_\oplus)^2 - (r_2/a_\oplus)^2]/\beta, \tag{3.30}$$

where t_{pr} is given in years.

3.3.2.2 P-R Drag without Collisions

Consider the daughter fragments created in the break-up of a parent body that was on an orbit at a distance r from the star. The largest fragments are broken up by collisions before their orbits have suffered any significant P-R drag evolution, while the smaller fragments, for which the P-R drag evolution is faster, can reach the star (at which point they evaporate) without having encountered another particle. Particles for which P-R drag significantly affects their orbits in their lifetime can be estimated as those for which their collisional lifetime (eq. [3.18]; the use of this equation is justified in the next paragraph) is longer than their P-R drag lifetime (eq. [3.30] with $r_2 = 0$), i.e., those for which $\beta > \beta_{pr}$, where

$$\beta_{pr} = 5000\tau_{eff}(r)\sqrt{(r/a_\oplus)(M_\odot/M_\star)}. \tag{3.31}$$

For large spherical particles, this is also those for which $D < D_{pr}$, where

$$D_{pr} = [0.23/\rho\tau_{eff}(r)]\sqrt{(a_\oplus/r)(M_\odot/M_\star)}(L_\star/L_\odot), \tag{3.32}$$

ρ is measured in kg/m^3, and D_{pr} in μm.

Consider the daughter fragments created in the break-up of an endless supply of parent bodies that are on orbits with the same semimajor axis, a_s. Ignoring collisional processes, the fragments with orbits that are affected by P-R drag, those with $\beta > \beta_{pr}$, have their semimajor axes distributed from $a = a_s$ to $a = 0$ according to (eq. [3.28]):

$$n(a) \propto 1/\dot{a}_{pr} \propto a. \tag{3.33}$$

This corresponds to a volume density distribution that is roughly inversely proportional to distance from the star[4]. If the collisional processes leading to the size distribution of the parent bodies, $n_s(D)$, still holds for the production of the P-R drag affected particles, then their size distribution is given by:

$$n(D) \propto n_s(D)/\dot{a}_{pr} \propto n_s(D)D. \tag{3.34}$$

If $n_s(D)$ can be given by equation (3.5) with $q = 11/6$, the cross-sectional area of a disk's P-R drag affected particles is concentrated in the largest of these particles, while that of its unaffected particles is concentrated in the smallest of these particles; i.e., most of a disk's cross-sectional area is expected to be concentrated in particles with $D_{typ} \approx D_{pr}$, justifying the use of equation (3.18) for the collisional lifetime of these particles.

3.3.2.3 P-R Drag with Collisions

If the P-R drag lifetime, t_{pr} (eq. [3.30]), is comparable to, or shorter than t_{coll}, then the effect of P-R drag on a particle's collisional lifetime must be accounted for; e.g., a particle may evolve quickly out of a dense region where it has a short collisional lifetime, into a less dense one where it can continue its evolution without encountering other particles. On average, particles from a parent at r_{parent}, survive until they reach r_{coll} where $\int_{r_{parent}}^{r_{coll}} \frac{800(M_\odot/M_\star)r}{t_{coll}(r)\beta}dr = 1$.

[4]If the particles had circular orbits, equation (3.33) means a spherical shell of width dr, the volume of which is $\propto r^2 dr$, would contain a number of particles that is $\propto rdr$ (see, e.g., Gorkavyi et al. 1997).

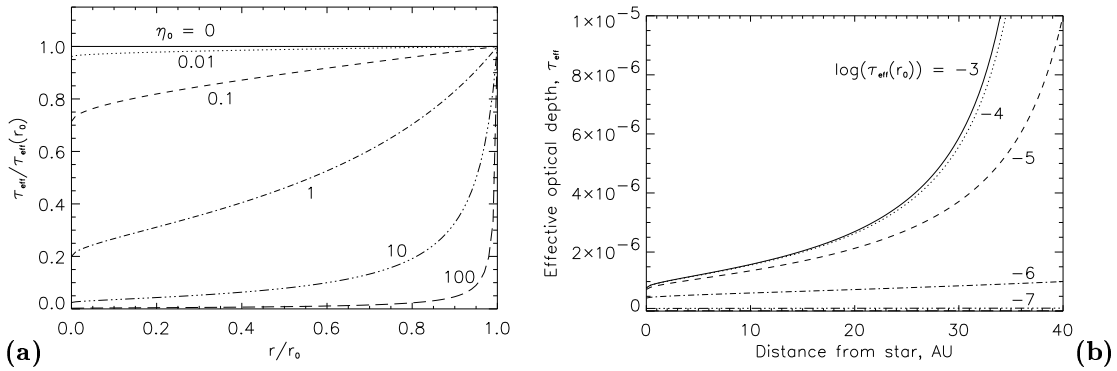

Figure 3.4: The distribution of effective optical depth in a disk resulting from a source of same-sized particles located at r_0. The particles evolve into the inner disk due to P-R drag and mutual collisions (which are assumed to be destructive). The steady state solution depends on the parameter η_0 which is defined by the source parameters. A value of $\eta_0 = 1$ corresponds to the situation when the collisional lifetime of the source particles (if they suffered no P-R drag evolution) is equal to their P-R drag lifetime. **(a)** shows the functional dependence of the distribution on η_0. **(b)** shows the distribution resulting from a source of particles with $\beta = 0.1$ located at 40 AU from a solar mass star, but with different dust production rates that result in different effective optical depths at the source.

The following paragraphs give a heuristic understanding of the structure of a disk of particles that are evolving due to both P-R drag and collisions. Consider a source of particles at r_0, where all of the particles produced are of the same size, D, and consequently have the same P-R drag force, β, affecting them, and all of which have circular orbits. If these particles evolve into the inner disk due to P-R drag and mutual collisions (which are assumed to destroy both particles involved in the collision), then the distribution resulting from this evolution can be found by considering the amount of material entering and leaving an annulus at r of width dr. The steady state solution is that the amount entering the annulus due to P-R drag is equal to that leaving due to P-R drag and that which is lost by collisions (i.e., the continuity equation):

$$d[n(r)\dot{r}_{pr}(r)]/dr = -N^{-}(r), \tag{3.35}$$

where $n(r)$ is the one dimensional number density (number of particles per unit radius), $\dot{r}_{pr}(r) = -2\alpha/r$ is their P-R drag evolution rate (from eq. [3.28]), and $N^{-}(r) = n(r)/t_{coll}(D,r)$ is the rate of collisional loss of $n(r)$.

Taking the collisional lifetime of the particles from equation (3.18) and using the thin disk approximation that $\tau_{eff}(r) = \sigma n(r)/2\pi r$, we find that $N^{-}(r) = 2[n(r)]^2\sigma/rt_{per}(r)$. Substituting into equation (3.35), and solving for the variation of effective optical depth with distance from the star, we find that

$$\tau_{eff}(r)/\tau_{eff}(r_0) = \frac{1}{1 + 4\eta_0(1 - \sqrt{r/r_0})}, \tag{3.36}$$

where $\eta_0 = 5000\tau_{eff}(r_0)\sqrt{(r_0/a_\oplus)(M_\odot/M_\star)}/\beta = \beta_{pr}/\beta$, and $\tau_{eff}(r_0)$ can be calculated from the production rate of these particles. Note that $\eta_0 = 1$ corresponds to the situation when the collisional lifetime of the particles (if they suffered no P-R drag evolution) is equal to their P-R drag evolution time (see eq. [3.31]).

Thus, the solution given by equation (3.36), which is shown in Fig. 3.4a, depends only on the value of η_0. In disks that have high values of η_0 (or equivalently, disks that are very dense), collisions form a central cavity region. The particles that have been removed by collisions are presumably blown out of the system by radiation pressure. Disks with low values of η_0, on the other hand, suffer

minimal collisional loss, and their spatial distribution follows equation (3.33). Note that for a disk of particles with $\beta = \beta_{pr}$ (i.e., one with $\eta_0 = 1$), there is a significant fraction of particles interior to the source.

In a more realistic situation, a source produces particles of a range of sizes at different rates. These particles then collide with each other, resulting in either catastrophic or non-catastrophic collisions. If we approximate a particle's collisional lifetime as being inversely proportional to the number density of particles of the same size as itself, then equation (3.36) can be used to estimate the spatial distribution of particles of different sizes from the same source. Since particles of different sizes have different values of η_0, their spatial distributions are different. This also means that the size distribution of particles in the disk changes with r (although to know what that distribution is, we need to understand the production rates of different sized particles in the source). This is, however, an over-simplified model of the collisional evolution of particles in a disk moving under P-R drag and collisions. A more accurate solution could be found by solving the partial differential continuity equations (eq. [3.35]; where all of the parameters in this equation would now depend on D as well as r) numerically. This would be a very interesting study which could be applied to studying the collisional evolution of particles in the zodiacal cloud, but it is not within the scope of this dissertation.

3.3.3 Evidence from the Zodiacal Cloud

Observations of the zodiacal cloud at 1 AU show that its effective optical depth here is $\tau_{eff} = O(10^{-7})$. Since these particles originated in the asteroid belt at $\sim$ 3 AU, arriving at 1 AU due to the P-R drag evolution of their orbits, the zodiacal cloud's volume density should vary $\propto 1/r$, and its effective optical depth at 3 AU should be similar to that at 1 AU. Assuming zodiacal cloud particles to have a density $\sim$ 2500 kg/m^3 (Leinert & Grün 1990), the cross-sectional area of material in the asteroid belt should be concentrated in particles with $D_{pr} = O(500\ \mu\text{m})$ (eq. [3.32]), for which both the collisional lifetime, and the P-R drag lifetime, is $\sim$ 4 Myr. The cross-sectional area of material at 1 AU is expected to be concentrated in particles smaller than that in the asteroid belt, since many of the larger particles should have been broken up by collisions before they reach the inner solar system. This is in agreement with observations that show the cross-sectional area distribution at 1 AU to peak for particles with $D = 100 - 200\ \mu$m (Leinert & Grün 1990; Love & Brownlee 1993; see Fig. 3.5). The size distribution of particles evolving due to P-R drag should have a size distribution with $q < 11/6$, possibly with q as low as 5/6 (e.g., eq. [3.34]). This is supported by modeling of the brightness of the dust bands in different wavebands which shows that the size distribution of this material is best fitted with $q = 1.43$ (Grogan et al. 2000; see Fig. 3.2); the deviation from $q = 5/6$ is indicative of the collisional evolution of this material.

Also, equation (3.21) with $D_{typ} = 500\ \mu$m, $D_{cc}(D)/D = (10^{-4})^{1/3}$, and $q = 11/6$, predicts that the collisional lifetime of large bodies in the asteroid belt should be:

$$t_{coll} \approx 10^9 \sqrt{D}, \tag{3.37}$$

where t_{coll} is given in years, and D in km. Since the solar system is $\sim 4.5 \times 10^9$ years old, this implies that asteroids larger than $\sim$ 20 km should be primordial asteroids. This is in agreement with more accurate models of the observed size distribution of these asteroids (Durda et al. 1998; see Fig. 3.1). Further evidence of the zodiacal cloud's collisional cascade comes from the dust detector onboard the Ulysses spacecraft, which found evidence of small (submicron) β meteoroids streaming out of the solar system on hyperbolic trajectories that were probably created in collisions between larger bodies in the inner solar system (rather than by sublimation near the Sun) (Wehry & Mann 1999).

3.4 Disk Particle Categories

Disk particles of different sizes can be categorized according to the dominant physical processes affecting their evolution. Particles in the different categories have different lives; i.e., the

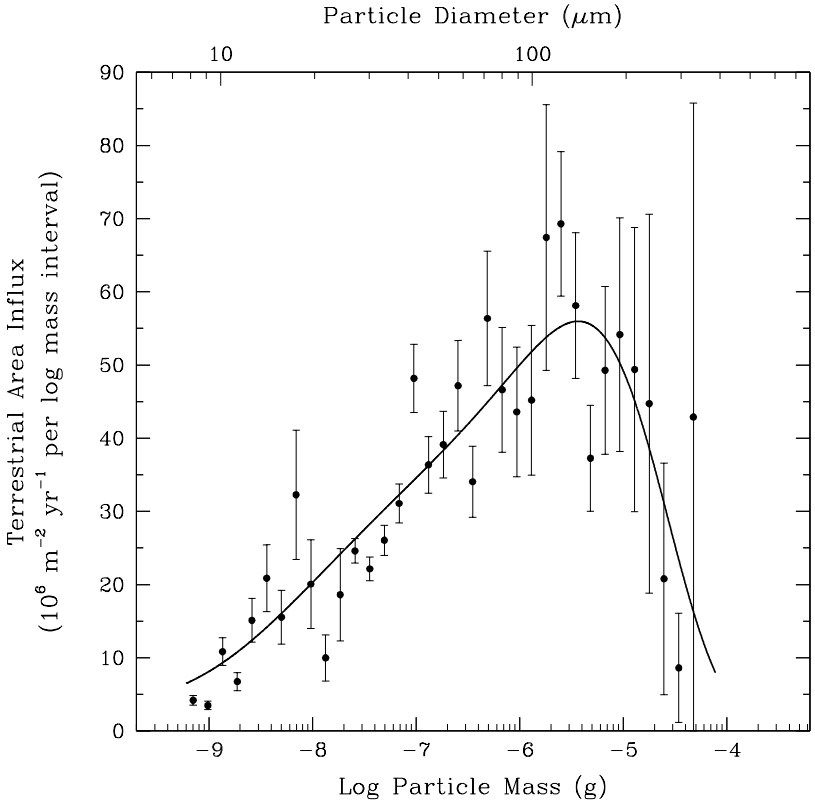

Figure 3.5: Mass of micrometeorites accreted by the Earth annually per log differential particle mass interval (Love & Brownlee 1993). This is indicative of the size-frequency distribution of material in the zodiacal cloud at 1 AU. It is, however, biased towards the type of particle that is preferentially accreted by the Earth (see §4.3 for a further discussion of accretion).

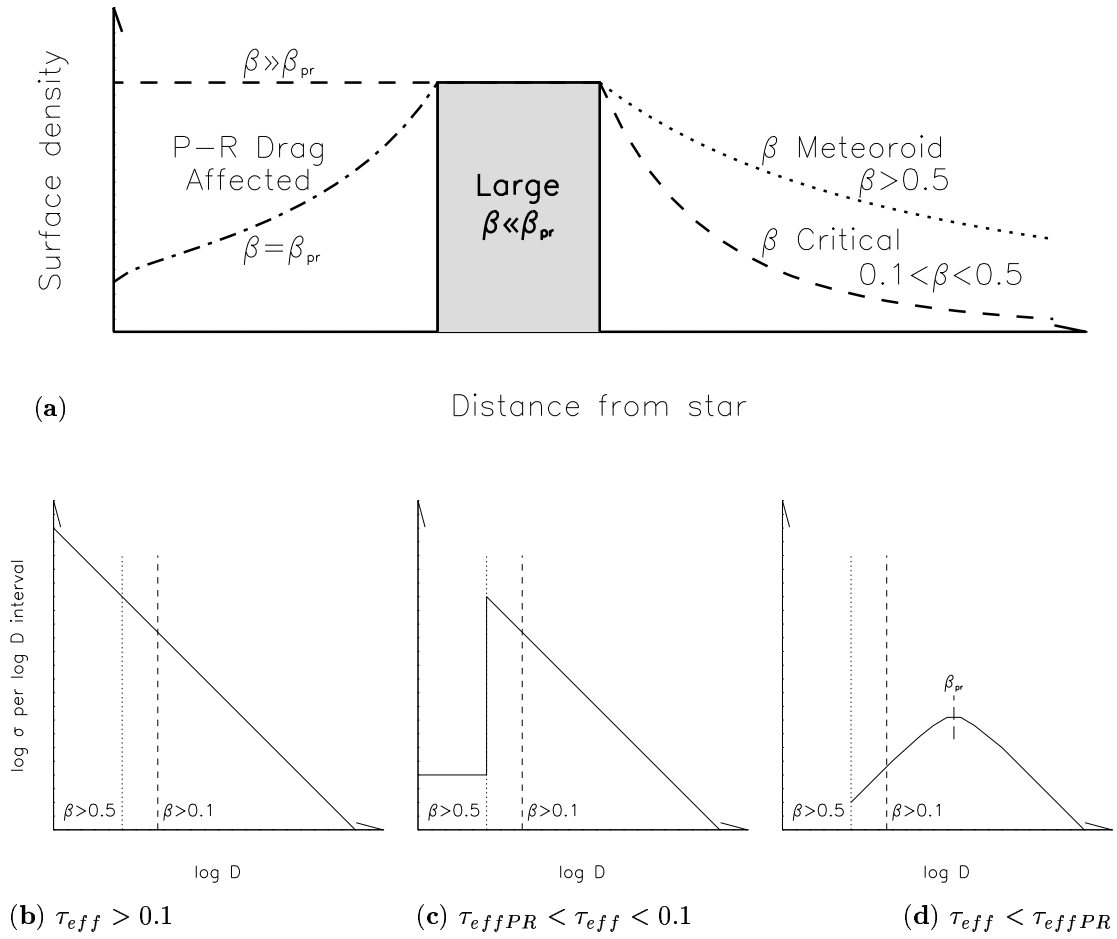

Figure 3.6: The spatial and size distributions of particles in a debris disk comprised of a narrow torus of planetesimals (such as a Kuiper belt-like or asteroid belt-like disk). (**a**) The qualitative functional form of the surface density of particles of different sizes (and hence different β) created by collisions between the planetesimals. The distribution of the planetesimals is shown by the shaded region, which is the same as the distribution of the largest collisional fragments. (**b**), (**c**), and (**d**) The qualitative cross-sectional area distribution in disks of different densities.

way they are created, their dynamical evolution, and the way they are eventually destroyed, are all different. Each of a disk's categories has a different spatial distribution. Which of these categories dominates the disk's observable structure depends on the relative contribution of each to the disk's cross-sectional area (see §2.3). The concept of particle categories is supported by the example of a debris disk comprised of a narrow torus of planetesimals (Fig. 3.6).

3.4.1 Category Definitions

A disk's largest particles, those with $\beta < 0.1$, have orbital elements that are initially the same as, or at least very similar to, those of their parents. Of these large particles, only those with $\beta < \beta_{pr}$ suffer no significant P-R drag evolution to their orbits in their lifetime. These truly large particles continue on the same orbits as those of their ancestors until they collide with a particle large enough to cause a catastrophic collision; the resulting collisional fragments populate the collisional cascade. The spatial distribution of these "large" particles in a disk is its base distribution. The spatial distributions of a disk's smaller particles can only be understood in terms of how they differ from the disk's base distribution (see Fig. 3.6a).

Disk particles with $\beta_{pr} < \beta < 0.1$, spiral in from their parent's orbits due to P-R drag, so that they are closer to the star than their parents by the time of their demise (which could be caused either by collisions or by evaporation close to the star). The spatial distribution of these "P-R drag affected" particles in a disk differs from the disk's base distribution in that it extends closer in to the star. The orbits of particles with $0.1 < \beta < 0.5$ also undergo significant P-R drag evolution before their demise, but their original orbits are already different from those of their parents. The spatial distribution of these "β critical" particles in a disk extends both further out, and further in, from the disk's base distribution. Particles with $\beta > 0.5$ leave their parents on hyperbolic orbits and so are quickly lost from the system. The spatial distribution of these "β meteoroids" in a disk extends further out, but not further in, from the disk's base distribution.

Thus, a disk comprises four particle categories, each of which has a different spatial distribution, although all are inextricably linked to that of the large particles through the collisional cascade. For disks that have $\beta_{pr} > 0.5$, however, i.e., those with $\tau_{eff}(r) > \tau_{effPR}(r)$, where

$$\tau_{effPR}(r) = 10^{-4}\sqrt{(M_\star/M_\odot)(a_\oplus/r)}, \tag{3.38}$$

there is no significant P-R drag evolution of any of its constituent particles. Such disks comprise just three categories, since the P-R drag affected category is empty.

3.4.2 Category Cross-Sectional Area

The size distributions of a disk's large particles, and its P-R drag affected particles, were discussed in §§3.2 and 3.3. These discussions imply that the cross-sectional area of a disk in which there is a population of P-R drag affected particles (see eq. [3.38]) is dominated by particles with $D \approx D_{pr}$ (eq. [3.32]; see Fig. 3.6d). As a first-cut approximation, the size distribution of a disk in which there are no P-R drag affected particles follows equation (3.5) from D_{max} down to $D_{min} = D(\beta = 0.5)$ (see, e.g., eq. [3.19] and Fig. 3.6c), although this is unlikely to be true for the smaller end of this size distribution, since a particle's catastrophic collision rate is affected by the size distribution of particles smaller than itself (Durda & Dermott 1997). The cross-sectional area of such a disk is concentrated in its smallest particles, and the contribution of β critical particles to the disk's total cross-sectional area is given by

$$d\sigma/\sigma_{tot} = [D^{5-3q}]_{D(\beta=0.1)}^{D(\beta=0.5)}/[D^{5-3q}]_{D_{max}}^{D(\beta=0.5)}; \tag{3.39}$$

e.g., if $q = 11/6$, and $\beta \propto 1/D$, this means that half of the disk's cross-sectional area comes from its β critical particles.

Since β meteoroids have hyperbolic orbits, they are expected to contribute little to a disk's cross-sectional area unless they are produced at a high enough rate to replenish their rapid loss from the system. This could be the case if the disk was very dense, since material would pass quickly through the cascade (see Fig. 3.6b); such a disk would undergo considerable mass loss. An estimate of how dense the disk would have to be for this to be the case depends on the assumptions made about the physics of collisions between small particles. For heuristic purposes, it is assumed here that the total cross-sectional area of β meteoroids created by the collisional break-up of a parent body is comparable to that of the parent itself. This is probably an underestimate if the collision is destructive, but an overestimate if the collision is erosive. If this were the case, then the disk's β meteoroids would dominate a disk's cross-sectional area only if their lifetime, which is of the order of the orbital period of their parents, is longer than the lifetime of these parents, which can be approximated by equation (3.18), i.e., only if

$$\tau_{eff}(r) > 0.1. \tag{3.40}$$

In conclusion, from a theoretical stand-point, there are few solid assumptions that can be made about a disk's size distribution. However, it would appear that it is a disk's density that determines the size of particles in which its cross-sectional area is concentrated, and the denser the disk is, the smaller the diameter of particles that its cross-sectional area is concentrated in.

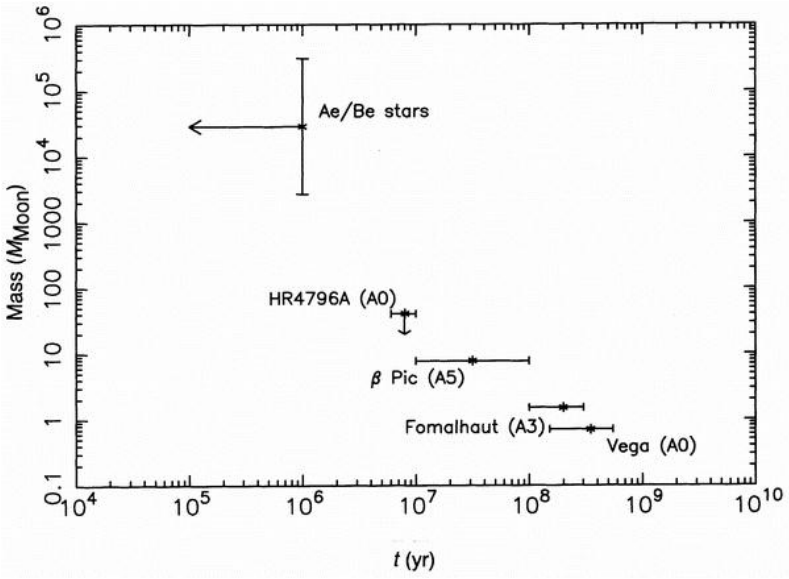

Figure 3.7: Circumstellar dust masses plotted as a function of stellar age (Fig. 2 of Holland et al. 1998).

3.5 Debris Disk Evolution

Collating the available observational information, we see that just as for the protoplanetary disks (Beckwith 1999) there is a trend for older debris disks to be less massive than younger disks (see, e.g., Fig. 3.7). It also appears that the disk emission tends to arise from regions analogous to the Kuiper belt in the solar system (Backman & Paresce 1993), with the region interior to this being relatively (but not necessarily completely) empty, possibly due to the formation of planets, or planetesimals, in the inner disk. Thus, here we consider the evolution of a Kuiper belt disk of planetesimals.

The emission of Kuiper belt-like disks that have different densities are dominated by the emission of different particle categories. The physics affecting the evolution of these disks is also different. For young disks, that have a high optical depth, their emission is dominated by β meteoroids that are the end products of the grinding down of larger planetesimals (see Figs. 3.6a and b). The consequently high mass loss rate results in the decay of the planetesimal population, which causes a reduction in the disk's optical depth, and hence a reduction in the mass loss rate. The optical depth of young debris disks is also reduced by ongoing planet formation. Very young systems cannot have reached dynamical equilibrium, and planetesimals are still lost from source regions through either accretion onto a nascent planet or through scattering onto highly eccentric or inclined orbits, ending up as Oort- or short period-like comets.

The mass loss from a young disk means that eventually it becomes tenuous enough for β critical particles to dominate the disk emission (eq. [3.40]; see Figs. 3.6a and c). As the disk dissipates further (at an ever slowing-pace), P-R drag becomes important, first for the evolution of the disk's β critical particles (eq. [3.38]), then for the evolution of larger particles (eq. [3.32]; see Fig. 3.6d). Throughout these stages, the disk's emission (i.e., the disk's cross-sectional area) comes from particles of increasing size. Also, the outer edge of the disk creeps inwards, as does the inner edge (see Fig. 3.6a). If the particles' P-R drag evolution is not disrupted by a planet at the inner edge of the disk (see Chapter 4), the extent of migration of the inner edge can be shown by considering the solution given by equation (3.36) for a disk with a constant r_0 and D but a decreasing n_0; e.g., Fig. 3.4b shows the distribution of $\beta = 0.1$ particles from a source at 40 AU from a solar mass star that has a variable dust production rate which causes the effective optical depth of the particles at

the source to vary. To understand these latter stages of evolution better, a more complete analysis of the P-R drag evolution with collisions that includes a range of particle sizes is needed (§3.3.2.3).

As the disk gets older, its optical depth (and so its brightness) decreases at all r. Since a disk's collisional mass loss rate, $-\dot{M}$ (where M is the disk's mass) is proportional to the collision rate in the disk, which is proportional to the disk's optical depth, which is roughly proportional to $M^{2/3}$, the disk never totally disappears. For a disk with a current mass of M_1 and a mass loss rate $-\dot{M}_1$ (which can be determined from its optical depth), its mass, M_2, after an elapsed time dt will be:

$$M_2 = M_1(1 - \dot{M}_1 dt/M_1)^{-3}. \tag{3.41}$$

However, a disk will eventually dissipate under the threshold when it is no longer observable with a given detector system, and the disks that are preferentially observed are those in the earlier stages of their evolution, since this is when they are brightest.

The arguments outlined in the last paragraphs apply equally for the evolution of an inner disk, such as one associated with an asteroid-like belt. The zodiacal cloud can be explained as an asteroid belt disk in the latter stages of its evolution, where its P-R drag affected particles reach all the way into the Sun and dominate its thermal emission (see Figs. 3.6a and d). The rate of evolution of the two (inner and outer) components in a disk depends on their stability against gravitational perturbations from the planetary system and the initial density of the planetesimal population. There may also be some interaction between the two populations; β meteoroids and β critical particles from the inner disk may interact with the outer disk, and P-R drag affected particles from the outer disk may interact with the inner disk. Given the myriad of possible outcomes of the planetary formation process, the wavelengths and radial location at which the emission from a disk arises varies from disk to disk, as well as for the same disk at different stages of its evolution.

3.6 The Perturbed Dynamic Disk

In addition to the physical processes described in §§3.1-3.3, the particles of the dynamic disk are affected by a number of perturbing processes. These produce subtle, but perhaps observable, and in some cases maybe dominant, changes in a disk's structure. The dominant perturbing processes in the zodiacal cloud are the secular and resonant gravitational perturbations of the planets. These are discussed in Chapter 4.

Other possible perturbing processes include: stellar wind forces, that, at least for dust in the solar system, effectively increase the value of β for P-R drag (e.g., Leinert & Grün 1990); Lorentz forces acting on charged particles, that, while negligible for particles in the inner solar system, are increasingly important for particles at distances further from the Sun (e.g., Kimura & Mann 1998); interactions with dust from the interstellar medium (e.g., Artymowicz & Clampin 1997); the sublimation of icy dust grains, which is one of the mechanisms that has been suggested as the cause of the inner hole in the HR 4796 disk (Jura et al. 1998); the self gravity of a massive disk, which could have played an important role in determining the evolution of the primordial Kuiper belt (Ward & Hahn 1998); the Yarkovsky force, which may be important for the evolution of intermediate-sized meteorites (e.g., meter-sized) in the asteroid belt (e.g., Farinella et al. 1998); and gas drag, which is important for evolution in a young disk in which the gaseous component of the protoplanetary disk has not yet dissipated (which is thought to occur in $\sim 10^7$ years, Beckwith 1999).

CHAPTER 4
SIGNATURES OF PLANETARY PERTURBATIONS

Consider the structure of a young debris disk. It is thought that by an age of $\sim 10^7$ years, any planets that are to form in the disk should have accumulated most of their final mass (Lissauer 1993). The remainder of their mass, which they should accumulate by $\sim 10^8$ years, comes from a planetesimal population that has already been depleted by the initial growth of the planet. This planetesimal disk (i.e., the debris disk) already has structure that is indicative of the nascent planetary system, since regions close to the orbits of the planets are relatively empty, this material having been accreted onto, or scattered by, the growing planet. Thus the first signature of a planetary system is the large-scale radial distribution of the reservoir of planetesimals that collide to produce the dust that is seen by its thermal emission (or by its scattering of the starlight). In the solar system, the fact that planetesimals are only found in specific regions such as the asteroid belt and the Kuiper belt is indicative of the solar planetary system. However, regions that are relatively empty of planetesimals are only suggestive, rather than demonstrative, of planetary formation, since there could be other reasons for the depletion; i.e., we cannot rely on the planetary formation paradigm to explain the state of a young debris disk.

What we can be certain of, is that any debris particle in a circumstellar disk that is in a system in which there are one or more massive perturbers inevitably has its orbit affected by the gravitational perturbations of these bodies. The consequent evolution of the orbits of individual particles can be used to obtain a quantitative understanding of the effect of these perturbations on the structure of the disk. There are three types of gravitational perturbation from a planetary system that act on the orbit of a disk particle: secular perturbations, resonant perturbations, and close encounter perturbations (such as scattering or accretion). The signatures of planets seen in the solar system debris disk can be attributed to these perturbations: the offset and warp asymmetries are caused by secular perturbations; resonant rings structures are caused by resonant perturbations; and the large scale radial distribution of material is caused by both resonant and close encounter perturbations.

4.1 Secular Perturbations

4.1.1 Perturbation Equations

The gravitational forces from a planetary system that act to perturb the orbit of a particle in the system can be decomposed into the sum of many terms that are described by the particle's disturbing function, R. The long-term average of these forces are the system's secular perturbations, and the terms of the disturbing function that contribute to these secular perturbations, R_{sec}, can be identified as those that do not depend on the mean longitudes of either the planets or the particle (the other forces having periodic variations).

Consider a particle that is orbiting a star of mass $M_\star$, that also has N_{pl} massive, perturbing, bodies orbiting it. This particle has a radiation pressure force acting on it represented by β, and its orbit is described by the elements a, e, I, Ω and $\tilde{\omega}$. To second order in eccentricities and inclinations, the secular terms in the particle's disturbing function are given by (Brouwer & Clemence 1961; Dermott et al. 1985; Dermott & Nicholson 1986; Murray & Dermott 1999):

$$R_{sec} = na^2 \left[\frac{1}{2} A(e^2 - I^2) + \sum_{j=1}^{N_{pl}} [A_j e e_j cos(\tilde{\omega} - \tilde{\omega}_j) + B_j I I_j cos(\Omega - \Omega_j)] \right], \tag{4.1}$$

where $n = (2\pi/t_{year})\sqrt{(M_\star/M_\odot)(1-\beta)(a_\oplus/a)^3}$ is the mean motion of the particle in rad/s, $t_{year} = 2\pi/\sqrt{GM_\odot/a_\oplus^3} = 3.156 \times 10^7$ s is one year measured in seconds, and

$$A = +\frac{n}{4(1-\beta)} \sum_{j=1}^{N_{pl}} \left(\frac{M_j}{M_\star}\right) \alpha_j \overline{\alpha}_j b^1_{3/2}(\alpha_j), \tag{4.2}$$

$$A_j = -\frac{n}{4(1-\beta)} \left(\frac{M_j}{M_\star}\right) \alpha_j \overline{\alpha}_j b^2_{3/2}(\alpha_j), \tag{4.3}$$

$$B_j = +\frac{n}{4(1-\beta)} \left(\frac{M_j}{M_\star}\right) \alpha_j \overline{\alpha}_j b^1_{3/2}(\alpha_j), \tag{4.4}$$

where $\alpha_j = a_j/a$ and $\overline{\alpha}_j = 1$ for $a_j < a$, and $\alpha_j = \overline{\alpha}_j = a/a_j$ for $a_j > a$, and $b^s_{3/2}(\alpha_j) = (\pi)^{-1} \int_0^{2\pi} (1 - 2\alpha_j \cos\psi + \alpha_j^2)^{-3/2} \cos s\psi d\psi$ are the Laplace coefficients ($s = 1, 2$). A, A_j and B_j are in units of rad/s, and R_{sec} is in units of $\mathrm{m}^2/\mathrm{s}^2$.

The effect of these perturbations on the orbital elements of the particle can be found using Lagrange's planetary equations (Brouwer & Clemence 1961; Murray & Dermott 1999). The semi-major axis of the particle remains constant, $\dot{a}_{sec} = 0$, while the variations of its eccentricity and inclination are best described when coupled with the variations of its longitude of pericenter and ascending node using the variables defined by its complex eccentricity, z, and complex inclination, y:

$$z = e * \exp i\tilde{\omega}, \tag{4.5}$$

$$y = I * \exp i\Omega, \tag{4.6}$$

where $i^2 = -1$. Using these variables Lagrange's planetary equations give the orbital element variations due to secular perturbations as:

$$\dot{z}_{sec} = +iAz + i \sum_{j=1}^{N_{pl}} A_j z_j, \tag{4.7}$$

$$\dot{y}_{sec} = -iAy + i \sum_{j=1}^{N_{pl}} B_j y_j, \tag{4.8}$$

where z_j and y_j are the complex eccentricities and inclinations of the perturbers, which have a slow temporal variation due to the secular perturbations of the perturbers on each other (Brouwer & Clemence 1961; Murray & Dermott 1999):

$$z_j(t) = \sum_{k=1}^{N_{pl}} e_{jk} * \exp i(g_k t + \beta_k), \tag{4.9}$$

$$y_j(t) = \sum_{k=1}^{N_{pl}} I_{jk} * \exp i(f_k t + \gamma_k), \tag{4.10}$$

where g_k and f_k are the eigenfrequencies of the perturber system, the coefficients e_{jk} and I_{jk} are the corresponding eigenvectors, and β_k and γ_k are constants found from the initial conditions of the perturber system.

4.1.2 Solution to Perturbation Equations

Ignoring the evolution of a particle's orbital elements due to P-R drag, equations (4.7) and (4.8) can be solved to give the secular evolution of the particle's instantaneous complex eccentricity and inclination (a.k.a. the particle's osculating elements). This secular evolution is decomposed into

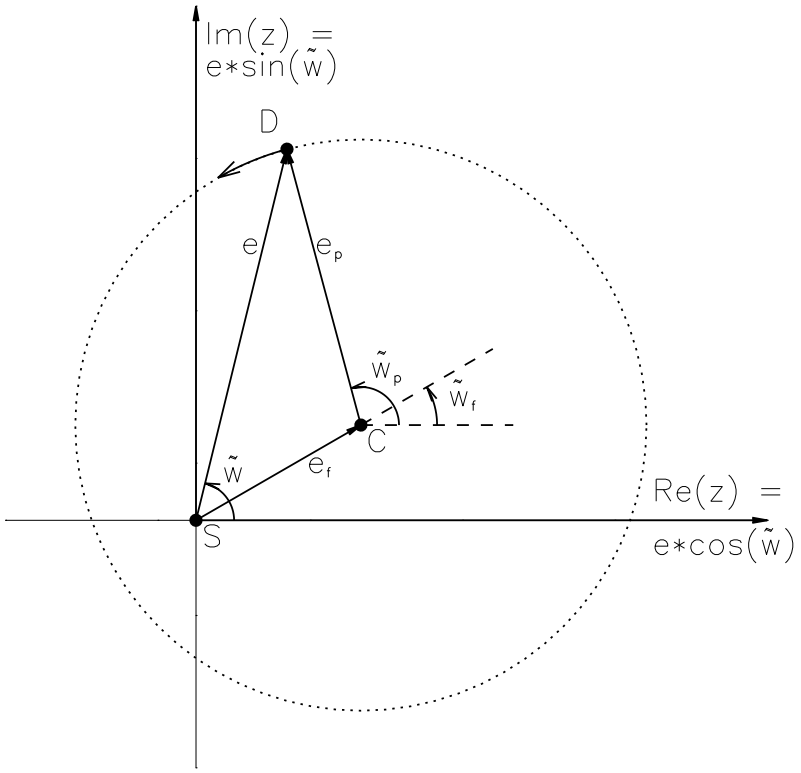

Figure 4.1: The osculating (instantaneous) complex eccentricity, $z = e * \exp i\tilde{\omega} = SD$, of the orbit of a particle in a system with one or more massive perturbers can be resolved vectorially into two components: a forced eccentricity, $z_f = e_f * \exp i\tilde{\omega}_f = SC$, that is imposed on the particle's orbit by the perturbers; and a proper eccentricity, $z_p = e_p * \exp i\tilde{\omega}_p = CD$, that is the particle's intrinsic eccentricity. The secular evolution of its complex eccentricity is to precess counterclockwise around the dotted circle in the figure, although the forced eccentricity may also vary with time. A similar figure applies for the particle's osculating complex inclination, $y = I * \exp i\Omega$.

two distinct time-varying elements — the "forced", subscript f, and "proper", subscript p, elements — that are added vectorially in the complex planes (see Fig. 4.1):

$$z(t) = z_f(t) + z_p(t), \tag{4.11}$$

$$= \sum_{k=1}^{N_{pl}} \left[\frac{\sum_{j=1}^{N_{pl}} A_j e_{jk}}{g_k - A} \right] * \exp i(g_k t + \beta_k) + e_p * \exp i(+At + \beta_0), \tag{4.12}$$

$$y(t) = y_f(t) + y_p(t), \tag{4.13}$$

$$= \sum_{k=1}^{N_{pl}} \left[\frac{\sum_{j=1}^{N_{pl}} B_j I_{jk}}{f_k + A} \right] * \exp i(f_k t + \gamma_k) + I_p * \exp i(-At + \gamma_0), \tag{4.14}$$

where e_p, β_0, and I_p, γ_0 are determined by the particle's initial conditions.

These equations have simple physical and geometrical interpretations. A particle's forced elements, z_f and y_f, depend only on the orbits of the perturbers in the system (that have a slow secular evolution, eqs. [4.9] and [4.10]), as well as on the particle's semimajor axis (which has no secular evolution). Thus, at a time t_0, a particle that is on an orbit with a semimajor axis a, has forced elements imposed on its orbit by the perturbers in the system that are defined by $z_f(a, t_0)$ and $y_f(a, t_0)$. The contribution of the particle's proper elements to its osculating elements, $z(t_0)$ and $y(t_0)$, is then given by $z_p(t_0) = z(t_0) - z_f(a, t_0)$ and $y_p(t_0) = y(t_0) - y_f(a, t_0)$, thus defining

the particle's proper eccentricity, e_p, and proper inclination, I_p, which are its fundamental orbital elements (i.e., those that the particle would have if there were no perturbers in the system), as well as the orientation parameters β_0 and γ_0. Since both the forced elements, and the osculating elements, of collisional fragments are the same as those of their parent (apart from fragments with $\beta > 0.1$), particles from the same family have the same proper elements, e_p and I_p.

The evolution of a particle's proper elements is straight-forward — they precess around circles of fixed radius, e_p and I_p, at a constant rate, A, counterclockwise for z_p, clockwise for y_p. The secular precession timescale depends only on the semimajor axis of the particle's orbit:

$$t_{sec} = 2\pi/At_{year}, \tag{4.15}$$

where t_{sec} is given in years, and A is given in equation (4.2); secular perturbations produce long period variations in a particle's orbital elements (e.g., $t_{sec} = O(0.1$ Myrs) in the asteroid belt). The centers of the circles that the proper elements precess around are the forced elements (see, e.g., Fig. 4.1). Actually the forced elements vary on timescales that are comparable to the precession timescale (eq.[4.15]). Thus, it might appear ambitious to talk of the precession of a particle's osculating elements around circles when its real evolutionary track in the complex eccentricity and complex inclination planes may not be circular at all. The reason it is presented as such is that at any given time, all of the particles at the same semimajor axis precess (at the same rate) around the same forced elements on circles of different radii, and this has consequences for the global distribution of orbital elements (see §4.1.3).

There are two things that are worth mentioning now about a particle's forced elements. If there is just one perturber in the system, $N_{pl} = 1$, its complex eccentricity and complex inclination do not undergo any secular evolution, and the forced elements imposed on a particle in the system are not only constant in time, but also independent of the mass of the perturber:

$$z_f = \left[b^2_{3/2}(\alpha_j)/b^1_{3/2}(\alpha_j)\right] e_j * \exp i\tilde{\omega}_j, \tag{4.16}$$

$$y_f = I_j * \exp i\Omega_j. \tag{4.17}$$

This implies that a body of low mass, such as an asteroid, has as much impact on a particle's orbit as a body of high mass, such as a Jupiter mass planet. The perturbations from a smaller perturber, however, produce longer secular precession timescales (eq. [4.15]):

$$t_{sec} = 4[\alpha_j\overline{\alpha}_j b^1_{3/2}(\alpha_j)(a_\oplus/a)^{3/2}(M_j/M_\star)\sqrt{M_\star/M_\odot}]^{-1}. \tag{4.18}$$

Also, for a very small perturber, the perturbations could be similar in magnitude to those of the disk's self-gravity, which in that case could no longer be ignored. If there is more than one perturber in the system, $N_{pl} > 1$, then particles on orbits for which their precession rate equals one of the system's eigenfrequencies ($A = g_k$, or $-A = f_k$) have infinite forced elements imposed on their orbits, and so are quickly ejected from such a secular resonance region.

The solution given by equations (4.12) and (4.14) accounts for the fact that small particles see a less massive star due to the action of radiation pressure, but not for the P-R drag evolution of their orbits. To find the secular evolution of the orbital elements of a particle that is affected by P-R drag, i.e., one with $\beta_{pr} < \beta < 0.1$, the equations governing the evolution of its complex eccentricity, $\dot{z} = \dot{z}_{sec} - 2.5(\alpha/a^2)z$ (eqs. [3.29] and [4.7]), and its complex inclination, $\dot{y} = \dot{y}_{sec}$ (eq. [4.8]), must both be solved in conjunction with the P-R drag evolution of its semimajor axis (eq. [3.28]). While the solution given by equations (4.12) and (4.14) is no longer applicable, the decomposition of the particle's complex eccentricity and complex inclination into forced and proper elements (eqs. [4.11] and [4.13]), and the physical meaning of these elements, is still valid. However, each of these elements now depends on the particle's dynamical history.

Also, the perturbation theory of §4.1.1 is only valid for particles with small eccentricities; i.e., it is not valid for the evolution of a disk's β critical particles, or its β meteoroids. However, if the evolution of a disk's β critical particles is affected by secular perturbations (i.e., if their lifetime

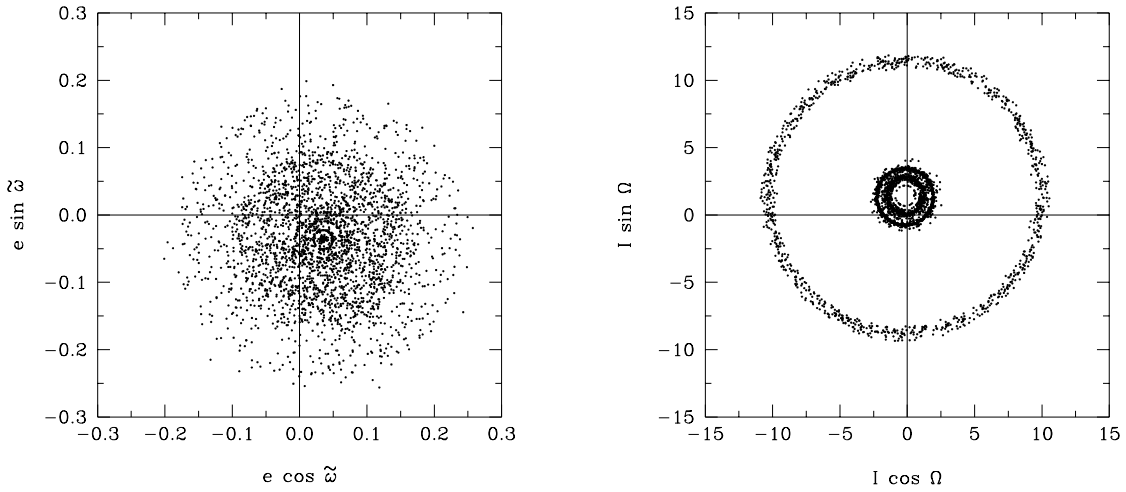

Figure 4.2: The distribution of orbital elements of the asteroids in the families Eos, Themis, and Koronis (Murray & Dermott 1999). The asteroids in the three families have mean semimajor axes of 3.015, 3.148, 2.876 AU, mean proper eccentricities of 0.071, 0.155, 0.047, and mean proper inclinations of 10.2, 1.426, 2.112°, respectively. The secular evolution the asteroids in each of the families results in their orbital elements lying on circles in the complex eccentricity, z, and complex inclination, y, planes, the radii of which are equal to the family's mean proper elements. Since these asteroid families are at similar semimajor axes, the forced elements imposed on their orbits are almost identical, which is why their circles are offset from the origin by the same amount and in the same direction.

is longer than the secular timescale), then it is probably also affected by P-R drag (i.e., their lifetime is probably also longer than the P-R drag timescale), in which case the disk's β critical particles do not contribute much to its observable structure (§§3.3 and 3.4.2). There is no secular evolution to the orbits of β meteoroids because of their short lifetimes.

4.1.3 Offset and Plane of Symmetry of Family Material

The effect of secular perturbations on the structure of a disk can be understood by considering the effect of the secular evolution of the constituent particles' orbits on the distribution of their orbital elements. The perturbation equations of §4.1.1 show that secular pertubations affect only the distribution of disk particles' complex eccentricities, $n(z)$, and complex inclinations, $n(y)$, while having no effect on their size distribution (and hence the division of the disk into its particle categories), or on their semimajor axis distribution (and hence the disk's large-scale radial distribution). Consider the family of collisional fragments originating from a primordial body, the orbital elements of which were described by a, e_p, and I_p.

4.1.3.1 Large ($\beta < 0.1$) Fragments

The orbital elements of the largest fragments, those with $\beta < 0.1$, created in the breakup of the primordial body are initially very close to those of the primordial body; they do not have identical orbits due to the velocity dispersion imparted to the fragments in the collision. The forced elements imposed on the orbits of all of these collisional fragments are the same as those imposed on the primordial body. The secular evolution of their osculating complex eccentricities (eq. [4.12]) and complex inclinations (eq. [4.14]), is to precess about the forced elements (which are

also varying with time), but at slightly different rates (due to their slightly different semimajor axes). A similar argument applies for all particles created by the collisional break-up of these fragments. Thus, after a few precession timescales, the complex eccentricities and complex inclinations of the collisional fragments of this family lie evenly distributed around circles that are centered on $z_f(a,t)$ and $y_f(a,t)$, and that have radii of e_p and I_p (e.g., their complex eccentricities lie on the circle shown in Fig. 4.1), while their semimajor axes are all still close to a. This is seen to be the case in the asteroid belt: there are families of asteroids that have similar a, e_p, and I_p, that are the collisional fragments resulting from the break-up of a much larger asteroid (Hirayama 1918; see Fig. 4.2)

Thus, the distribution of the complex eccentricities, $n(z)$, of these particles, has a distribution of pericenters that is biased towards the orientation in the disk that is defined by $\tilde{\omega}_f$. The consequence of this biased orbital element distribution on the spatial distribution of this family material is best described with the help of Fig. 4.3. This shows how the family material forms a uniform torus of inner radius $a(1-e_p)$ and outer radius $a(1+e_p)$ centered on a point that is displaced from the star by a distance ae_f in a direction away from the forced pericenter, $\tilde{\omega}_f$ (Dermott et al. 1985; Dermott et al. 1998).

The distribution of the complex inclinations, $n(y)$, of these particles is also unevenly distributed. Each particle's complex inclination describes its orbital plane, so $n(y)$ describes the distribution of the orbital planes of the family material; i.e., the out-of-plane distribution of the torus described in the last paragraph (and that shown in Fig. 4.3). Changing the reference plane relative to which the particles' orbital inclinations are defined to that described by y_f, shows that the secular complex inclination distribution of this family material leads to a torus that is symmetrical about the plane described by y_f, the opening angle (half width) of which is described by I_p.

This picture of both the distribution of the orbital elements and the consequent spatial distribution of the large family members is extremely important for understanding the distribution of the smaller members of the family, since the smaller members are created by collisions between the larger members.

4.1.3.2 P-R Drag Affected ($\beta_{pr} < \beta < 0.1$) Fragments

Immediately after they are created, the orbital elements of the P-R drag affected particles are the same as the large members of the family. The dynamical evolution of a wave of these particles, i.e., those that were created at the same time, can be followed by numerical integration to ascertain how the orbital elements of the particles in the wave vary as their semimajor axes decrease due to P-R drag; this is the "particles in a circle" method (Dermott et al. 1992; see Fig. 4.4). It was found that the complex eccentricities and complex inclinations of a wave of particles originating in the asteroid belt remain on circles, and that as the wave's semimajor axis, a_{wave}, decreases: its effective proper eccentricity (the radius of the wave's circle in the complex eccentricity plane) decreases $\propto e_p * (a_{wave}/a)^{5/4}$; its effective proper inclination (the radius of the wave's circle in the complex inclination plane) remains constant at I_p; the distributions of the particles' $\tilde{\omega}_p$ and Ω_p remain random; while its effective forced elements (the centers of the circles in the complex eccentricity and complex inclination planes) have a more complicated variation (Dermott et al. 1992; Liou 1993).

Thus, the orbital element distributions, $n(z)$ and $n(y)$, of P-R drag affected family particles are like that of the large particles, in that they are the addition of z_f and y_f to symmetrical proper element distributions, except that these distributions are different for particles of different sizes as well as for particles at different semimajor axes. This means that the P-R drag affected family particles of a given P-R drag rate that are at a given semimajor axis form a torus with an offset described by their complex forced eccentricity and a plane of symmetry described by their complex forced inclination.

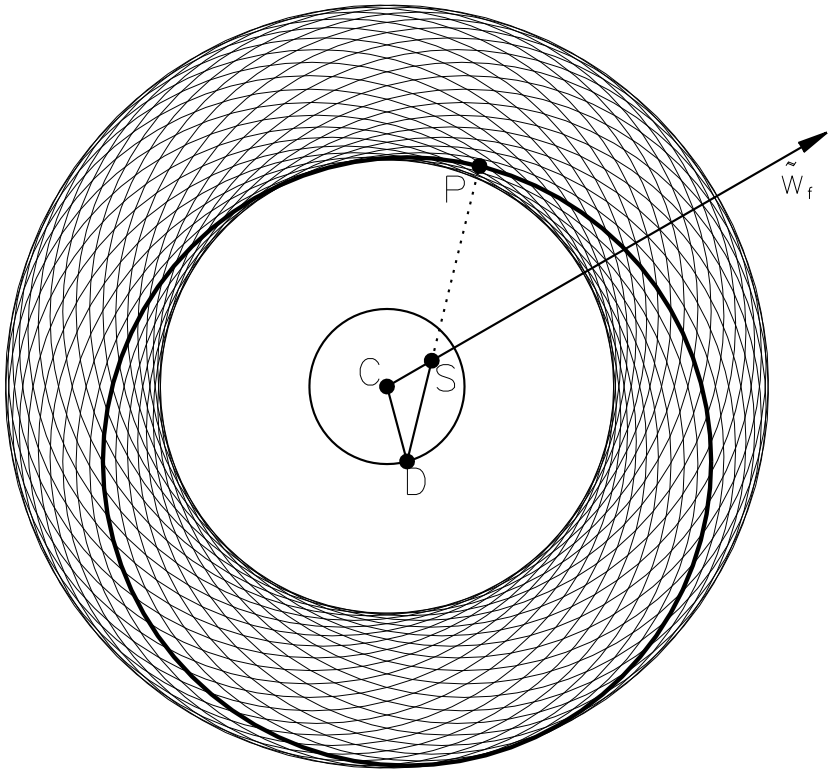

Figure 4.3: Face-on view of the secular spatial distribution of large particles in a disk created by the break-up of one large asteroid. After a few secular precession timescales, these particles still have the same semimajor axis, a, and their complex eccentricities lie evenly distributed around a circle of radius e_p that is centered on the complex forced eccentricity, described by e_f and $\tilde{\omega}$ (such as the dotted circle in Fig. 4.1). The contribution of each particle to the spatial distribution of material in the disk can be described by the elliptical ring of material coincident with the particle's orbit (see §3.1). Here, these elliptical rings have been represented by uniform circles of radius a, with centers that are offset by ae in a direction opposite to the pericenter direction, $\tilde{\omega}$ (this is a valid approximation to first order in the particles' eccentricities). A heavy line is used to highlight the orbital ring with a pericenter located at P, and a displaced circle center located at D, where $DP = a$. The vector SD can be decomposed into its forced and proper components; this is shown by the triangle SCD, where $SD = ae$, $SC = ae_f$, and $CD = ae_p$ (there is a similar triangle in Fig. 4.1). Given that the distribution of $\tilde{\omega}_p$ is random, it follows that the distribution of the rings' centers, D, for this family disk are distributed on a circle of radius ae_p and center C. Thus, the family forms a uniform torus of inner radius $a(1 - e_p)$ and outer radius $a(1 + e_p)$ centered on a point C displaced from the star by a distance ae_f in a direction away from the forced pericenter, $\tilde{\omega}_f$ (Dermott et al. 1985; Dermott et al. 1998).

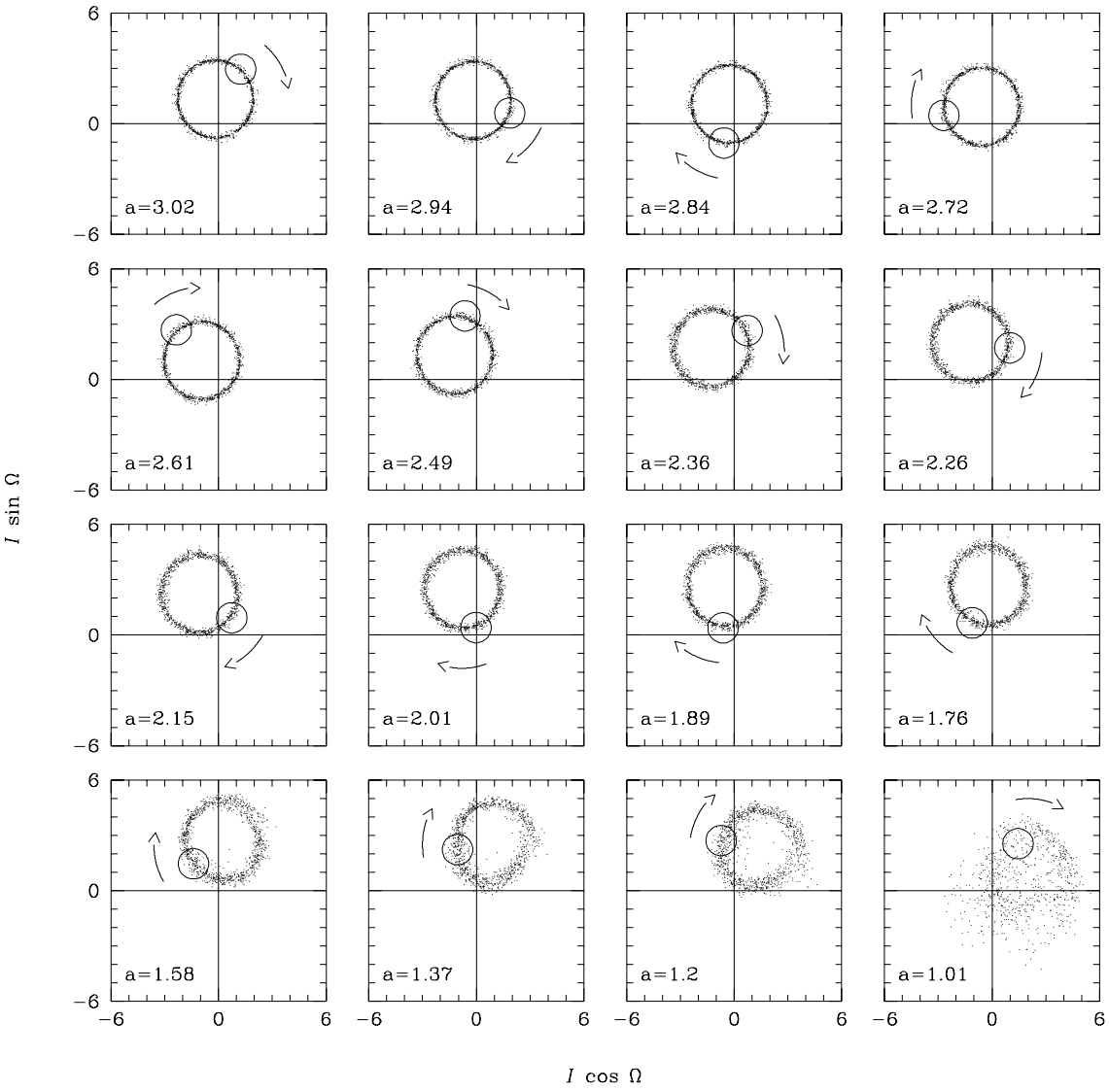

Figure 4.4: The 52,000 year dynamical evolution of a wave of 10 μm particles released at the same time from material in the asteroid family Koronis (Kortenkamp & Dermott 1998). This evolution was found by numerical integration including the gravitational forces of the Sun and the solar system planets, radiation pressure, P-R drag, and the solar wind force. Each panel represents the complex inclination plot at a snapshot of time ($\sim$ 3500 years between each panel) when the mean semimajor axis of the particles is shown in the panels. The circle highlights the dynamical evolution of one particle in the wave.

4.1.3.3 Small ($\beta > 0.1$) Fragments

Consider the β critical particles that are produced at the same time from the population of family particles that have the same $\tilde{\omega}_p$ and Ω_p at that time. This parent population is spread out along the orbit defined by the elements a, e, and $\tilde{\omega}$, which could be one of the rings shown in Fig. 4.3. The average pericenter orientation of these β critical particles, $\langle \tilde{\omega}' \rangle$, is the same as that of the orbit of the larger particles, $\tilde{\omega}$ (obvious because of the symmetry of eq. [3.26] with respect to f). Their pericenter locations are also the same (eq. [3.27]). Thus, the ring shown in Fig. 4.3 defines the inner edge of the disk of β critical particles created in the break-up of large particles on this ring; i.e., their disk is offset by an amount ae in the $\tilde{\omega}$ direction. Consequently, the inner edge of the disk of β critical particles created in the break-up of all large particles in this family is offset by an amount ae_f in the $\tilde{\omega}_f$ direction. This disk has the same plane of symmetry as the families' large particles, since all particle categories from the same family have the same distribution of orbital planes, $n(y)$. Similar arguments apply for the families' β meteoroids.

4.1.4 Offset and Warp of Whole Disk

Consider first of all a disk in which there are no P-R drag affected particles. The tori of material from all of the families that have the same semimajor axis, or equivalently that are at the same distance from the star, have the same offset inner edge, and the same plane of symmetry. This is because their large particles have the same forced elements imposed on their orbits. The complex eccentricities and complex inclinations of the large particles of all of these families lie evenly distributed around circles with the same centers, z_f and y_f, but with a distribution of radii, $n(e_p)$ and $n(I_p)$, that are the distributions of the proper elements of these families (defining the radial width and opening angle of the torus consisting of these families' material).

The whole disk is made up of families with a range of semimajor axes. The families that are at different semimajor axes can have different forced elements imposed on their orbits (depending on the perturbers in the system), and in view of the proper element distributions in the asteroid belt and in the Kuiper belt, they can also have different distributions of proper elements. A disk with a proper inclination distribution that increases with semimajor axis would be flared; protoplanetary disks are both expected (if they are thermally supported) and observed to be flared (Kenyon & Hartmann 1987; Burrows et al. 1996). If the forced eccentricity imposed on the disk is non-zero, which it is if there is at least one perturber in the system that is on a non-circular orbit (eqs. [4.12] and [4.16]), then the disk's center of symmetry is offset from the star. If the forced inclination imposed on the disk is different for families at different semimajor axes, which it is if there are two or more perturbers in the system that are moving on orbits that are not co-planar (eqs. [4.14] and [4.17]), then the disk's plane of symmetry varies with distance from the star; i.e., the disk is warped.

The addition of P-R drag complicates the situation further, since z_f and y_f at a given distance from the star are different for particles from different families as well as for particles of different sizes from the same family. However, for the same reasons as for the larger particles, this orbital element distribution leads to a disk that is both offset and warped.

4.1.5 Physical Understanding of Offset and Warp

There is also a physical explanation for the secular perturbation asymmetries. The secular perturbations of a massive body are equivalent to the gravitational perturbations of the elliptical ring that contains the mass of the perturber spread out along its orbit, the line density of which varies inversely with the speed of the perturber in its orbit (Gauss' averaging method, Brouwer & Clemence 1961; Murray & Dermott 1999). The ring's elliptical shape, as well as its higher line density at the perturber's apocenter, mean that the center of mass of the star-ring system is shifted from the star towards the perturber's apocenter. The focus of the orbits of particles in such a system is offset from the star; i.e., the center of symmetry of a disk in this system is offset from the star. The gravitational perturbations of the ring also point to the plane coincident with the perturber's orbital plane. In systems with two or more perturbers, the system's plane of symmetry (that in

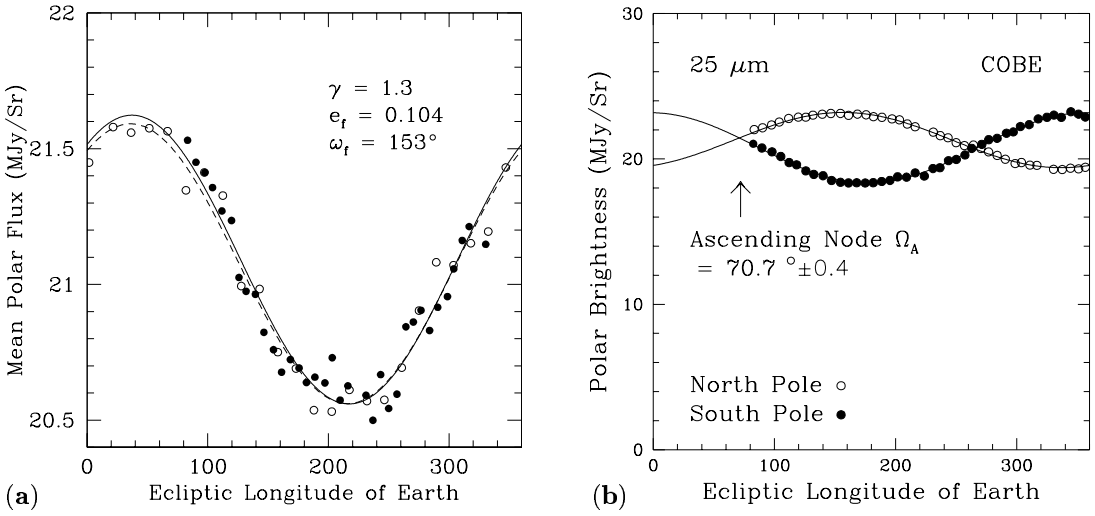

Figure 4.5: COBE observations in the 25 μm waveband of the variation of brightnesses at the North, N, and South, S, ecliptic poles with ecliptic longitude of the Earth, $\lambda_\oplus$ (Dermott et al. 1999). (**a**) shows the mean polar flux, $(N+S)/2$. The COBE observations are shown with the filled circles and the best fit to this observation with the solid line. The fact that $N+S$ is at a minimum at $\lambda_\oplus = 224 \pm 3°$ rather than at the Earth's aphelion, $\lambda_\oplus = 282.9°$, implies that the center of symmetry of the zodiacal cloud is displaced from the Sun. Models for the zodiacal cloud with a number density fall-off $\propto r^{-1.3}$ show that this observation can be explained by the particles having $e_f = 0.104$ and $\tilde{\omega}_f = 153°$ (Dermott et al. 2000); the model observation is shown with the open circles and the dashed line. (**b**) N and S are equal when the Earth is at either the ascending or the descending node of the plane of symmetry of the cloud at 1 AU, giving an ascending node of $70.7 \pm 0.4°$. This plane of symmetry is different from the plane of symmetry of the cloud at distances > 1 AU from the Sun, implying that the cloud is warped.

which the perturbing forces out of this plane cancel) varies with distance from the star; i.e., a disk in such a system is warped.

4.1.6 Observational Evidence of Offset and Warp in the Zodiacal Cloud

Mid-IR geocentric satellite observations (such as the IRAS, COBE, and ISO observations) are dominated by the thermal emission of the zodiacal cloud's P-R drag affected particles in all directions except that of the Galactic plane (Leinert & Grün 1990). Such observations contain detailed information about the spatial structure of the zodiacal cloud, especially since their observing geometry changes throughout the year as the Earth moves around its orbit. Since there are 9 massive perturbers in the solar system, the resulting secular perturbation asymmetries should be apparent in the IRAS, COBE, and ISO data-sets.

Fig. 4.5a shows COBE observations of the sum of the brightnesses in the 25 μm waveband at the north and south ecliptic poles, $(N+S)/2$ (Dermott et al. 1999), where there is no contamination from the Galactic plane. If the zodiacal cloud was rotationally symmetric with the Sun at the center, then the cross-sectional area density of particles in the near Earth region would vary according to $\sigma(r,\theta,\phi) \propto r^{-\gamma} f(\phi)$, where γ is a constant. Because the Earth's orbit is eccentric, geocentric observations sample the zodiacal cloud at different radial distances from the Sun. Thus, the minimum of the $(N+S)/2$ observation is expected to occur either at the Earth's aphelion, $\lambda_\oplus = 282.9°$, or perihelion, $\lambda_\oplus = 102.9°$, depending on whether $\gamma > 1$ or $\gamma < 1$, which is determined by the collisional evolution of particles in the near-Earth region (e.g., Leinert & Grün 1990 discuss the observational evidence and conclude that $\gamma \approx 1.3$ as found by the Helios zodiacal light experiment; see also Kelsall et al. 1998). However, the minimum in the 25 μm waveband observations occurs at $\lambda_\oplus = 224°$, and

a similar result is found in the 12 μm waveband. This is expected only if the Sun is not at the center of symmetry of the zodiacal cloud. Assuming that $\gamma = 1.3$, the observations can be explained if a forced eccentricity of $e_f = 0.103$ with a forced pericenter of $\tilde{\omega}_f = 153°$ is imposed on the particles in the background cloud (Dermott et al. 2000). Parametric models of the zodiacal cloud have also shown the need for an offset to explain the observations (e.g., Kelsall et al. 1998).

Fig. 4.5b shows the variation of the brightnesses of the ecliptic poles with ecliptic longitude of the Earth (Dermott et al. 1999). The north and south polar brightnesses are equal when the Earth is at either the ascending or descending node of the local (at 1 AU) plane of symmetry of the cloud, giving an ascending node of $\Omega_{asc} = 70.7 \pm 0.4°$. However, COBE observations of the latitudes of the peak brightnesses of the zodiacal cloud measured in the directions leading and trailing the Earth's orbital motion give $\Omega_{asc} = 58.4°$ (Dermott et al. 1996). Since such observations sample the cloud external to 1 AU, this implies that the plane of symmetry of the zodiacal cloud varies with heliocentric distance, i.e., that the zodiacal cloud is warped.

To observe the zodiacal cloud's offset and warp asymmetries, an observer outside the solar system, would, at the very least, need an observational resolution greater than the magnitude of these asymmetries; e.g., to observe the offset asymmetry, the observer needs a resolution of $> (ae_f/a_\oplus)/R_\odot$ arcseconds, where the distance from the observer to the Sun, $R_\odot$, is measured in pc. An offset asymmetry would be more readily observable in a disk with a central cavity, since the offset would cause a brightness asymmetry in the emission from the inner edge of the disk (Wyatt et al. 1999; see Chapter 7).

4.2 Resonant Perturbations

A disk particle is subjected to resonant perturbations from a planet either when the particle orbits the star p times for every $p + q$ times that the planet does (the external resonance case), or when the particle orbits $p + q$ times for every p planet orbits (the internal resonance case), where both p and q are integers. The nominal resonance location can be found from Kepler's third law of planetary motion, and for an exterior resonance:

$$a/a_{pl} = \left(\frac{p+q}{p}\right)^{2/3}, \tag{4.19}$$

where a is the semimajor axis of the particle's orbit, and a_{pl} is that of the planet. If the particle also suffers from radiation pressure, there should be an additional factor of $(1-\beta)^{1/3}$ on the right hand side of equation (4.19). The physical reason for the resonance can be understood in terms of its geometry. Repeated encounters between the particle and the planet give the particle's orbit a periodic kick. These can either destabilize the particle's orbit, in which case the particle is quickly ejected from the resonance region, or they can stabilize its orbit, in which case the particle can be said to be trapped in the resonance.

Just as the secular perturbations from a planetary system could be described by the appropriate terms in the particle's disturbing function (§4.1.1), so can the resonant perturbations (see, e.g., Murray & Dermott 1999). Quantitative analysis of the appropriate terms in the particle's disturbing function shows how to define whether or not a particle is in resonance, and shows whether that resonance has a stabilizing or destabilizing effect on the particle's orbit; e.g., a particle is formally said to be in an external $p : p + q$ eccentricity resonance when the resonant argument, ϕ, librates about some mean value rather than circulates through 360°, where

$$\phi = (p+q)\lambda - p\lambda_{pl} - q\tilde{\omega}, \tag{4.20}$$

λ and λ_{pl} are the longitudes of the particle and planet respectively, and $\tilde{\omega}$ is the particle's longitude of pericenter. Resonant phenomena can also be studied using numerical simulations, since a full dynamical integration of a particle's motion as it evolves under the gravitational influence of a star and a planetary system automatically accounts for all types of gravitational perturbation. It is not the aim of this section to give a quantitative analysis of resonant phenomena (for which the reader

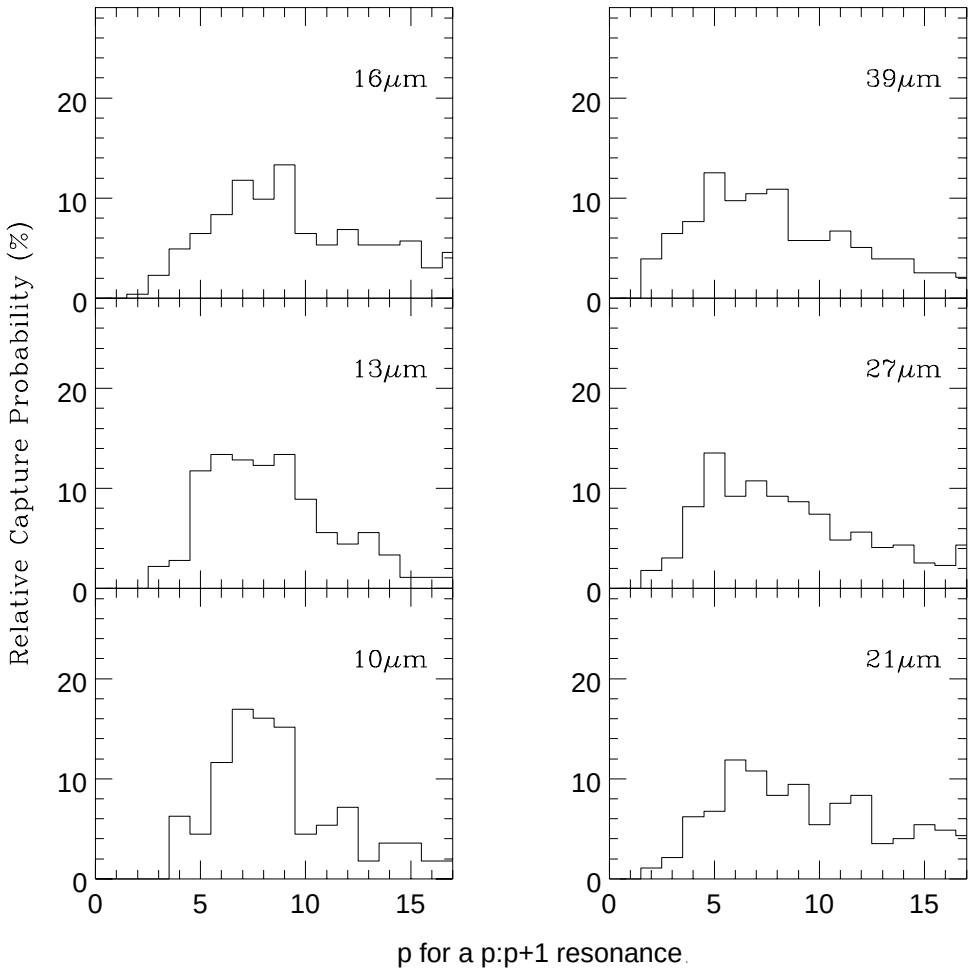

Figure 4.6: The probabilities of trapping into $p : p + 1$ mean motion resonances with the Earth for asteroidal particles of different sizes as they spiral in towards the Sun due to P-R drag (Jayaraman & Dermott 2000). The probabilities are plotted relative to the probability of the particle's capture into all of the first order mean motion resonances, which is approximately 12, 20, 29, 41, 43, and 47 % for the 10, 13, 16, 21, 27, and 39 μm particles respectively.

is referred to texts such as Murray & Dermott 1999), but rather to give a qualitative understanding of the type of resonant phenomena we can expect to observe in circumstellar debris disks that is based upon observations of resonant phenomena in the solar system.

4.2.1 Resonant Trapping due to Particle Migration

As the particles responsible for the thermal emission of the zodiacal cloud spiral in towards the Sun due to P-R drag, they encounter the exterior mean motion resonances of the Earth. A significant proportion of the particles get trapped into these resonances. The strongest resonances, i.e., those with the highest capture probabilities, are the $p : p+1$ resonances. For a particular particle, capture into a resonance is probabilistic and depends on factors such as the particle's P-R drag rate and its orbital parameters at the time of the encounter; e.g., capture is more likely for a particle with a low eccentricity, such as one originating in the asteroid belt, than for one with a high eccentricity, such as one with a cometary origin. Since particles of different sizes have different P-R drag rates, they have different capture probabilities; e.g., larger particles have a lower P-R drag rate and so

have a higher capture probability than smaller particles. The proportion of asteroidal particles of different sizes that get trapped into the different resonances can be ascertained by following their dynamical evolution from the asteroid belt (Dermott et al. 1994; Jayaraman & Dermott 2000; see Fig. 4.6). Note that particles do not get trapped in interior mean motion resonances with Jupiter (Gonczi et al. 1982), because resonant trapping is far more likely to occur when the orbits of a particle and a planet are converging rather than diverging (Dermott et al. 1988).

While a particle is trapped in resonance, the orbital decay due to P-R drag is balanced by the resonant perturbations from the Earth; the semimajor axis of the particle remains roughly constant and its eccentricity increases. Eventually the particle leaves the resonance, either when its eccentricity is high enough to permit a close encounter with the Earth (Weidenschilling & Jackson 1993; Beaugé & Ferraz-Mello 1994), or when its orbit becomes chaotic due to resonance overlap (Dermott et al. 1988; see §4.2.3.1). It then either continues its evolution into the inner solar system or it gets accreted by the Earth. The amount of time a trapped particle remains in resonance depends on the p of the resonance and the eccentricity of the particle when it entered the resonance; e.g., trapping times are shorter for resonances with higher p, since these are closer to the Earth, and so close encounters are more likely to occur (Dermott et al. 1994). Again, trapping time can be found by numerical integration; e.g., it is found that the 13 μm particles that get trapped into the Earth's 2:3 resonance remain there on average for 10,000 years (Jayaraman & Dermott 2000), which is comparable to the time it would have taken them to reach the Sun by P-R drag if they had not been trapped.

The density enhancement at ~ 1 AU caused by the particles trapped in resonance causes the formation of a narrow ring of material that co-orbits with the Earth; this ring was first predicted by Gold (1975), and later by Jackson & Zook (1989). Dermott et al. (1994) used numerical simulations to get a single-sized particle model of the ring, which they later developed to include a range of particle sizes (Jayaraman & Dermott 2000; see Fig. 4.7). The geometry of resonance is such that in the absence of P-R drag, the ring would be symmetrical about the line joining the Earth and the Sun. Its structure would, however, be clumpy, since the ring associated with each resonance is denser at the longitudes where the particles in that ring are at pericenter (Dermott et al. 1994). The action of P-R drag on a resonance's geometry is to introduce a phase lag into the equation of motion that is different for particles with different P-R drag rates, as well as for resonances with different p. The result is that the pericenters of the particles trapped in the ring bunch together behind the Earth, while the pericenters in front of the Earth are dispersed. This causes the formation of a trailing cloud that follows the Earth in its motion (see Fig. 4.7) that is estimated to have a size of $\sim 0.2^3$ AU^3 and to have a number density $\sim 10\%$ above the background (Dermott et al. 1994).

Since the trailing cloud is located permanently in the Earth's wake, the brightness of the zodiacal cloud in the direction behind the Earth's motion is always brighter than that of the Earth's motion. This observational manifestation of the resonant ring was discovered in the IRAS data-set (Dermott et al. 1994). The discovery of the Earth's resonant ring was later confirmed in the COBE observations (Reach et al. 1995). In theory, the other terrestrial planets could also have resonant rings of asteroidal material co-orbiting with them (Dermott et al. 1994), although these remain to be detected, and their expected brightness has yet to be determined. Dust particles created in the Kuiper belt that are spiraling in towards the Sun due to P-R drag could also be trapped into resonance with Neptune (Liou & Zook 1999).

If the P-R drag affected particles of an exosolar disk evolve past a planet in the disk, an asymmetric resonant ring structure could result. Observations of such a structure could be modeled using the same techniques that were used to model the Earth's resonant ring (Dermott et al. 1994; Jayaraman & Dermott 2000), possibly allowing us to determine the presence, location, and even the mass of the perturbing planet (Dermott et al. 1998). However, calculations show that when viewed from a distant point in space normal to the ecliptic plane, the Earth's "wake" would only have an IR signal $O(0.1)$ times that of the Earth (Backman 1998). So, regardless of the resolution requirements, if one were to observe the solar system from outside, it would be easier to detect the Earth directly than to infer its existence from the structure of the zodiacal cloud. This may not be

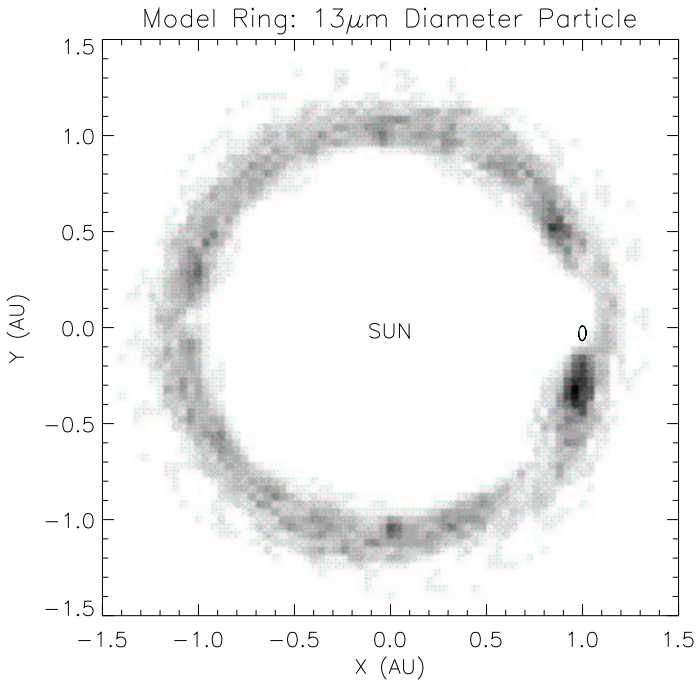

Figure 4.7: Face-on view of a model of the 13 μm particles trapped in the Earth's resonant ring (Jayaraman & Dermott 2000). This is plotted in the reference frame rotating with the Earth's mean motion; i.e., this ring-like structure co-orbits with the Earth. The epicyclic motion of the Earth is shown by the small ellipse 1 AU to the right of the Sun.

true of dust from the Kuiper belt. If this dust were plentiful enough to be observable, an exosolar observer could infer the existence of Neptune and one other giant planet in the inner solar system (Liou & Zook 1999). Also, an extrasolar terrestrial planet resonant ring could be brighter than the Earth's resonant ring if the density of the background cloud were greater than the zodiacal cloud.

4.2.2 Resonant Trapping due to Planetary Migration

The distribution of known Kuiper belt objects is distinctly non-random and shows very pronounced resonant structure (Jewitt 1999; see Fig. 4.8). About one third of the observed Kuiper belt objects are, just like Pluto, in the 2:3 mean motion resonance with Neptune, which is located at $a = 39.4$ AU; these bodies are known as "Plutinos". The Plutinos have high orbital eccentricities which puts some of their pericenters within the orbit of Neptune. However, close encounters with Neptune are prevented by the geometry of the resonance; i.e., the resonance has a stabilizing effect on their orbits. There is almost no Kuiper belt material on orbits with semimajor axes interior to the 2:3 resonance. There may also be a significant fraction in the 1:2 resonance, although these objects would be more difficult to detect because of their faintness. The other two thirds of the Kuiper belt objects are known as "Classical" objects. These are characterized by their semimajor axes, which lie between 42 and 47 AU, and their low eccentricities (which means they do not suffer close encounters with Neptune) and inclinations. We are also now beginning to see another population of Kuiper belt objects, the "Scattered" objects, which are those that are supposed to have been scattered by Neptune.

An explanation of the origin of this detailed structure is important, since it can provide an insight into the last stages of the planetary formation process in the solar system (e.g., Hahn & Malhotra 1999). It is especially important, since the emission from debris disks appears to originate from analogous Kuiper belt regions (Backman & Paresce 1993). In the final stages of the formation

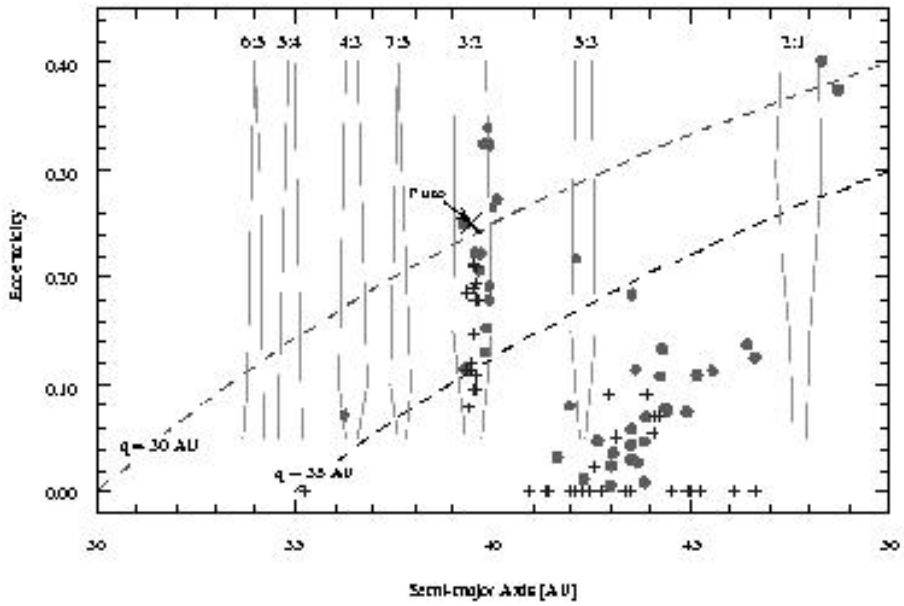

Figure 4.8: Semimajor axis vs. orbital eccentricity plot for the known Kuiper belt objects (Jewitt 1999). The solid circles denote multi-opposition objects and the pluses denote single opposition objects. The approximate boundaries of dominant resonances with Neptune are shown (Malhotra 1995). The dashed lines indiacte the loci of orbits that have perihelion distance 30 and 35 AU.

of the solar system, the residual planetesimal population was cleared (apart from those planetesimals that still reside in the asteroid belt) due to the gravitational perturbations of the fully-formed giant planets. The consequent exchange of orbital energy and angular momentum is expected to result in the radial migration of the orbits of the giant planets (Fernández & Ip 1984). The extent and rate of this migration depends on the mass of the residual planetesimal disk, with the migration being stronger for more massive disks. Numerical simulations of this process show that the orbits of Saturn, Uranus, and Neptune migrated radially outwards, while that of Jupiter migrated slightly inwards (Hahn & Malhotra 1999).

The expansion of Neptune's orbit meant that the planetesimals beyond its orbit ended up on converging orbits with Neptune's first-order mean motion resonances. This allowed the possibility of them being captured into these resonances. This resonance sweeping explains the large number of objects trapped in the 2:3 resonance, as well as explaining the large eccentricities of these objects (Gomes 1997b), and predicts that a similar amount of objects could be trapped in the 1:2 resonance (Malhotra 1995). It also provides a natural explanation for the other populations of Kuiper belt objects, as well as an explanation for the formation of the Oort cloud of comets (Hahn & Malhotra 1999). Hahn & Malhotra (1999) showed that a mass of $\sim 50 M_\oplus$ for the residual disk is required to expand Neptune's orbit by ~ 7 AU which would pump Plutino eccentricities up to ~ 0.3, and they estimated that $\sim 12 M_\oplus$ of this material would be deposited in the Oort cloud, of which only $\sim 4 M_\oplus$ would remain today. However, there are still many issues to deal with when studying the structure of the young Kuiper belt regions. For example, if the disk was very massive, then the interaction of Neptune with the self-gravitating disk could set up apsidal density waves, which would both cause disk structure, and damp the eccentricity of Neptune (Ward & Hahn 1998). Also, density waves launched at mean motion resonances would exert a torque on Neptune's orbit opposing its radial migration (Goldreich & Tremaine 1980).

Just as for the Earth's resonant ring, the geometry of particles trapped in Neptune's resonances is such they create clumpy patterns that co-orbit with the planet. In this instance, however, there is no phase lag, since the P-R drag force acting on the Kuiper belt objects is minimal, so the

resulting resonant ring structure has mirror symmetry about the line joining Neptune and the Sun. The geometry of the orbits of Kuiper belt objects trapped in the 2:3 resonance means that they are expected to be most densely concentrated 90° in front of and behind the location of Neptune, while those in the 1:2 resonance are expected to be concentrated 180° from Neptune. If the debris disks really are analogue Kuiper belts, then some of the large particles that are colliding to create the dust seen by its emission could have undergone the same fate as the Kuiper belt objects. This could cause the emission to have large-scale observable asymmetries that co-orbit with the outermost planet in the system. A ring with all of its particles trapped in the 1:2 and 2:3 resonances with a planet would have three lobes of emission, with the planet residing in an empty fourth lobe.

4.2.3 Resonance Removal Mechanisms

In a planetary system, there are stable regions where large particles can remain undisturbed over the age of the system, and unstable regions where planetary perturbations cause any particles in these regions to be quickly removed. Numerical integrations over the age of the solar system confer with observations that show that the only stable regions in the solar system are the asteroid belt and the Kuiper belt (e.g., Duncan et al. 1989), and that the asteroid belt itself has regions of instability. The regions of instability in the solar system can be explained analytically as the consequence of resonant mechanisms, and these arguments can be applied to explain large-scale radial distribution of large particles in exosolar disks.

4.2.3.1 Resonance Overlap

Close to the orbit of a planet, the planet's first-order mean motion resonances are so tightly packed that the libration widths of the individual resonances overlap (i.e., a particle in this region can have two different resonant arguments, eq.[4.20], that are librating at the same time), and this causes the particle's orbit to be chaotic. Resonance overlap causes material on orbits within a radial width

$$dr \approx 1.3 a_{pl} (M_{pl}/M_\star)^{2/7} \tag{4.21}$$

about a planet's orbit get scattered onto highly eccentric orbits within about 1000 orbital periods (Wisdom 1980).

4.2.3.2 Resonance Gaps

It was noticed that the distribution of the orbits of asteroids in the asteroid belt contains structure; there are significantly fewer asteroids with semimajor axes close to some of Jupiter's interior resonances (Kirkwood 1876). These Kirkwood gaps were later shown to be truly associated with the resonances, since they encompass the specific regions where a particle's resonant argument (eq. [4.20]) is librating rather than circulating (Dermott & Murray 1983). The cause of the gaps has been shown, at least for the 1:3 resonance (e.g., Wisdom 1982), to be due to the chaotic nature of orbits in these resonances; i.e., the eccentricity of a particle in the resonance is pumped up until it is eventually removed from the resonance by a close planetary encounter.

4.2.3.3 Secular Resonance

It was already mentioned in §4.1.2 that material cannot reside in regions of secular resonance (those regions which cover the range of semimajor axes where $e_f, I_f \rightarrow \infty$). The current asteroid belt is truncated interior to a secular resonance at 2 AU. If the orbits of the giant planets suffered radial migration (Hahn & Malhotra 1999), then the locations of the solar planetary system's secular resonances will have swept through a wide range of semimajor axes in the primordial asteroid belt, pumping up the eccentricities and inclinations of material there. This could have inhibited planetary formation in the asteroid belt and could explain the current distribution of the asteroids' eccentricities and inclinations (Gomes 1997a). Similarly, secular resonance sweeping in the primitive

solar nebula has been invoked to explain the dearth of asteroids between the 2:1 and 3:2 resonance with Jupiter (Lecar & Franklin 1997).

4.3 Accretion

Accretion processes are very important during the initial stages of planetary formation, since this is the method by which planetesimals grow into planets. At the end of planetary formation, however, accretion should be minimal, since the source of accretion material close to the planet should be much depleted. However, material can be transported into a planet's accretion zone by P-R drag. While the resulting increase in the planet's mass is likely to be insignificant, the loss of the P-R drag affected particles from the debris disk could be important observationally. In the absence of collisional or accretion loss, the P-R drag affected particles from a particular source extend all the way in to the star. Accretion could cause the formation of an inner hole in such a disk. It is therefore relevant to question how much material that is set to evolve past a planet due to P-R drag survives without being accreted onto the planet.

A simple estimate for the proportion of particles lost in such a way can be obtained by considering the P-R drag evolution of a torus of particles with orbital elements a, e, I, and random Ω, $\tilde{\omega}$ and λ; the volume of this torus is $V_{tor} = 8\pi a^3 e \sin I$ (Sykes 1990). In the time it takes for the torus to pass the planet, $\Delta t = (1602/\beta)(M_\odot/M_\star)(a_{pl}/a_\oplus)^2 e$ yrs, the planet accretes a volume of dust given by (Kessler 1981): $V_{acc} = \sigma_{cap} v_{rel} \Delta t$, where $\sigma_{cap} = \pi R_{pl}^2 (1 + v_e^2/v_{rel}^2)$ is the capture cross-sectional area, R_{pl} is the radius of the planet, $v_e = \sqrt{2GM_{pl}/R_{pl}}$ is the escape velocity of the planet, and v_{rel} is the mean relative velocity of encounter between the planet and the particles. Thus, the proportion of dust accreted onto the planet, $P = V_{acc}/V_{tor}$, is given by:

$$P \approx \frac{12}{\beta\sqrt{1-\beta}} \left(\frac{M_\odot}{M_\star}\right)^{3/2} \left(\frac{M_{pl}}{M_\odot}\right)^{4/3} \left(\frac{a_\oplus}{a_{pl}}\right)^{1/2} \left(\frac{\rho_J}{\rho_{pl}}\right)^{1/3} g(e, I), \tag{4.22}$$

where $\rho_J = 1330$ kg/m^3 is the mean density of Jupiter, $g(e, I) = [(v_{rel}/v) \sin I]^{-1}$, and v is the velocity of the particle.

For a massive enough planet, $P = 1$ for $\beta < 0.5$, implying that no material can pass it, and an inner hole can be formed. However, a planet that is likely to accrete much of the material that passes it is also likely to trap the particles into a resonant ring. This could affect the calculation of the accretion rate, although it is not immediately obvious whether it would make accretion easier or harder. It is thought that resonance trapping helps the accretion process, since trapped particles may leave the resonance upon a close encounter with the planet (e.g., Kortenkamp & Dermott 1998).

CHAPTER 5
DISK PARTICLE OPTICAL PROPERTIES

In order to model circumstellar debris disk observations, we need a model for the optical properties of the constituent particles (§2.5). Essentially, we need a method of finding the variation of the optical coefficients, Q_{abs} and Q_{pr}, with wavelength for a particle of a given diameter, D. First, we need to know the composition of the grains. This defines the optical constants of the grain material (or materials), i.e., the variation of the complex refractive index with wavelength:

$$m(\lambda) = m^{'} + im^{"}. \tag{5.1}$$

The optical constants for a given material can be found by some combination of laboratory measurements and theoretical analysis; e.g., the real part, $m^{'}$ can be calculated from the imaginary part, $m^{"}$, using the Kramers-Kronig relation (Bohren & Huffman 1983). Second, we need to know the morphology of the grains. Finally, we need to use a light scattering theory (see, e.g., Bohren & Huffman 1983) to ascertain how these grains interact with incident light to determine their optical coefficients.

To understand the composition and morphology of debris disk grains, we need to consider their physical origin. The grains described in Chapter 3 are created by the collisional break-up of debris material (such as asteroids or comets) left over at the end of the planetary formation process in the disk. Thus, the grains have a long history that can be traced back to the dust grains in the diffuse interstellar medium. Presumably, interstellar grains can also be traced back to their creation in events such as condensation in the outflow from cool supergiant stars. Observations of the grain populations at different stages in this evolutionary cycle, from diffuse interstellar medium to molecular cloud core to protoplanetary disk to debris disk, can be pieced together to form an understanding of the factors affecting their ultimate composition and morphology. Again, the solar system provides one of the best opportunities for studying debris disk grains, since it is the only system for which we have actual samples of the grains.

5.1 Interstellar Dust Grains

Information about the physical and chemical nature of interstellar dust grains (composition, size, shape, and alignment) can be gleaned from observations of interstellar continuum extinction and polarization from the NIR to FUV (e.g., Li & Greenberg 1997), as well as from dust thermal emission. Spectral features in the interstellar extinction law identify three major dust populations.

First, there is a population of elongated particles with a silicate core, and an organic refractory mantle that are a few tenths of a micron in size (e.g., Li & Greenberg 1997). The presence of silicates is noticeable because of strong absorption/emission features in the extinction at about 10 and 20 μm that are characteristic of Si-O stretching and O-Si-O bending modes. These silicates could not be bare (i.e., have no mantle, such as those proposed by Draine & Lee 1984), because their destruction rate in the interstellar medium is too high compared with their production rate. An organic refractory mantle accreted onto the silicate core protects the core from being destroyed; this material is also responsible for the 3.4 μm extinction feature. The mantle material originally comprised of ices of simple chemical compounds, but billions of years of UV photoprocessing changed the ice mixture into a carbon-rich, oxygen-poor refractory material containing many different organic molecules. These core-mantle grains were shown to be a few tenths of a micron in size and have to be elongated by a factor of about 2:1 to fit the NIR extinction polarization (Li & Greenberg 1997).

There is also a separate population of grains that are responsible for the hump in the interstellar extinction at 2200 Å. While the exact nature of these grains is unknown, they are generally believed to be small < 0.01 μm carbonaceous grains (e.g., Li & Greenberg 1997). It has been speculated that these grains could be made of graphite (e.g., Draine & Lee 1984), however, the carbon in the interstellar medium is produced in carbon stars that have amorphous not graphitic carbon in their circumstellar envelopes. Further, the precise location of the hump is very sensitive to grain properties if graphite grains are assumed, which is inconsistent with observations. The final population of grains are those responsible for the FUV extinction. These are likely to be Polycyclic Aromatic Hydrocarbons (PAHs), which are small < 10 Å thermally spiking grains.

A unified model for interstellar dust that incorporates all three components can simultaneously fit the observed interstellar extinction and polarization (Li & Greenberg 1997). This model for interstellar grains is consistent with constraints on the abundance of the condensable atoms (O, C, N, Mg, Si, Fe) in interstellar dust relative to elemental hydrogen, $[X/H]_{dust}$. This constraint states that the abundance of a particular element in the dust cannot be greater than the difference between its cosmic abundance in the interstellar medium, $[X/H]^{ism}_{cosmic}$, and its abundance observed there in the gas phase, $[X/H]^{ism}_{gas}$. Cosmic abundances can be estimated from those of the solar system. There is, however, evidence that suggests that solar abundances of O, C, and N are above that of the interstellar medium in general. Such an overabundance could have occurred due to the injection of nucleosynthetic products by a nearby supernova, or from a decreasing rate of type II supernovae that resulted in a secular decrease in the heavier elements in the last 5 billion years. There is also evidence that abundances are not uniform in the galaxy, with the inner regions of the galaxy having a greater abundance of heavier elements. Mixing should, however, have maintained some level of uniformity over the local (within a few kpc) interstellar medium. Gas phase abundances can be estimated from UV spectral observations of background objects, which appear to give consistent results along different lines of sight.

5.2 Primordial Cometary Grains

In the process of the formation of molecular cloud cores, and subsequently protoplanetary disks, some of the species that were in the gas phase in the interstellar medium condense onto the refractory grains to form an outer mantle of volatile ices (e.g., Pollack et al. 1994), within which are embedded hundreds of the small carbonaceous particles (e.g., Greenberg & Hage 1990). The widespread occurrence of a feature near 3.0 μm in the infrared spectra of molecular cloud cores that could arise from the O-H stretch fundamental indicates that H_2O ice is the dominant ice in the outer mantle. The grains in protoplanetary disks are different from those in molecular cloud cores due to chemical reactions that process the grains as they pass through the shock interface between the two. In particular, these reactions increase the amount of H_2O and SiO_2 in the disks (Pollack et al. 1994). In the colder outer portions of protoplanetary disks, further condensation of the gaseous components can occur, while in the warmer inner portions, some of the grain species sublimate or are chemically transformed.

Comets are widely recognized to be the most primitive bodies in the solar system. The currently observed coma grains can be linked to their interstellar origin through models of how the grains were formed (Greenberg & Hage 1990; Greenberg 1998; see Fig. 5.1). The formation of a comet nucleus starts with the aggregation of the protosolar nebula particles. The proposed tangled "bird's nest" structure of these aggregates (Greenberg & Gustafson 1981) would provide the aggregates with rigidity. These aggregates then coalesce to form the comet. When the comet approaches the Sun, the icy mantle, and possibly part of the organic refractory mantle, of the individual aggregates evaporate leaving porous aggregate particles, which are lifted from the surface of the comet to become the coma grains. If the comet reaches close enough to the Sun, some of the silicate core may be crystallized (Greenberg 1998). The mass fractions of the various components of the protosolar nebula grains, and hence the comet nucleus, can be estimated from models for the composition of the interstellar dust (e.g., Li & Greenberg 1997), and observations of the solar

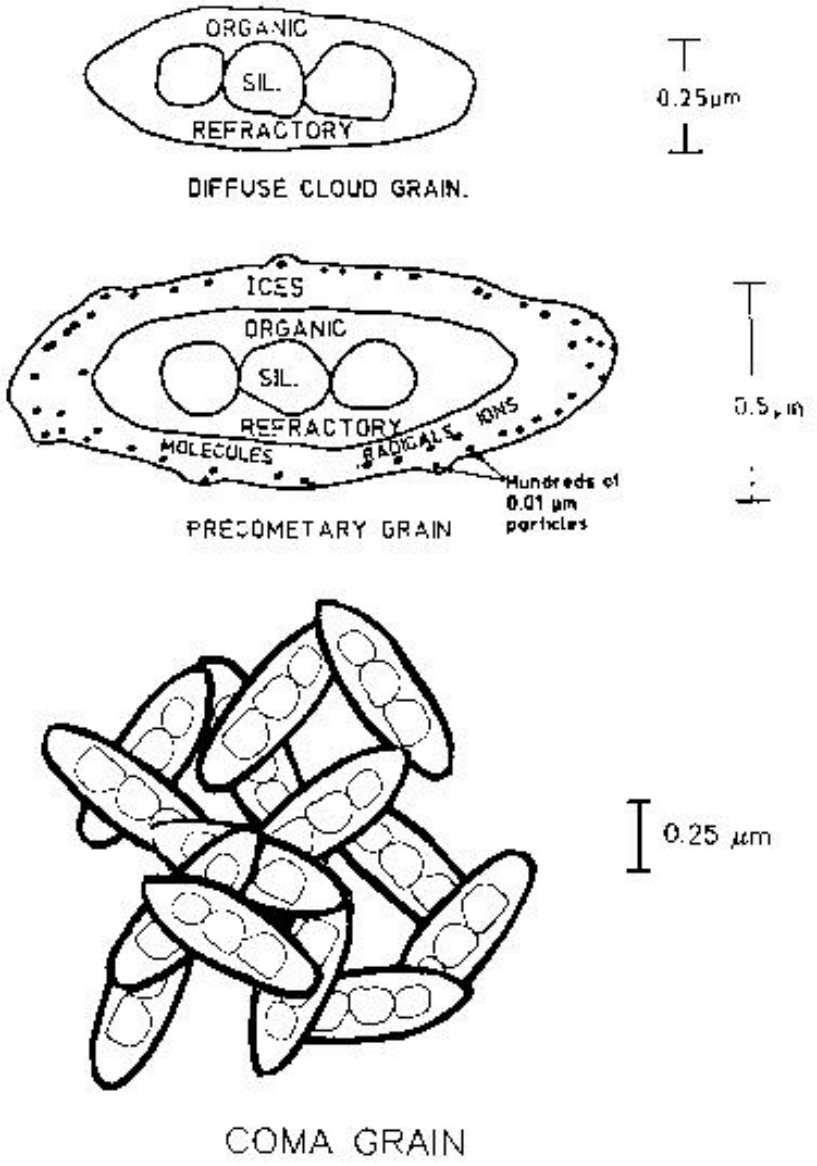

Figure 5.1: The evolutionary history from interstellar grains to cometary grains (Greenberg & Hage 1990). *Top*: Schematic of an interstellar dust grain which consists of a core of silicates and a mantle of organic refractory material. *Middle*: An interstellar grain as it would appear in the protosolar dust cloud after accretion of gases onto its surface. These grains make up a comet. *Bottom*: Schematic of a porous coma grain as it would appear according to the interstellar dust model.

abundance (Greenberg 1998). These can be used to estimate the density and porosity of coma grains which can be compared with observed meteor and nucleus densities. Modeling the optical properties of these particles constrains the grain properties from spectral observations of cometary comae. The evidence supports this model of grain formation (e.g., 0.1 μm particles have been shown to be the basic constituents of the coma aggregates), and indicates that the coma grains have a high porosity of between 0.93 and 0.975 (Greenberg & Hage 1990).

5.3 Zodiacal Dust

Interplanetary dust particles (IDPs) in the zodiacal cloud originate in both comets and asteroids (see, e.g., Leinert & Grün 1990; Gustafson 1994). The composition and morphology of cometary coma grains was discussed in §5.2. The composition of the solar system asteroids ranges from the comet-like D and P types found at the outer edge of the main belt, to the less pristine C and S types further in. This gradation could either be a consequence of the primordial properties of the solar nebula, or of a nearby supernova which either restructured these asteroids or affected the solar abundance in the nebula. Asteroids have porosities of between 0.2 and 0.3 which means that they are much denser than comets. They are supposed to have formed through repeated collisions between chondrules of partially melted interstellar grains which resulted in the observed compaction. Asteroidal grains should therefore be more compact than cometary grains. If the cometary grains seen in the zodiacal cloud are those created by the collisional break-up of a comet at the end of its active life, rather than by their ejection in the coma, then these too could be more compact than the cometary coma grains.

IDPs have been collected in the Earth's stratosphere, and while this is bound to be a selective example of those in the zodiacal cloud as a whole (e.g., due to either the preferential accretion of particles on circular orbits or the low survival probability of loosely packed aggregates), the collected samples do provide us with much information about the elemental composition and structure of IDPs. Most of the collected IDPs are chondritic, either carbonaceous or silicate, with approximately solar composition, and often appear to be aggregates of smaller more or less spherical silicate particles of about 0.1 μm size, which is suggestive of an interstellar origin. Some of the aggregates have high porosity, such as those expected to be of cometary origin, while others are densely packed, such as would be expected from particles created in collisions between asteroids. The aggregates are roughly equidimensional which is consistent with the morphology of lunar microcraters.

5.4 Debris Disk Dust

The most obvious place to search for an understanding of the composition and morphology of debris disk particles is in observations of these disks. Much information can be gleaned from spectral observations of a disk's thermal emission. The mid-IR spectrum of β Pictoris was discovered to contain silicate emission features near 10 μm very similar to those seen in the coma of comet Halley (Telesco & Knacke 1991). Silicate features (which are located at 9.7 and 18 μm) have since been identified in the spectra of a broad sample of debris disks (e.g., Fajardo-Acosta et al. 1993; Sylvester et al. 1996; Sitko et al. 1999). Careful modeling is needed for a successful interpretation of the relative abundance of silicates in these systems, since feature strengths depend on the temperature and size distribution of the disk particles; e.g., the silicate emission features are only observed if most of the disk particles are smaller than 10 μm (Greenberg & Hage 1990). The spectra of some debris disks also show unidentified IR emission bands which indicate oxygen and carbon rich dust species (Sylvester et al. 1996) and could be attributed to thermally spiking small grains (Sylvester et al. 1997). These grains could be PAHs which are so small that on absorption of a single UV photon, their temperature rises to between 1000 and 1500 K. Thermally spiking grains also have emission features at $\sim$ 10 μm which means that interpretation of a 10 μm excess in terms of silicate emission should be treated cautiously.

In fact, any inferences from spectral observations are only as strong as the model upon which they are based; e.g., the model must include the spatial distribution of the emitting dust which is

in general not known. Further, the spatial distribution of the particles emitting at one wavelength may not be the same as those at a different wavelength (§3.4). There may also be two populations of particles that have different compositions; these may, or may not, be spatially related (e.g., the PAHs may originate in the mantles of the particles responsible for the silicate emission, or they may be an unrelated population). However, the observations tend to concur with the theoretical arguments that debris disk particles have their origin in interstellar dust particles. This lead to the formation of a comet dust model for the β Pictoris disk (Li & Greenberg 1998).

5.5 Dust Models

When creating a model for debris disk particles, one must remember that the methods for calculating their optical properties are limited, since there are only rigorous solutions for light scattering from particles that are either spheres (using Mie theory) or infinite cylinders (Bohren & Huffman 1983). Solutions for more complicated configurations do exist (e.g., Xu & Gustafson 1999), however at present these are prohibitively computer intensive for our purposes. Solutions can also be found using laboratory experiments. I have chosen to use Mie theory throughout this dissertation, not because I believe debris disk particles to be compact spheres, but for its robustness (the codes are well-established in the astronomical community) and its ability to provide a real-time solution.

Given this constraint, the simplest model for the dust particles is that they are spherical and composed of a single material. The most obvious choice for this material is silicates. Based on a combination of laboratory measurements and infrared emissivities inferred from astronomical observations of circumstellar and interstellar grains, Draine & Lee (1984) obtained the optical constants of a material they term "astronomical silicate". This model has since been updated (Laor & Draine 1993), and the updated optical constants for astronomical silicate are plotted in Fig. 5.2. Since astronomical silicate is not a physical material, its density is undefined. Here it is taken as 2.5 g/cm^3, a density representative of IDPs (Gustafson 1994). Another set of optical constants for silicates comes from the core material of the interstellar dust model of Li & Greenberg (1997), which is amorphous olivine, $MgFeSiO_4$, with a density of 3.5 g/cm^3. The optical constants of this core material were found from laboratory measurements of amorphous and crystalline olivine (and in part from Draine & Lee 1984), and are plotted next to those of astronomical silicates in Fig. 5.2 for comparison. Another choice for the dust material is the organic refractory mantle of the interstellar grain model (Li & Greenberg 1997), which has a density of 1.8 g/cm^3. The optical constants for this material were found using a combination of measurements of ices that have been subject to UV photoprocessing in space, measurements of the Murchison meteorite, and theoretical reasoning (Li & Greenberg 1997), and are plotted in Fig. 5.3. Other potential materials for dust particles are water ice, graphite, or PAHs, but these are not discussed here.

The absorption coefficients, Q_{abs}, for Mie spheres of different sizes composed of both astronomical silicate and organic refractory material are plotted in Figs. 5.2 and 5.3. Since the imaginary part of the optical constants, $m"$, is related to how energy is dissipated in the particle, Q_{abs} is closely related to $m"$. There is more information about how these constants lead to the temperature and brightness dependences in a debris disk in Chapter 7.

A more complicated model of the dust particles could still be made within the confines of Mie theory. Using the Maxwell-Garnett effective medium theory (Bohren & Huffman 1983), we could model the particles to be composed of a silicate core and an organic refractory mantle (Hage & Greenberg 1990; Greenberg & Hage 1990). The dielectric constant of the composite grain, $\epsilon_{cm} = m^2$, would be given by:

$$\epsilon_{cm} = \epsilon_m \left[\frac{\epsilon_c + 2\epsilon_m + 2q^3(\epsilon_c - \epsilon_m)}{\epsilon_c + 2\epsilon_m - q^3(\epsilon_c - \epsilon_m)} \right], \tag{5.2}$$

where ϵ_c and ϵ_m are the dielectric constants of the core and mantle materials, respectively, and q is the fractional radius of the core to the mantle. The same effective medium theory could also be used to model a fluffy aggregate of core-mantle particles with a packing factor (one minus the porosity),

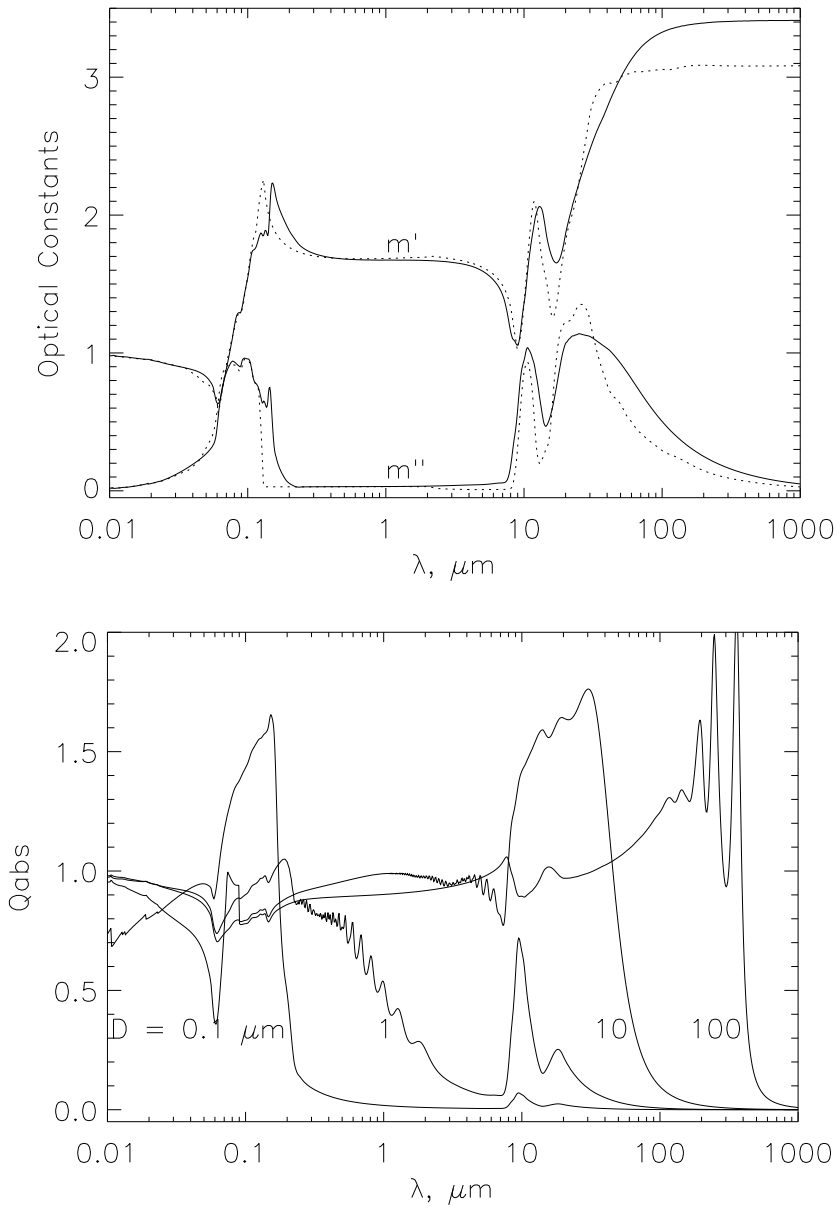

Figure 5.2: The optical properties of particles composed of astronomical silicate. The optical constants, $m(\lambda) = m' + im''$, are shown in the top plot. The solid line corresponds to the astronomical silicates of Draine & Lee (1984), and the dotted line corresponds to the silicates of Li & Greenberg (1997). The absorption coefficients for solid spherical astronomical silicate (Draine & Lee 1984) particles with diameters, 0.1, 1, 10, and 100 μm, calulated using Mie theory, are shown in the bottom plot.

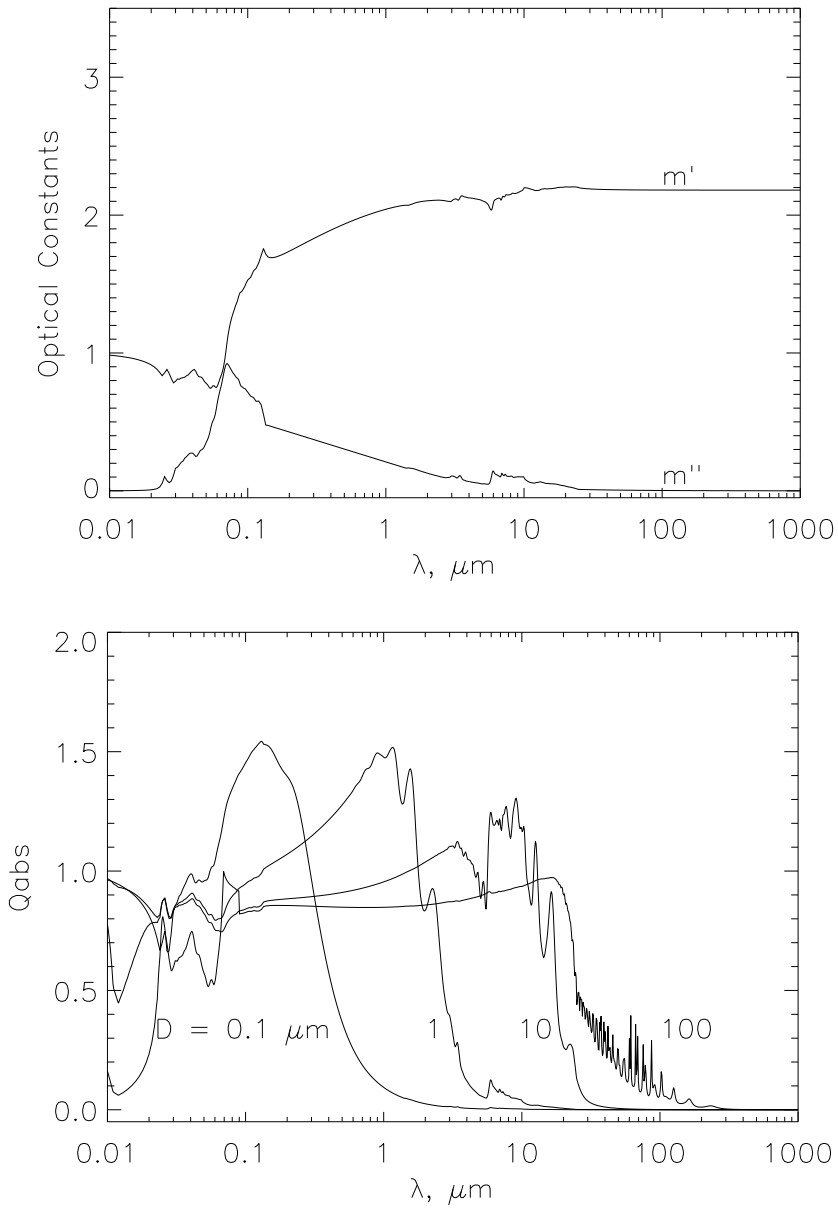

Figure 5.3: The optical properties of particles composed of organic refractory (Li & Greenberg 1997). The optical constants, $m(\lambda) = m^{'} + im^{"}$, are shown in the top plot. The absorption coefficients for solid spherical particles with diameters, 0.1, 1, 10, and 100 μm, calulated using Mie theory, are shown in the bottom plot.

f. The resulting dielectric constant would be (Hage & Greenberg 1990; Greenberg & Hage 1990):

$$\epsilon = \frac{\epsilon_{cm} + 2 - 2f(1 - \epsilon_{cm})}{\epsilon_{cm} + 2 + f(1 - \epsilon_{cm})}, \tag{5.3}$$

where we have assumed that the space between the core mantle particles is filled with a vacuum, however, this space could also be filled with ice.

This is the essence of the cometary grain model for the β Pictoris disk (Li & Greenberg 1998), which has also been used to study the HR4796 disk (Augereau et al. 1999). Given that debris disk particles are likely to originate from comet-like bodies, this is the best available model. There are, however, many parameters in this model, so a lot of information about the disk's spectral energy distribution is needed in order to constrain them. Some of the model parameters could be estimated by constraining the abundance of the different elements in the grain model to match that of the abundances in the star. Since this model is not used in this dissertation, it will not be discussed in any further detail.

CHAPTER 6
HR 4796 LITERATURE REVIEW

The remainder of the dissertation shows the application of the theory of the previous chapters to the modeling of a real disk observation. The disk that is studied is that around the A0V star HR 4796A, and the observations that are modeled are those of Telesco et al. (2000, herafter T2000). Most of the modeling described here has been presented in Wyatt et al. (1999, hereafter W99). Before embarking on the modeling, this chapter describes the information available about the HR 4796 system from the literature.

6.1 The stars HR 4796A and HR 4796B

The HR 4796 system is a binary system consisting of the A0V star, HR 4796A (Gerbaldi et al. 1999), and the T Tauri-like pre-main sequence M2.5 dwarf star HR 4796B (Stauffer et al. 1995). There is no spectroscopic evidence to suggest that these stars are also close binaries (Jura et al. 1995). The position of HR 4796B relative to HR 4796A is at a projected separation of 7.7 arcseconds and at position angle (measured counterclockwise from north) of 226° (Jura et al. 1993). Since this separation has not changed over the last 61 years (Jura et al. 1993), there is strong evidence that the two stars are physically associated. This association is supported by the similarities of their proper motions, radial velocities, and ages (Jura et al. 1993). There are two stars that are located close to HR 4796A on the sky: HR 4796C is located at 40 arcseconds separation and HR 4796D is at 4.7 arcseconds separation. Both of these are background stars (Jura et al. 1993; Mouillet et al. 1997a; Jura et al. 1998).

The distance to HR 4796A was measured by Hipparcos to be 67.1 ± 3.5 pc. The physical parameters of HR 4796A were estimated to be (Gerbaldi et al. 1999): $T_{eff} = 9774 \pm 100$ K, $L_\star/L_\odot = 23.4 \pm 2.3$, $log(g_{ev}) = 4.33 \pm 0.03$, $M_\star/M_\odot = 2.18 \pm 0.1$, $R_\star/R_\odot = 1.68$, $t \approx 10^7$ years, and $v \sin i = 150$ km/s (i.e., rapid rotation). Like other IR excess stars, it is under luminous for its color, which is indicative of its youth (Jura et al. 1998). In the modeling of W99 that is described here, the parameters were assumed to be those of a typical A0V star (Jura et al. 1998): $T_{eff} = 9500$ K, $L_\star/L_\odot = 21$, $M_\star/M_\odot = 2.5$. This discrepancy would not affect the results in any significant manner. A typical A0 star has a main sequence lifetime of $\sim 10^9$ years, and has low stellar winds and magnetic fields (Artymowicz 1997). The spectrum of HR 4796A is characterized by weak metal lines (Gerbaldi et al. 1999), however, a detailed model for the stellar atmosphere is needed to estimate the stellar abundances. High resolution spectroscopy of other Vega-excess stars showed that their photospheric abundances are only slightly under the solar values (Dunkin et al. 1997). Such an underabundance would be expected if some of the heavier elements in the gaseous stellar environment had been accreted onto dust grains before this gas was accreted onto the star. This has been proposed as an explanation for the origin of the metal poor A-type λ Bootis stars (Venn & Lambert 1990).

The parameters for HR 4796B are (Jayawardhana et al. 1998): $T_{eff} = 3620 \pm 60$ K, $L_\star/L_\odot = 0.11 \pm 0.02$, and $M_\star/M_\odot = 0.38 \pm 0.05$. The spectrum of HR 4796B shows an extraordinarily strong lithium 6708 Å absorption line (Stauffer et al. 1995). From the strength of this line and from pre-main sequence isochrone fitting, the age of HR 4796B was estimated to be 10 Myr (Stauffer et al. 1995; Jura et al. 1998). This fits in with observations of the rotational velocity and chromospheric activity of the star. Further, the star is a source of X-rays with $L_X/L_{bol} \approx 3 \times 10^{-4}$, which is typical for a 10^7 year old pre-main sequence star (Jura et al. 1998). Assuming the two stars to be coeval, we thus have an accurate age estimate for the system. The current projected separation between

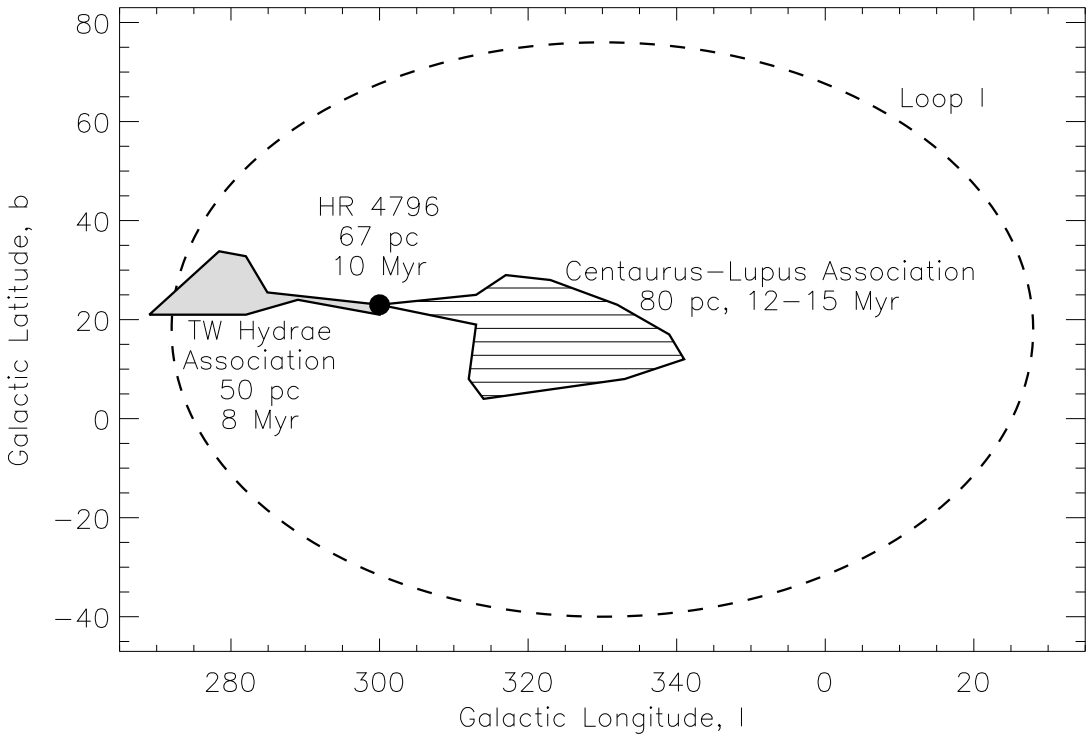

Figure 6.1: The positions on the sky of HR 4796, the Centaurus-Lupus association (de Geus et al. 1989; Jura et al. 1995), the TW Hydrae association (Webb et al. 1999; Jayawardhana et al. 1999), and the Galactic giant radio loop, Loop I (Berkhuijsen et al. 1971; Egger & Aschenbach 1995).

HR 4796A and HR 4796B corresponds to a projected distance of ~ 517 AU, which gives an orbital period of > 7000 years (eq. [3.2]). The relative positions of the two stars was also observed 61 years ago, however the observational errors mean that it is not possible to derive the binary orbit from the change in their relative positions (Jura et al. 1993). Based on samples of other binary orbits, the long period of the binary orbit implies that it could be highly eccentric ($e > 0.5$; Black 1997).

The HR 4796 system is located at an R.A. and Dec. of 12h 36m, $-40°$, or in Galactic coordinates, at $l = 300°$, $b = 23°$ (see Fig. 6.1). It was first speculated that HR 4796 might be a very young and close member of the Centaurus-Lupus region (Jura et al. 1993; Jura et al. 1995), where stars are at 80 ± 20 pc from the Sun, and have an age of 12-15 Myr (de Geus et al. 1989), since its proper motion and radial velocity are similar to those of the rest of the group. HR 4796 lies at the edge of this region, which is centered $\sim 25°$ away close to $l = 325°$, $b = 18°$. More recently, HR 4796 has been associated with the TW Hydrae association (TWA) (Webb et al. 1999; Jayawardhana et al. 1999). At ~ 50 pc and an age of ~ 8 Myr (Webb et al. 1999), the TWA is the closest known region of recent star formation. If HR 4796 is indeed a member of the TWA, then it is the most distant member of the group. Also, HR 4796 lies on the edge of the group, the center of which is $\sim 18°$ away, close to TW Hydrae itself, which is at $l = 279°$, $b = 23°$. The two groups Centaurus-Lupus and the TWA do not overlap, rather, HR 4796 lies in between them (see Fig. 6.1). All members of the TWA have the same signatures of youth: high X ray fluxes, large lithium abundances, and strong chromospheric activity (as does HR 4796B); the age of the TWA is ~ 8 Myr (Webb et al. 1999) and most members are T Tauri stars. They also have similar proper motions and radial velocities. There has been much speculation about the origin of the TWA, because there appears to be very little nearby molecular gas, and most young stars are found in regions of molecular clouds (Leisawitz et al. 1989); the natal clouds of the TWA stars appear to

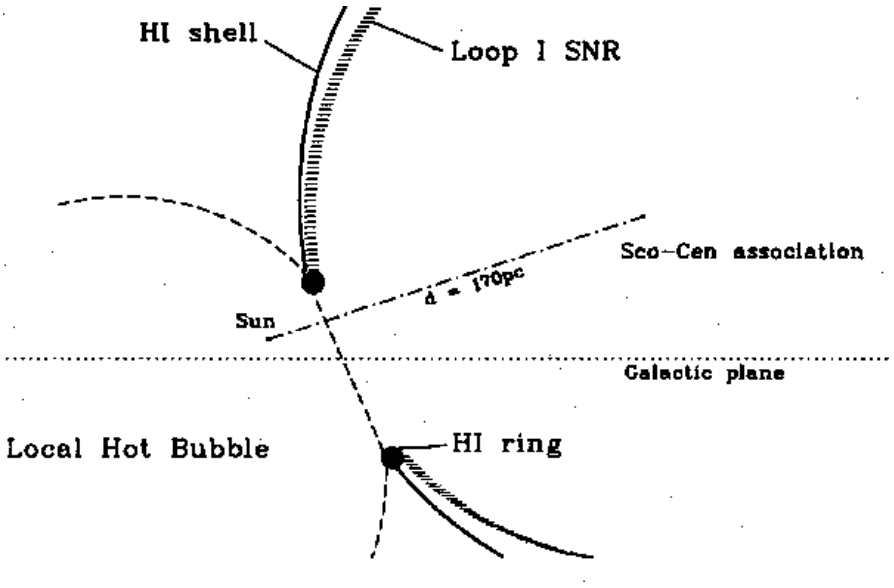

Figure 6.2: The possible spatial arrangement of the Sun, the Local Hot Bubble, the Scorpio-Centaurus association, the HI shell, and Loop I (Egger & Aschenbach 1995). This is a vertical cut normal to the Galactic plane through the interaction area of Loop I and the LHB.

have been dispersed or destroyed. Both the nearest dark cloud and the nearest CO emission are $> 15°$ from HR 4796. Based on its motion through space, HD 98800, which is a quadruple system in the TWA, was shown to be within the Scorpio-Centaurus complex at the time of its birth ~ 10 Myr ago if its velocity relative to this complex was ~ 15 km/s (Soderblom et al. 1998).

Since HR 4796 is nearby, we should know something about the interstellar medium within which it resides (for a review of the local interstellar medium, see Ferlet 1999). Loop I is a Galactic giant radio loop of $\sim 58°$ radius centered at $l = 330°$, $b = 18°$ (Berkhuijsen et al. 1971; see Fig. 6.1), which is caused by the interaction of a shock wave with the interstellar medium. It can be modeled as a superbubble of radius ~ 160 pc produced by collective stellar winds and several consecutive SN events in the Scorpio-Centaurus OB association which is at a distance of ~ 170 pc (Egger & Aschenbach 1995; see Fig. 6.2). The terminal shock of the bubble is still expanding outwards at a velocity of ~ 20 km/s; the most recent SNe was $\sim 2 \times 10^5$ years ago (Egger & Aschenbach 1995). It is interacting with the Local Hot Bubble (LHB), the superbubble within which the Sun is embedded (although not at the center), which has a radius of ~ 100 pc (Ferlet 1999). At the shock wall, a ring of neutral matter is expected to form that is denser by a factor of 20-30 than the ambient medium (Yoshioka & Ikeuchi 1990). The HI column density in this direction does indeed increase by this factor at about 70 pc, however, the exact shape and distance to the ring is not uniform, since other estimates put the neutral gas wall at $\sim 40 \pm 25$ pc (Egger & Aschenbach 1995).

Thus, it appears that both HR 4796 and the TWA sit either at the edge of or within the shock front neutral gas wall. Could the TWA be associated with the terminal shock, which when it passed a molecular cloud some $\sim 10^7$ years ago, triggered both star formation and the dispersal of this cloud? This would explain the proper motion of HD 98800, the natal cloud of which would have attained a proper motion relative to the shock center. If this were true, it could explain the origin of the proper motion of the whole TWA. The shock could also have been responsible for star formation in the Centaurus-Lupus association, since at a distance of 80 pc, it is closer to the shock center, thus the shock would have passed it longer ago than the TWA, explaining the older age of these stars. An estimate of the speed of the shock front in this scenario depends on the geometry of the two associations with respect to the plane of the shock front, which may be significantly deformed due to

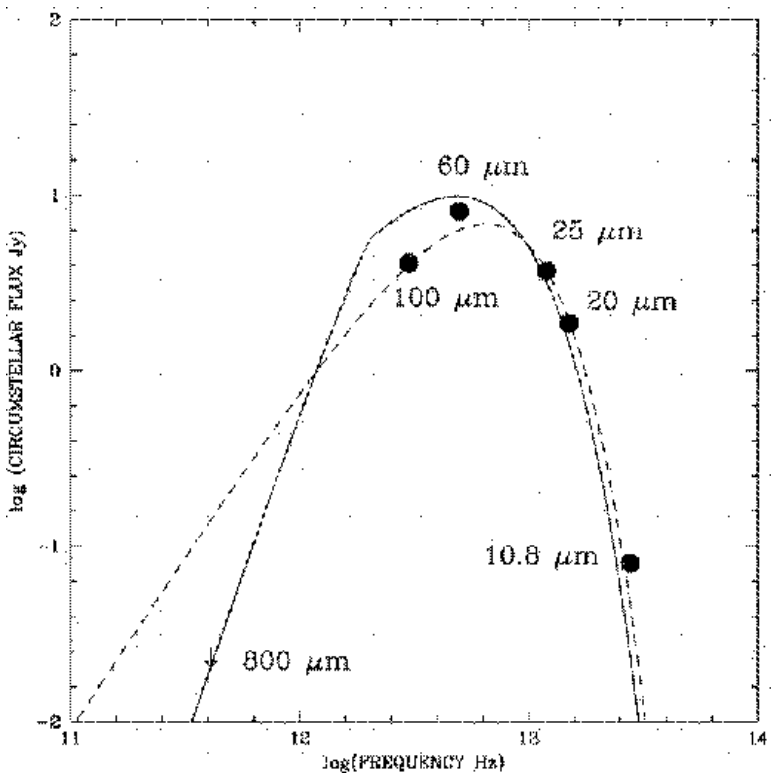

Figure 6.3: The excess dust emission from the HR 4796 disk above that of the photosphere of HR 4796A (Jura et al. 1998). The solid circles are the IRAS measured excesses (Jura 1991), and the limit to the sub-mm excess comes from observations described in Jura et al. (1995). The dashed line indicates emission from a black body at a temperature of 110 K. The solid line is the emission from a model of a disk composed of icy grains (Jura et al. 1998).

its interaction with the LHB (Egger & Aschenbach 1995). Without studying this geometry further, I note that a distance of 30 pc traveled in 5.5 Myr corresponds to a velocity of ~ 5 km/s, which is comparable to the velocity of the expanding shock front. So far, the evidence is purely speculative. More detailed analysis of the spatial geometry of the shock front with respect to the associations from radio and X-Ray observations is warranted. There may be other observational consequences of this scenario which either support it or rule it out.

6.2 The Pre-discovery Disk

HR 4796A was one of the stars observed by IRAS to have an IR flux above that expected from the photospheric emission from the star that was seen to be indicative of debris disks. Until the disk was resolved, interpretation of the IR excess had to be based on the shape of the spectral energy distribution (Jura 1991; Fig. 6.3). The mean optical depth of the dust debris is very high at $\tau = L_{dust}/L_\star = 5 \times 10^{-3}$ (Jura 1991). The shape of the SED implied that the dust in the disk is at a temperature of 110 K and therefore has an inner hole ≈ 40 AU in radius from the star (Jura et al. 1993). Limits from the non-detection of reflection nebulosity put an outer limit of 130 AU to the dust location (Mouillet et al. 1997a; Jura et al. 1998).

Thus, the disk emission arises from analogue Kuiper belt regions. Since the age of the HR 4796 system (Stauffer et al. 1995) places it at a stage in its evolution when the formation of any planets is expected to be almost complete (e.g., Lissauer 1993), many authors speculated that the central cavity could be indicative of planetary formation in this inner region. It was thought that a

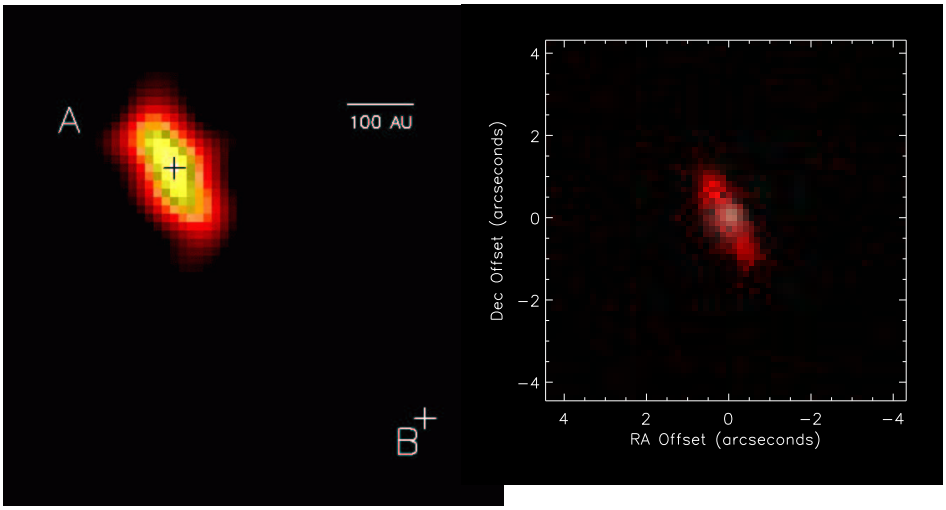

(a) **(b)**

Figure 6.4: Discovery images of the mid-IR emission from the HR 4796 disk. **(a)** False color image of the HR 4796 disk in the IHW18 (18.2 μm) waveband (Jayawardhana et al. 1998). The positions of star A and star B are marked with crosses. **(b)** Composite two-color image of the emission from HR 4796 at $\lambda = 12.5$ (light) and 20.8 μm (dark) (Koerner et al. 1998).

sweeper companion orbiting HR 4796A at a distance of half the hole radius (Artymowicz & Lubow 1994) could be the cause of the inner hole (Jura et al. 1995; Jura et al. 1998). Speckle imaging at 2 μm showed that any companion between 11 and 120 AU from HR 4796A must be less than 0.2 $M_{\odot}$ (Jura et al. 1995; Jura et al. 1998). Another origin that was proposed for the inner hole was that the dust grains are icy. Icy grains would sublimate in the inner hole region due to the high temperatures attained by the dust there (Jura et al. 1998). A model that gave the spatial distribution of icy grains in the disk based on their sublimation times was shown to provide a good fit to the observed excess (Jura et al. 1998; see Fig. 6.3).

A lower limit to the disk's mass was obtained from its optical depth, since this arises from the disk's small emitting particles that contain the disk's surface area, but not its mass. An upper limit to its mass was obtained from the sub-mm flux, since this arises from the larger particles in the disk ($\sim$ 1 mm) which are more indicative of the disk mass. These gave the constraint that $0.1 M_{\oplus} < M_{disk} < 1.0 M_{\oplus}$ (Jura et al. 1995; Jura et al. 1998), which is $O(10^{-3})$ less than that expected to have been around the star in its pre-main sequence stage (Jura et al. 1993). Study of the nature of the HR 4796 disk was understood to be particularly important, since it could yield clues to the scenario of disk formation in binary systems (Clarke & Pringle 1991).

6.3 Disk Discovery Images

With the new generation of astronomical instrumentation making it possible to image the thermal emission from the debris disks, observers had to make a choice of which objects to observe, and HR 4796 was high on the list. Two teams reported the simultaneous discovery of the spatially resolved disk (Jayawardhana et al. 1998; Koerner et al. 1998). Their images, shown in Fig. 6.4, show the disk's 18 and 21 μm emission to be concentrated in two lobes, one on either side of the star. The emission is extended along a position angle of $210 \pm 10°$, which is similar to the direction of HR 4796B. These observations indicate that the disk is being observed nearly edge-on, and that its inner region is almost completely devoid of dust. The outer edge of the disk at 18 μm was observed to be at $\sim$ 110 AU (Jayawardhana et al. 1998). Comparison of parametric models for the disk morphology with these observations gave the radial location of the inner hole at 55 ± 15 AU from the star, and an inclination of the disk plane of $\sim 18°$ to the line of sight (Koerner et al. 1998). In contrast to the 21 μm emission, the 12.5 μm emission was observed to be faint and concentrated at

the stellar position, and was concluded to arise from a tenuous population of hot grains close to the star (Koerner et al. 1998).

6.4 The Post-discovery Disk

The discovery images (Jayawardhana et al. 1998; Koerner et al. 1998) attracted a lot of attention and there has consequently been a significant amount of work done on this disk. One of the teams involved in the discovery made follow-up observations of the disk in the N (10.8 μm) and IHW18 (18.2 μm) wavebands from Keck (T2000). These observations, which are shown in Fig. 6.5, are the best (in terms of sensitivity and resolution) mid-IR images of the disk to date. These not only confirmed the 18 μm double-lobed structure in more detail than before, but also showed a further interesting feature: the disk's lobes appear to be of unequal brightness, although this observed asymmetry is of low statistical significance ($\sim 1.8\sigma$). Their observation suggests that the NE lobe (on the upper left of the image in Fig. 6.5a) is $\sim 5\%$ brighter than the SW lobe. The same asymmetry is suggested in the 21 μm images of Koerner et al. (1998). The modeling of these images is described in W99, and is also described in the next two chapters.

The premise of the W99 modeling was that we know that if there is at least one massive perturber in the HR 4796 system that is on an eccentric orbit, then the system's secular perturbations would have caused the disk's center of symmetry to be offset from the star (Dermott et al. 1998; §4.1). This offset would mean that the material in one of the disk's observed lobes is closer to the star than that in the other lobe; consequently this lobe would be hotter and brighter. The aim of the modeling was to ascertain how large the perturbations would have to be to cause the observed 5% asymmetry, and to discuss whether perturbations of this magnitude are physically realistic, or even to be expected, in this system. As well as providing an explanation for the asymmetry, the W99 modeling confirmed the large scale disk morphology and orientation. Combining the IHW18 and N band observations, the modeling also showed that the particles in the outer disk are likely to be small 2-3 μm particles that are observed in the process of being blown out of the system.

The disk was also imaged in the near-IR, 1.1 and 1.6 μm, by NICMOS (Schneider et al. 1999). These images, one of which is reproduced in Fig. 6.6, show the disk in scattered light. These showed that the morphology of the disk at 1.1 and 18.2 μm and are almost identical (T2000). They also appear to show the same lobe asymmetry as the T2000 images. Asymmetries in images of a disk's scattered light can, however, arise from purely geometrical causes (Kalas & Jewitt 1995). From these observations, the NICMOS team inferred that the disk must be confined to a 17 AU wide ring, although this is not based on any detailed modeling of the disk morphology. Since the ring appears somewhat red in reflection, they also inferred that the mean particle sizes are in excess of several μm.

A model of the HR 4796 disk was produced that was based on a compilation of all previous observations of its spectral energy distribution, and using the NICMOS images for information about the spatial distribution of material in the disk (Augereau et al. 1999). The model used a simple parametric distribution of grains, the optical properties of which were modeled in the same way as proposed by Li & Greenberg (1998) for the grains in β Pictoris. It was found that the disk observations could be best fitted by two independent grain populations: a cold annulus peaking at 70 AU from the star with a width of ≈ 14 AU comprised of amorphous interstellar-like grains that have a porosity of 0.6, a small proportion of ices, and which have sizes that range from 10 μm to ~ 1 m, giving a mass of this component of a few $M_\oplus$; and a tenuous warm inner component at 9-10 AU from the star made of crystalline comet-like grains with a porosity of 0.97. The inner population of this model contributes almost all of the 10 μm flux, but little at longer wavelengths. This is a contentious issue, since the model did not have access to the results of T2000 that indicate that much of the 10 μm emission does indeed come from the outer disk. It would be interesting to see what the results of this modeling would have been had it included the observations of T2000.

Kenyon et al. (1999) modeled the planetesimal accretion in the HR 4796 disk, since it was not expected that planet-sized objects would form on short timescales at large distances from the

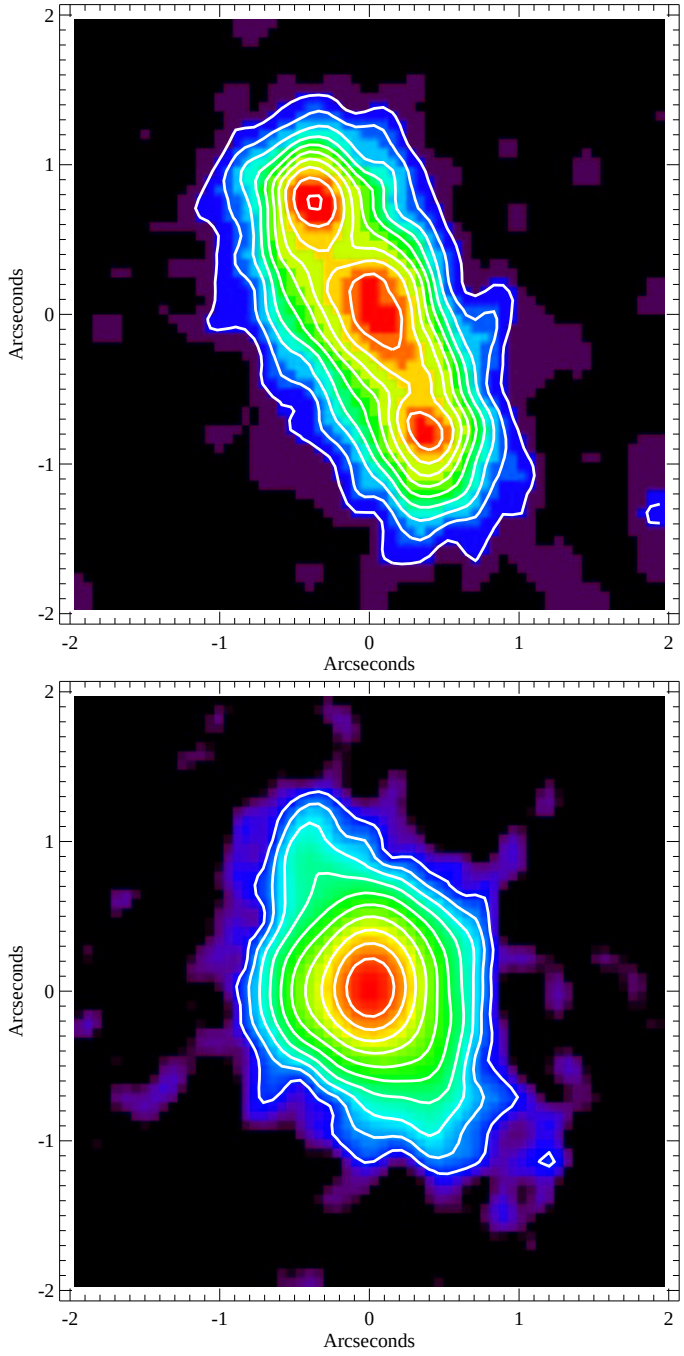

Figure 6.5: Images of HR 4796A made with OSCIR at Keck (Telesco et al. 2000). North is up, east is to the left, and HR 4796A is located at the center of the images. *Top*: IHW18 (18.2 μm) waveband image with contours (mJy/arcsec^2) spaced linearly at 58, 93, 128, 163, 198, 234, 269, 304, 339, 374. *Bottom*: N (10.8 μm) waveband image with contours (mJy/arcsec^2) spaced logarithmically at 6.4, 9.9, 15, 23, 36, 55, 85, 132, 203, 312.

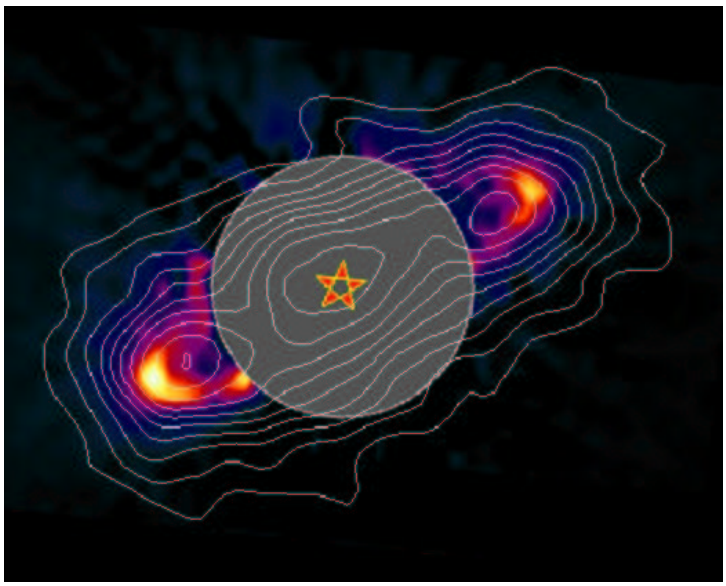

Figure 6.6: NICMOS 1.1 μm image of the scattered light from the HR 4796A circumstellar ring (Schneider et al. 1999). East is approximately down. The unusable area circumscribing the coronographic hole is indicated by the gray circle. For comparison, the 18.2 μm contours from the observation of T2000 (shown in Fig. 6.5) have been overlaid onto the scattered light image.

star. They showed that a dusty ring with a width of 7-15 AU and a height of 0.3-0.6 AU at 70 AU from HR 4796A would indeed form in $\sim$ 10 Myr as a natural outcome of the planetary formation process if the initial mass of the protoplanetary disk was 10-20 times the minimum mass solar nebula. The modeling process they used was the same as that used to estimate that the formation of Pluto would have taken $10 - 40$ Myr at 35 AU from the Sun (Kenyon & Luu 1999). They treat the planetesimals as a statistical ensemble of bodies with a distribution of horizontal and vertical velocities about keplerian orbits. Collisions between the planetesimals is assumed to result in either mergers (with potential cratering debris), catastrophic disruption, or inelastic rebound. Gas drag and mutual gravitational interactions are also included in the model. The planetesimal growth is simulated from when the planetesimals are 80 m in size. Thus, this planetesimal accretion model is based on assumptions about the outcome of the early stages of planet formation (i.e., the origin of the swarm of 80 m planetesimals) which are not as well understood as the latter stages. They find that there is initially a period of slow growth when planetesimals grow from 80 to 1000 m. In this stage collisions damp the velocity dispersion. After this there is runaway growth of the largest bodies in the disk from 1 to 100 km in several Myr. This increases the velocity dispersion, thus ending runaway growth. Finally there is slow growth from 100 to 1000 km.

Liseau (1999) observed HR 4796A in the CO (1-0) and (2-1) lines, but neither continuum or molecular line emission was detected. They concluded that this could either be a consequence of a dirth of gas in the system, possibly lost in the planetary formation process, or of photodissociation of the molecules from the intense stellar UV field. They did not put any quantifiable constraint on the gas in the system. Independent observations put the gas mass at $< 1 - 7 M_{\oplus}$ (Greaves et al. 1999), which means that it would probably not play an important role in the dynamics of the disk.

CHAPTER 7
THE DYNAMIC HR 4796 DISK MODEL

This chapter describes a model of the HR 4796 disk that accounts for the brightness distribution seen in the IHW18 waveband observation of T2000 (Fig. 6.5; also reproduced in Fig. 7.6a). This model is based on the theory of Chapters 2 to 5, and is also presented in W99. While the modeling techniques that are used are new to the study of circumstellar disks, they have already been widely used to study the observed structure of the zodiacal cloud (see, e.g., Dermott et al. 1994; Grogan et al. 1997), and so can be used with a certain degree of confidence. There are three components of the observation that had to be included in the model (§2.5): the disk's structure, $\sigma(r, \theta, \phi)$, defined in §2.2; the combination of the optical properties and the size distribution of the disk's particles given by $P(\lambda, r)$, defined in §2.3; and the disk's orientation.

7.1 Model of Offset Disk Structure, $\sigma(r, \theta, \phi)$

The disk's structure was modeled as that of a secularly perturbed dynamic disk. A combination of the theory of Chapters 3 and 4, and inferences from the observation (Fig. 7.6a), was used to parameterize the distribution of the orbital elements of the disk's large particles (§7.1.1). This was used to create parameterized models of the spatial distribution of these large particles (§7.1.2), that could then be compared with the observed spatial distribution. Since the observed spatial distribution is that of the emitting particles, the underlying assumption is that these emitting particles either are the disk's large particles, or that their spatial distribution is the same as that of the disk's large particles (whether they are large or not). The implications of this assumption are discussed in the interpretation of the model (Chapter 8).

7.1.1 Distribution of Orbital Elements, $\sigma(a, e, I, \Omega, \tilde{\omega})$

The quintessentially secular part of the distribution of the orbital elements of the large particles in a secularly perturbed disk is the distributions of their complex eccentricities, $n(z)$, and complex inclinations, $n(y)$. For a particle with an orbit of a given semimajor axis, a, its complex eccentricity, z, and complex inclination, y, are the addition of forced elements, $z_f(a)$ and $y_f(a)$, to proper elements that have $\tilde{\omega}_p$ and Ω_p chosen at random, while e_p and I_p are chosen from the distributions $n(e_p)$ and $n(I_p)$.

Since there is insufficient information available to determine the variation of the forced and proper elements with semimajor axis in this disk, they were assumed to be constant across the disk. The forced elements were left as model variables: the forced eccentricity, e_f, defines the magnitude of the offset asymmetry in the disk model; the forced pericenter orientation, $\tilde{\omega}_f$, defines the orientation of this asymmetry; and the forced inclination, y_f, defines the plane of symmetry of the disk model. When creating a disk model, both $\tilde{\omega}_f$ and y_f were set to zero; these were incorporated later into the description of the disk's orientation to the line of sight of the observation (see §7.3). The distributions of the proper eccentricities, $n(e_p)$, and proper inclinations, $n(I_p)$, of particles in the disk model were taken to be like those of the main-belt asteroids with absolute magnitudes $H < 11$ (Bowell 1996; see Fig. 7.1). These large asteroids constitute a bias-free set (Bowell 1996) and have mean proper eccentricities and proper inclinations of $\langle e_p \rangle = 0.130$ and $\langle I_p \rangle = 10.2°$. Not enough Kuiper belt objects have been discovered yet to infer a bias-free distribution for their orbital elements.

The distribution of the semimajor axes, $n(a)$, of particles in the disk defines its radial distribution. There is no way of guessing this distribution from theoretical considerations, since it

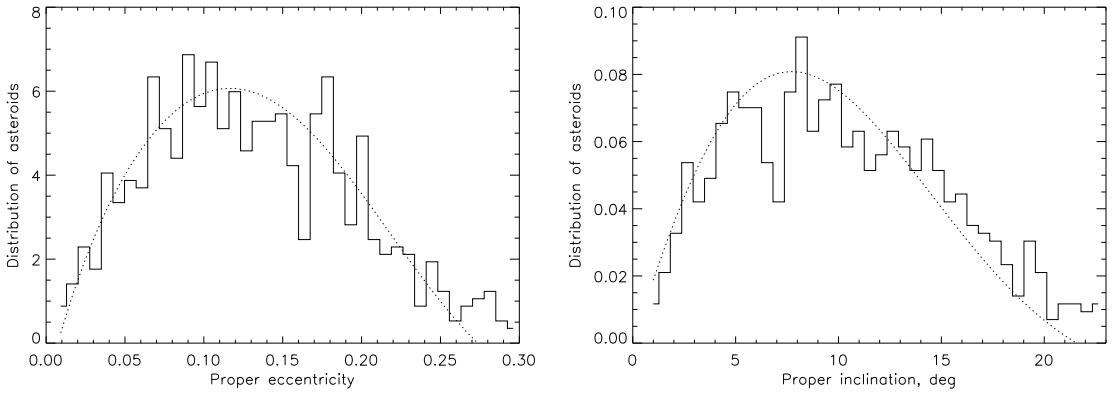

Figure 7.1: Distribution of the proper eccentricities and inclinations of the mainbelt asteroids. The histogram indicates the observed distribution and the dotted line is the parameterized fit to this distribution that was used in the model.

depends on the outcome of the system's planetary formation process, which varies from system to system (compare the distribution of the solar system's planets, and its disk material, with those found in exosolar systems, e.g., Backman & Paresce 1993; Marcy & Butler 1998). Thus, it had to be deduced purely observationally. Fig. 7.6a shows that the disk has an inner edge, inside of which there is a negligible amount of dust; this was modeled as a sharp cut-off in the distribution of semimajor axes at a_{min}, a model variable. The observation also shows that the disk has an outer edge at ~ 130 AU; this was modeled as a sharp cut-off in the distribution of semimajor axes at $a_{max} = 130$ AU (this is a non-critical parameter, since particles near the outer edge of the disk contribute little to the observation, see §7.2.3). The distribution between a_{min} and 130 AU was taken as $n(a) \propto a^{\gamma}$, where $n(a)da$ is the number of particles on orbits with semimajor axes in the range $a \pm da/2$, and γ is a model variable. To get an idea of the radial distribution resulting from this semimajor axis distribution, consider that if the particles had zero eccentricity, this distribution would result in a volume density (number of particles per unit volume) distribution that is $\propto r^{\gamma-2}$ (since the number of particles in a spherical shell of width dr, the volume of which is $\propto r^2 dr$, would contain a number of particles that is $\propto r^{\gamma} dr$).

7.1.2 Conversion to Spatial Distribution, $\sigma(r, \theta, \phi)$

Disk models were created from the orbital element distribution of §7.1.1 using the "SIMUL" program; SIMUL was developed by the solar system dynamics group at the University of Florida (Dermott et al. 1992). A disk model is a large three-dimensional array, $\sigma(r, \theta, \phi)$, that describes the spatial distribution of the cross-sectional area of material in the disk model per unit volume binned in: r, the radial distance from the star; θ, the longitude relative to an arbitrary direction (set here as the forced pericenter direction, $\tilde{\omega}_f$); and ϕ, the latitude relative to an arbitrary plane (set here as the forced inclination, y_f, or symmetry, plane). SIMUL creates a disk model by taking the total cross-sectional area of material in the disk (specified by the model variable σ_{tot}), and dividing it equally among a large number of orbits (5 million in this case), the elements of each of which are chosen randomly from the specified distribution (§7.1.1). The disk model is populated by considering the contribution of each orbit to the cross-sectional area density in each of the cells it crosses.

The spatial distribution of material in one such model of the HR 4796 disk can be described by the three variables a_{min}, γ, and e_f; σ_{tot} simply scales the amount of material in the model, and y_f and $\tilde{\omega}_f$ describe the reference plane and the reference direction of the model relative to the line of sight of the observation. Fig. 7.2 is a plot of the surface density of material in a disk model with $a_{min} = 62$ AU, $e_f = 0.02$, and $\gamma = -2$ (this is the final model of §7.4). This illustrates how the specified distribution of orbital elements affects the spatial distribution of material in the disk

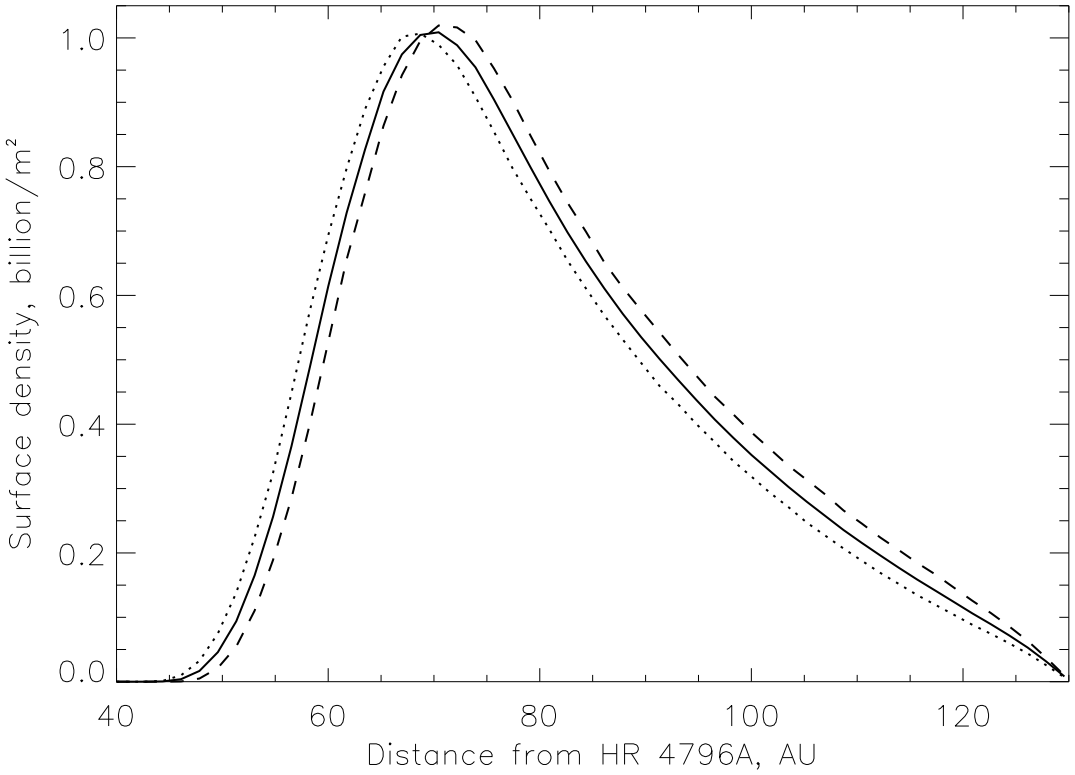

Figure 7.2: The surface number density of the 2.5 μm dust grains in the HR 4796 disk derived from the 18.2 μm brightness distribution (T2000). The solid curve is the azimuthal average of the surface number density, and the dotted and dashed lines indicate the density through the disk towards and away from the forced pericenter direction of the model, respectively. The offset is a result of the forced eccentricity imposed on the disk model; the inner edge of each side of the disk is offset by $\sim a_{min} e_f \approx 1$ AU. The disk's surface density peaks at $\sim 1.02 \times 10^9$ m^{-2} at ~ 70 AU. Interior to this, the surface density falls to zero by 45 AU; the sloping cut-off is due to the eccentricities of the disk model particles' orbits. Exterior to 70 AU, the surface density falls off $\propto r^{-3}$; this is due to the distribution of the disk model particles' semimajor axes, $n(a) \propto a^{-2}$.

model: the sharp cut-off in semimajor axes at a_{min} determines the radial location of the inner hole, which has a sloping cut-off in r due to the particles' eccentricities; as predicted in §4.1.3, particles at the inner edge of the disk in the forced pericenter direction are closer to the star than those in the forced apocenter direction by $\sim 2a_{min}e_f$; the distribution of semimajor axes has produced a surface density distribution that is $\propto r^{\gamma-1}$, but only exterior to 70 AU.

7.2 Model of $P(\lambda, r)$

7.2.1 Optical Properties of Disk Particles

The optical properties of the disk particles were found assuming them to be made of astronomical silicate (Draine & Lee 1984; Laor & Draine 1993), since this is a common component of interplanetary dust found in both the zodiacal cloud (Leinert & Grün 1990) and exosolar systems (e.g., Telesco & Knacke 1991; Fajardo-Acosta et al. 1993; Sitko et al. 1999). The presence of silicates in the disk can be tested at a later date using spectroscopy to look for silicate features in the disk emission. Furthermore, the particles were assumed to be solid, spherical, and have a density of $\rho = 2500\text{kg/m}^3$. Their optical properties were calculated using Mie theory, assuming that HR 4796A has a luminosity and temperature of $L_\star = 21L_\odot$, $T_\star = 9500°\text{K}$ (Jura et al. 1998), and using for its spectrum, that of the A0V star Vega. In other words, the model for the optical properties of the disk particles is a very simple one. The consequences of these simplifications are discussed in the next chapter, but since the modeling aims to reproduce an image of the disk in just one waveband, this should not affect the interpretation of the disk's observed spatial structure (§2.5).

The properties of particles of different sizes, and at different distances from HR 4796A, are shown in Fig. 7.3. The temperatures of the particles are plotted in Figs. 7.3a and 7.3b. The form of Fig. 7.3a can be understood by consideration of equation (2.1), and the wavelengths at which the star and a particle, if it was a black body, emit most of their energy: $\lambda_\star \approx 2898/T_\star$ μm, and $\lambda_{bb} \approx 2898/T_{bb} = 10\sqrt{r/a_\oplus}(L_\odot/L_\star)^{0.25}$ μm. As a crude approximation, a particle with diameter D has $Q_{abs} \approx 1$ for $\lambda \ll \pi D$ and $Q_{abs} \to 0$ for $\lambda \gg \pi D$. This is in qualitative agreement with Fig. 5.2. Thus, in terms of their thermal properties, disk particles can be divided into four categories: the largest particles, $D \gg \lambda_{bb}/\pi$, are efficient absorbers and emitters at all relevant wavelengths and so achieve nearly black body temperatures, T_{bb}; particles with $D \ll \lambda_{bb}/\pi$, are inefficient emitters at their black body temperature, and so need temperatures higher than T_{bb} to re-radiate all of the incident energy; the smallest particles, $D \ll \lambda_\star/\pi$, are also inefficient absorbers at the stellar temperature, and so do not need as high temperatures as slightly larger particles to re-radiate the absorbed energy; and particles with $D \approx 20$ μm have temperatures below that of a black body — this is because these particles are super-efficient emitters at their black body temperatures (due to silicate resonances, Q_{abs} can go up as high as 2), and so need lower temperatures to re-radiate the incident energy. The form of Fig. 7.3b can be understood in the same way. The fall-off of a large (e.g., $D = 1000$ μm) particle's temperature with distance from HR 4796A is like that of a black body, i.e., $T \propto 1/\sqrt{r}$. The fall-off for smaller particles, however, is not that steep because these particles emit less efficiently the further they are from the star (due to their lower temperatures, and consequently higher λ_{bb}); e.g., the fall-off for $D = 2.5$ μm particles is $T \propto 1/r^{0.34}$, which is close to the $1/r^{1/3}$ fall-off expected for particles with an emission efficiency that decreases $\propto 1/\lambda^2$ (e.g., Backman & Paresce 1993).

More important observationally is the variation of $Q_{abs}(\lambda, D)B_\nu[\lambda, T(D, r)]$, since this determines the contribution of a particle's thermal emission to the flux density received at the Earth (eqs. [2.3],[2.7] and [2.8]). This is plotted for $\lambda = 18.2$ μm in Figs. 7.3c and 7.3d, and for $\lambda = 10.8$ μm in Figs. 7.3e and 7.3f. The form of Figs. 7.3c and 7.3e can be explained in the same way that Fig. 7.3a was explained: all three figures have similar forms, which is to be expected since the particles' temperature also appears in B_ν; Figs. 7.3c and 7.3e are, however, attenuated for $D \ll \lambda/\pi$, since these particles are inefficient emitters at that wavelength. The fall-off with distance of the different particles shown in Figs. 7.3d and 7.3f is due solely to their different temperature fall-offs

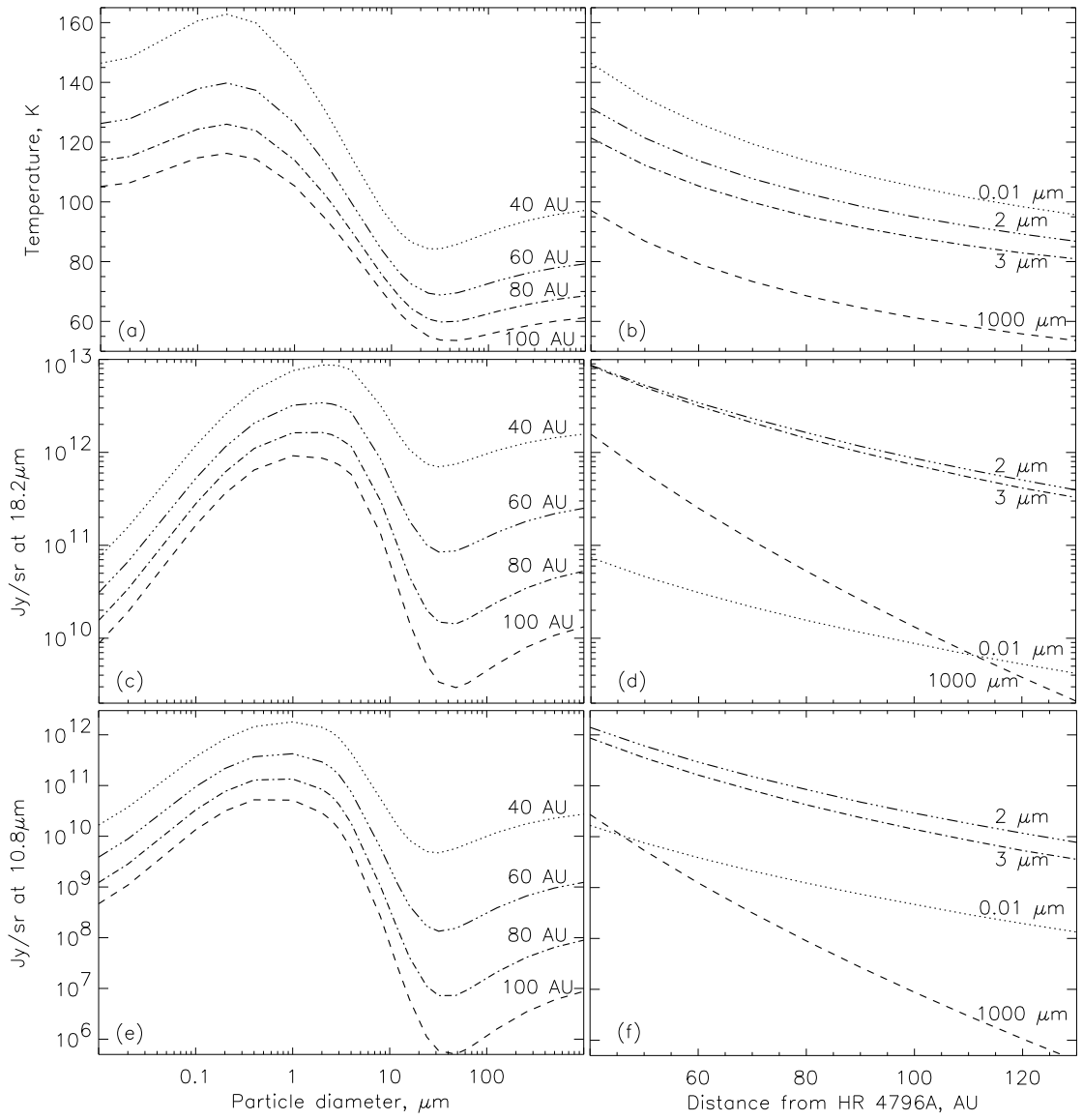

Figure 7.3: The thermal properties of astronomical silicate Mie spheres in the HR 4796 disk, plotted for particles of different sizes at 40, 60, 80, and 100 AU from HR 4797A (**a**), (**c**), and (**e**), and for 0.01, 2, 3, and 1000 μm diameter particles at different distances from HR 4796A (**b**), (**d**), and (**f**). The temperatures that these particles attain is plotted in (**a**) and (**b**). The contribution of a particle's thermal emission to the flux density received at the Earth per solid angle that its cross-sectional area subtends there, $Q_{abs}(D,\lambda)B_\nu[T(D,r),\lambda]$ (eq. [2.3]), is plotted for observations in the IHW18, 18.2 μm, (**c**) and (**d**), and N, 10.8 μm, (**e**) and (**f**) wavebands. The brightnesses of disk models in these two wavebands were calculated by taking $P(\lambda,r)$ from the lines on (**d**) and (**f**) corresponding to particles of diameter D_{typ}.

(Fig. 7.3b); e.g., for $\lambda = 18.2$ μm, the approximate fall-off for $D = 1000$ μm particles is $\propto 1/r^{5.4}$, while that for $D = 2.5$ μm particles is $\propto 1/r^{2.6}$.

7.2.2 Cross-sectional Area Distribution

The definition of $P(\lambda, r)$ (eqs. [2.8] and [2.9]) shows that it is the convolution of $Q_{abs}B_\nu$ (Fig. 7.3c - 7.3f) with the cross-sectional area distribution, $\bar{\sigma}(D, r)$. Since theoretical arguments cannot supply an accurate size distribution (§3.4.2), this model uses the assumption of equation (2.10), which is that $P(\lambda, r)$ is equal to the $Q_{abs}B_\nu$ of particles in the disk with characteristic size, D_{typ}. The model further assumes that this D_{typ} is constant across the disk in the IHW18 waveband; i.e., the brightness of a disk model observation in the IHW18 waveband is calculated using $P(\lambda, r)$ from the line on Fig. 7.3c corresponding to D_{typ}, where D_{typ} is a model variable. A qualitative understanding of D_{typ} comes from Fig. 7.3c: since $Q_{abs}B_\nu$ is fairly flat for particles larger than ~ 8 μm, an IHW18 waveband observation is dominated by those particles with the most cross-sectional area, unless there is a significant amount of particles smaller than 8 μm; Fig. 7.3c also shows that the observation is unlikely to be dominated by particles smaller than $O(0.01$ μm), unless their contribution to the disk's cross-sectional area is much higher than that of larger particles.

In addition to the IHW18 waveband, T2000 observed HR 4796 in the N ($\lambda = 10.2$ μm) waveband. The N band observations also show the double-lobed feature, but the inaccuracy of the subtraction of the image of HR 4796A from the observations means that they cannot be used to constrain the disk's structure. The N band observations can, however, be used to constrain the disk's brightness in this waveband. The brightness of a disk in different wavebands differs only in the factor $P(\lambda, r)$ (eq. [2.7]), and so the N band observation can be used to obtain information about the disk's size distribution. Since Figs. 7.3c and 7.3e have similar forms, the two observations should be dominated by the emission of similarly sized particles; i.e., they should have the same D_{typ}, and show similar structures. The same characteristic particle size, D_{typ}, was used to calculate the brightness of a disk model in both the IHW18 and N wavebands, using $P(\lambda, r)$ from the appropriate lines on the plots of Figs. 7.3d and 7.3f. There is just one D_{typ} that simultaneously matches the disk's observed brightnesses in both wavebands.

An initial estimate for D_{typ} was made based on the flux densities observed in the two wavebands: the flux densities of the disk in the IHW18 and N wavebands are 857 and 40 mJy, respectively (T2000); i.e., the observed flux density ratio (N/IHW18) is $O(0.05)$. The expected flux density ratio of the two wavebands (the ratio of $P(\lambda, r)$ for different D_{typ}) is plotted in Fig. 7.4. Assuming the emission to arise mostly from particles near the inner edge of the disk, $r = 60$-80 AU, Fig. 7.4 shows that the observed emission can be fairly well-constrained to come from particles with $D_{typ} = 2 - 3$ μm.

7.2.3 Pericenter Glow

Fig. 7.5 shows a contour plot of an unsmoothed IHW18 waveband observation of the disk model of Fig. 7.2 viewed face-on (i.e., perpendicular to the disk's plane of symmetry, y_f). This shows the observational consequence of the offset center of symmetry of the disk model. Because the particles at the inner edge of the disk (those that contribute most to the disk's brightness) are closer to the star in the forced pericenter direction, $\tilde{\omega}_f$, than those in the forced apocenter direction (Fig. 7.2), they are hotter and so contribute more to the disk's thermal emission than those at the forced apocenter. This is the "pericenter glow" phenomenon, which leads to the horseshoe-shaped highest contour line (the filled-in 1.02 mJy/pixel line), which is pointed in the $\tilde{\omega}_f$ direction. This asymmetry is a consequence of a_{min} and e_f only, and its magnitude is determined by e_f only. In particular, if there is a gradient of e_f across the disk, then it is e_f at the inner edge of the disk that controls the magnitude of the asymmetry. The outermost contour plotted on Fig. 7.5, which is an offset circle with a radius of 95 AU, is that corresponding to 0.17 mJy/pixel. Thus, there is little emission from the outer edge of the disk, justifying the arbitrary use of $a_{max} = 130$ AU in the modeling.

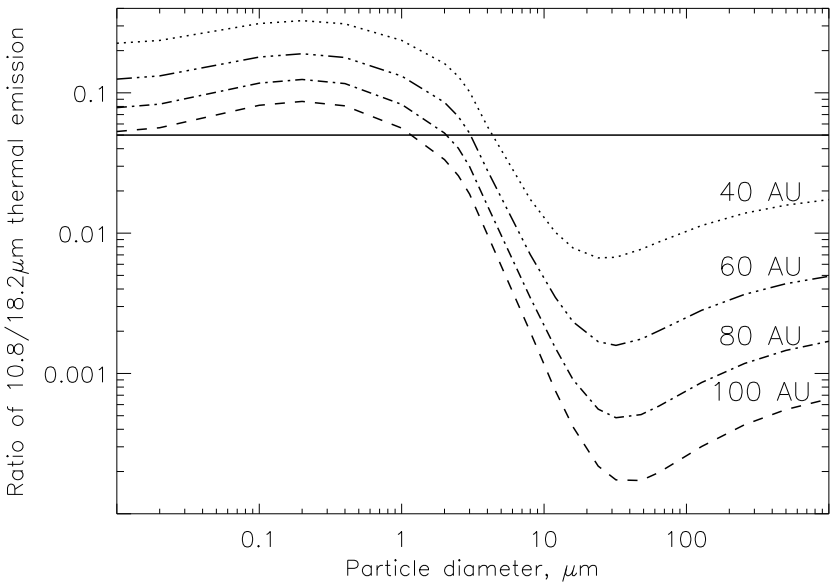

Figure 7.4: The ratio of the thermal emission in the N, 10.8 μm, and IHW18, 18.2 μm, wavebands, of astronomical silicate Mie spheres of different sizes at 40, 60, 80, and 100 AU from HR 4796A (i.e., Fig. 7.3e divided by Fig. 7.3c). Assuming the disk's flux densities in the two wavebands to be dominated by the emission of particles at 60-80 AU, the observed ratio of flux densities, $O(0.05)$ (T2000; §7.2.2), can be used to estimate that the disk's emitting particles have $D_{typ} = 2 - 3$ μm.

7.3 Disk Model Orientation

The two variables that define the orientation of the HR 4796 disk to the line of sight of the observation are $\tilde{\omega}_f$ and I_{obs}; how they define this orientation is best explained using Fig. 7.5. Imagine that the disk starts face-on with the forced pericenter direction pointing to the left. It is then rotated clockwise by $\tilde{\omega}_f$ (this is shown in Fig. 7.5, where $\tilde{\omega}_f = 26°$), and then tilted by $90° - I_{obs}$ about the dotted line on Fig. 7.5. The direction of this tilt, whether the top or bottom of the disk ends up closer to the observer, is not constrained in the modeling, since no account was made for either the extinction of the disk's emission by the disk itself, or for the disk's scattered light (e.g., an observer would see forward-scattered starlight from the closest part of the disk and back-scattered starlight from the farthest part, a phenomenon that could produce an apparent asymmetry in a symmetric disk, Kalas & Jewitt 1995). If the resulting inclination of the disk's symmetry plane to the line of sight, I_{obs}, is small, then the resulting nearly edge-on observation shows two lobes, one either side of the star. Since the hotter, brighter, pericenter glow material is predominantly in one of the lobes (unless $\tilde{\omega}_f = 90°$), the lobes have asymmetric brightnesses.

7.4 Modeling Process and Results

Pseudo-observations of disk models in the IHW18 and N wavebands were produced that mimicked the real OSCIR (the University of Florida mid-IR imager) observations in both pixel size, 1 pixel = 0.″0616 = 4.133 AU at 67 pc, and smoothing, using the observed PSFs (which are asymmetric and slightly fatter than diffraction limited, T2000), and including the post-observational gaussian smoothing of FWHM = 3 pixels. The model variables: a_{min}, γ, I_{obs}, e_f, $\tilde{\omega}_f$, and σ_{tot}, were optimized so that the modeled IHW18 observation correctly predicts the observed IHW18 brightness distribution; at the same time, the variable, D_{typ}, was optimized so that the modeled N band observation correctly predicts the observed N band brightness.

The model observations were compared with the real observations using the following diagnostics: the lobe brightnesses, $F_{ne,sw}$, and their projected radial offsets from HR 4796A, $R_{ne,sw}$,

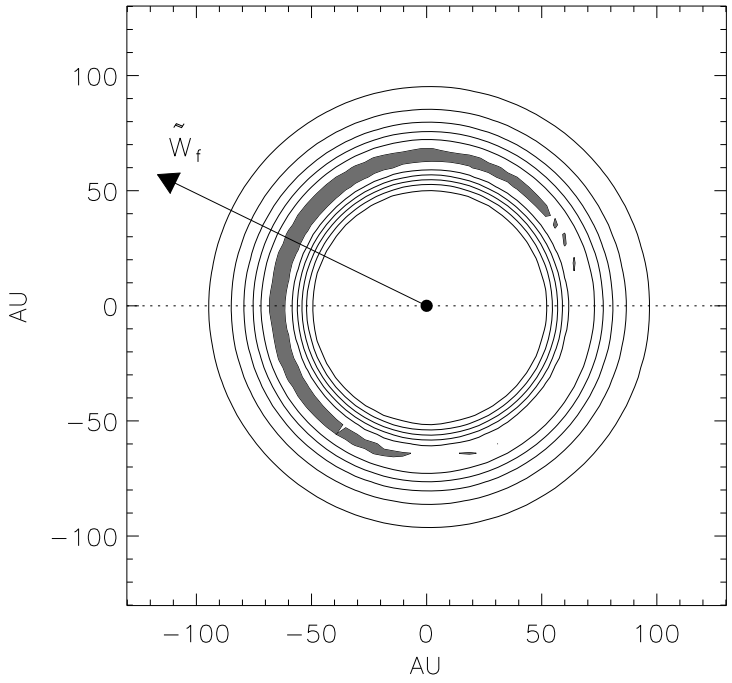

Figure 7.5: Contour plot of an unsmoothed face-on view of the HR 4796 disk model (shown also in Fig. 7.2) seen in the IHW18 (18.2 μm) waveband. The contours are spaced linearly at 0.17, 0.34, 0.51, 0.68, 0.85, and 1.02 mJy/pixel. The disk's offset causes particles in the forced pericenter direction, located at a position angle of $90° - \tilde{\omega}_f$, where $\tilde{\omega}_f = 26°$, as measured from North in a counterclockwise direction, to be hotter, and hence brighter, than those in the forced apocenter direction; this is the "pericenter glow" phenomenon, evident in this figure by the shape of the brightest (filled-in) contour. The geometry of the observation is defined such that the disk as it is shown here is rotated by a further $90° - I_{obs}$ about the dotted line, where $I_{obs} = 13°$.

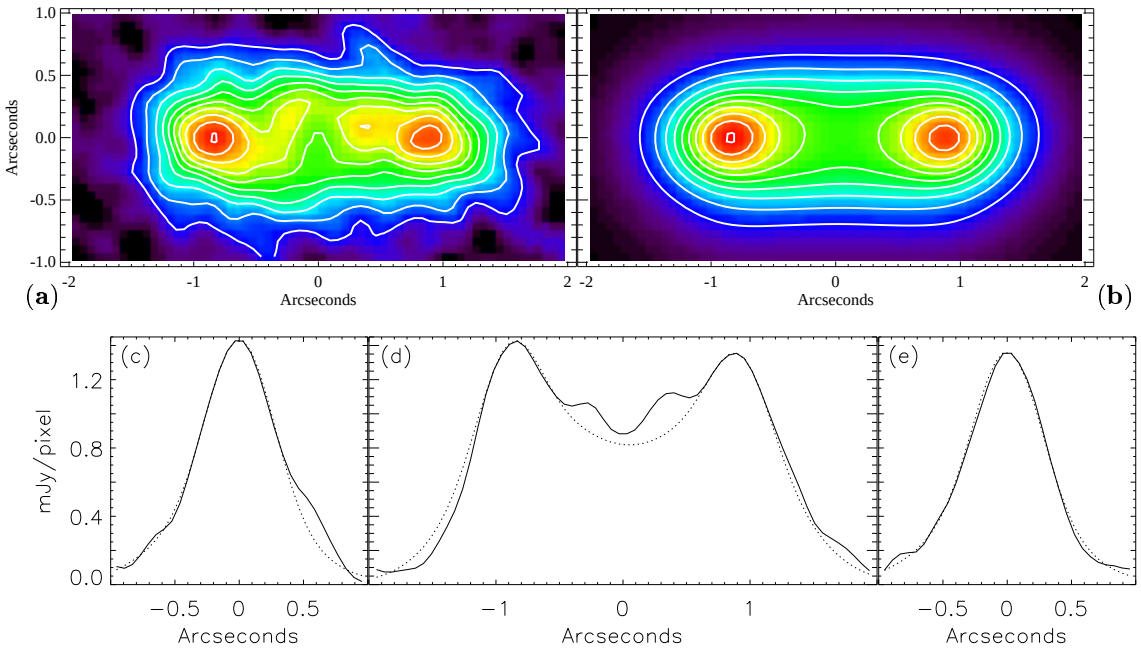

Figure 7.6: Comparison of the HR 4796 disk model observation with the real observation. *Top* — False color images of HR 4796 in the IHW18 (18.2 μm) waveband. Both the observation (**a**), on the left, and the model (**b**), on the right, have been rotated to horizontal with the NE lobe on the left. The contours are spaced linearly at 0.22, 0.35, 0.49, 0.62, 0.75, 0.89, 1.02, 1.15, 1.29, and 1.42 mJy/pixel. The observation has had the photospheric emission of HR 4796A subtracted, and a 3 pixel FWHM gaussian smoothing applied. The image of the model mimics the observation both in pixel size (1 pixel = $0\farcs0616$ = 4.133 AU) and smoothing (using an observed PSF and including the 3 pixel post-observational smoothing). *Bottom* — Line-cuts in the vertical direction through the NE (**c**) and SW (**e**) lobes, and in the horizontal direction through the center of both lobes (**d**). The observations are shown with a solid line and the model with a dotted line.

that were found by fitting a quintic polynomial surface to a 10×10 pixel region around each of the lobes with 0.1 pixel resolution (the location of HR 4796A in the real observations was also found in this way); and line-cuts through the disk both parallel (e.g., Figs. 7.6d and 7.7), and perpendicular (e.g., Figs. 7.6c and 7.6e) to the line joining the two lobes in the IHW18 observations. An understanding of how the different model variables affect the different diagnostics allowed the modeling process to be decoupled into solving for: the disk's symmetrical structure, defined by I_{obs}, a_{min}, and γ; the particle size D_{typ}; and the disk's asymmetrical structure, defined by e_f and $\tilde{\omega}_f$. Throughout the modeling, the amount of material in a model, σ_{tot}, was scaled so that the model observation predicted the correct observed mean brightness of the lobes in the IHW18 waveband, $F_{mean} = (F_{ne} + F_{sw})/2 = 1.40 \pm 0.02$ mJy/pixel; its final value, $\sigma_{tot} = 2.03 \times 10^{24}$ m^2, was calculated once the other variables had been constrained.

7.4.1 Symmetrical Disk Structure

Since e_f and $\tilde{\omega}_f$ only pertain to the disk's asymmetrical structure, then for a given D_{typ}, the variables pertaining to the disk's symmetrical structure, I_{obs}, a_{min}, and γ, could be solved using a model with $e_f = 0$; such a model is axisymmetric, and so the variable $\tilde{\omega}_f$ is redundant. The inclination of the disk's plane of symmetry to the line of sight, $I_{obs} = 13 \pm 1°$, was constrained to give the best fit to the line-cuts perpendicular to the lobes (Figs. 7.6c and 7.6e); this inclination agrees with that found by previous models of HR 4796 disk observations (Koerner et al. 1998; Schneider et al. 1999). Since the model is of a fat disk, a different proper inclination distribution would result in a different I_{obs}; e.g., if the disk is actually thinner than modeled here, $\langle I_p \rangle < 10.2°$, then the inferred I_{obs} is an underestimate, and vice versa. The inner edge of the disk, $a_{min} = 62 \pm 2$ AU, was constrained such that the model observation reproduces the observed mean radial offset of the lobes from HR 4796A, $R_{mean} = (R_{ne} + R_{sw})/2 = 58.1 \pm 1.3$ AU. The semimajor axis distribution, $\gamma = -2 \pm 1$, was constrained to give the best fit to the cut along the line joining the two lobes (Fig. 7.6d).

7.4.2 Particle Size

Since D_{typ} was already estimated to be about 2-3 μm (§7.2.2), the modeling of the disk's symmetrical structure was repeated for $D_{typ} = 2$, 2.5, and 3 μm. Adjusting D_{typ} by such a small amount did not affect the inferred symmetrical structure parameters. This was expected, since the $P(18.2\ \mu\text{m}, r)$ for each of these D_{typ} are very similar (Fig. 7.3d). Remembering that the model is always normalized to predict the observed mean IHW18 lobe brightnesses, the predicted N band lobe brightnesses are compared for the three values of D_{typ} in Fig. 7.7. This shows that the particle size can be constrained to be $D_{typ} = 2.5 \pm 0.5$ μm; i.e., the crude method of calculating the particle size of §7.2.2 gives a very good estimate of this size. This particle size means that the total mass of emitting particles in the disk model is $\sim 1.4 \times 10^{-3} M_\oplus$, where $M_\oplus = 3 \times 10^{-6} M_\odot$ is the mass of the Earth. However, this is not a useful constraint on the disk's mass, since the disk's mass is expected to be concentrated in its largest particles. The best estimate of the mass of the HR 4796 disk, from submillimeter observations, is that it is between $0.1 M_\oplus$ and $1.0 M_\oplus$ (Jura et al. 1995; Jura et al. 1998), which, as expected, is well above the mass of this disk model.

7.4.3 Asymmetrical Disk Structure

The disk's observed asymmetries are defined by the lobe brightness asymmetry, $(F_{ne} - F_{sw})/F_{mean} = 5.1 \pm 3.2\%$, and the radial offset asymmetry, $(R_{sw} - R_{ne})/R_{mean} = 6.4 \pm 4.6\%$. These asymmetries are also apparent in the disk model, and their magnitudes are determined by both e_f and $\tilde{\omega}_f$. The lobe brightness asymmetry was used to constrain e_f and $\tilde{\omega}_f$, and it was found that the forced eccentricity needed to cause the $5.1 \pm 3.2\%$ asymmetry depends on the geometry of the observation according to the relation shown in Fig. 7.8. Thus, for the majority of the geometries, a forced eccentricity of between 0.02 and 0.03 is sufficient to cause the observed brightness asymmetry. In the context of this modeling, the observed brightness asymmetry implies a radial offset asymmetry

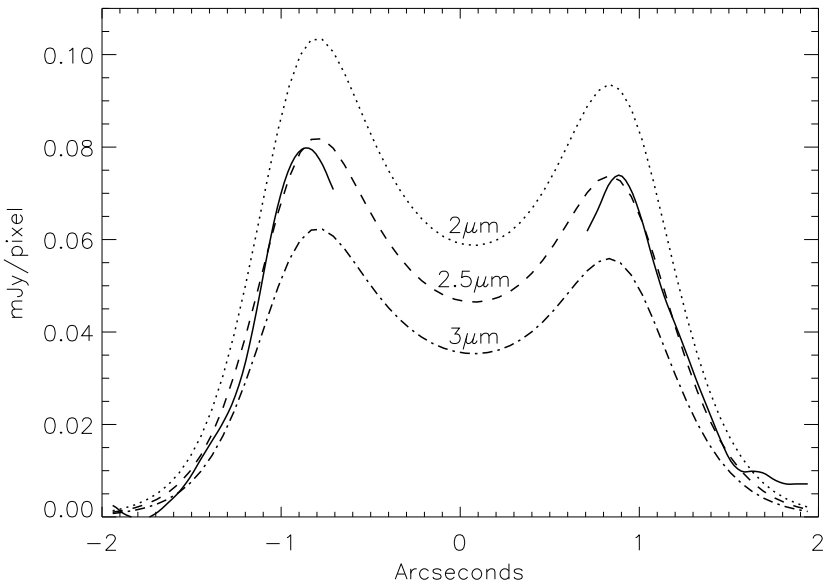

Figure 7.7: Horizontal line-cuts along the plane of the lobes in the N (10.8 μm) band. The observation is shown with a solid line and models with particle diameters of D_{typ} = 2, 2.5, and 3 μm are shown with dotted, dashed, and dash-dot lines. The total amount of cross-sectional area in the models, σ_{tot}, has been scaled to fit the observed mean brightness of the lobes in the IHW18 (18.2 μm) waveband; the model with D_{typ} = 2.5 μm gives the best fit to the observed lobe brightnesses in the N band. The observed N band flux density is not well constrained within 0.″8 of HR 4796A due to imperfect subtraction of the stellar photosphere from the image (T2000), and so it is not shown here.

of $\sim 5\%$, which is within the limits of the observation. The final model shown in Figs. 7.2, 7.5, 7.6, and 7.7 assumes a modest value of $e_f = 0.02$, which corresponds to a disk orientation described by $\tilde{\omega}_f = 26°$ (Fig. 7.8). Whether this rotation puts the pericenter glow material above or below the horizontal, $\tilde{\omega}_f = 26°$ or $-26°$, is not constrained here, since it has a minimal effect on the observation: in the model observation of Fig. 7.6, the top of the disk is brighter than the bottom of the disk by a fraction that would be undetectable in the observation due to noise and the disk's unknown residual structure. The line-cuts of Fig. 7.6 show how well the model fits all aspects of the observation — the vertical structure, the horizontal structure, and the lobe location and asymmetry.

7.4.4 Statistical Significance

The standard deviations of the OSCIR lobe observations quoted in this chapter were found using model observations that mimicked the noise present in the OSCIR observations. The background sky noise in the IHW18 observation was found to be approximately gaussian with zero mean and a 1σ noise per pixel of 0.15 mJy (T2000). In a noisy model observation, such a random noise field was included after the PSF smoothing, but before the post-observational smoothing. Observations of noisy models were repeated for 50,000 different noise fields to obtain the quoted standard deviations. Since the observed PSF was asymmetric (T2000), this introduces an apparent lobe asymmetry of -0.8% in an observation of a symmetric disk (i.e., one with $e_f = 0$), and so the observed lobe asymmetry is $5.9 \pm 3.2\%$ from the mean, and its statistical significance is 1.8σ. While this is small, it does show that the pericenter glow phenomenon is observable with current technology: HR 4796 was observed with the infrared imager OSCIR for only one hour on Keck II (T2000); in the background-limited regime, the significance level of any asymmetry increases at a rate $\propto \sqrt{t}$; thus, one good night on a 10 meter telescope should be enough to get a definitive observation of the HR 4796 lobe asymmetry. The real significance of the HR 4796 asymmetry may also be higher than

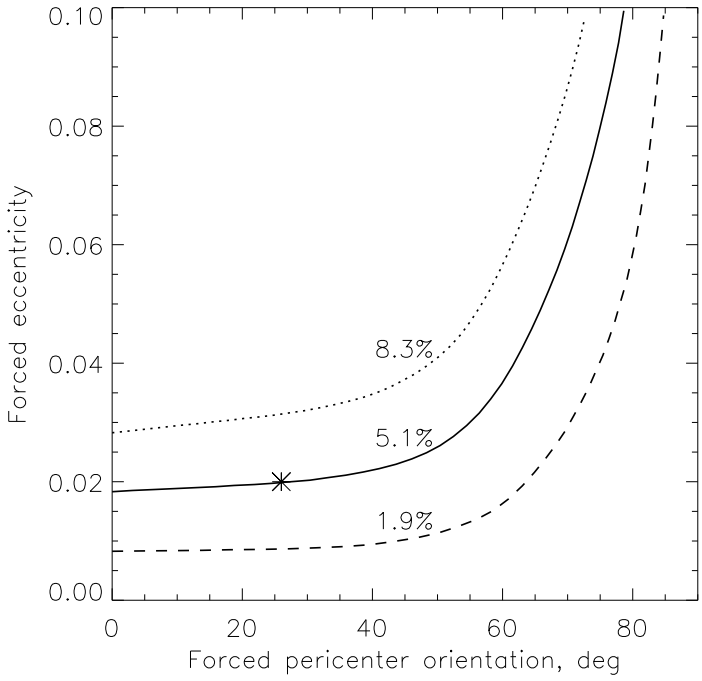

Figure 7.8: Relation of the forced eccentricity, e_f, to the orientation of the longitude of forced pericenter, $\tilde{\omega}_f$, in the model needed to achieve the observed lobe brightness asymmetry of $5.1 \pm 3.2\%$ (a similar relationship is required to achieve the observed radial offset). A forced eccentricity as small as 0.02 would suffice to achieve the observed asymmetry, but a higher forced eccentricity could be necessary if the forced pericenter is aligned in an unfavorable direction. The final model, shown in Figs. 7.2, 7.5, 7.6, and 7.7, has $e_f = 0.02$ and $\tilde{\omega}_f = 26°$, and this point is shown with an asterisk on this plot.

quoted above, since it also seems to be apparent in other observations of this disk (Koerner et al. 1998; Schneider et al. 1999). Even if subsequent observations happen to disprove the existence of the asymmetry, this is still significant, since, as §8.2 shows, an asymmetry is to be expected if the companion star, HR 4796B, is on an eccentric orbit.

CHAPTER 8
INTERPRETATION OF THE DYNAMIC HR 4796 DISK MODEL

The interpretation of the HR 4796 disk model is broken down into sections that cover discussions of: the dynamics of the disk particles, §8.1; the lobe asymmetry, §8.2; the emitting particle category, §8.3; the origin of the inner hole, §8.4; and the residual structure of the observation once the model has been subtracted, §8.5.

8.1 The Dynamic HR 4796 Disk

An interpretation of the observed structure of the HR 4796 disk starts with a discussion of the dynamics of the particles in the disk, and where the emitting particles fit into our understanding of the dynamic disk (Chapter 3). In all calculations, the mass of HR 4796A was assumed to be $M_\star = 2.5 M_\odot$ (Jayawardhana et al. 1998).

8.1.1 Radiation Forces, β

The radiation forces, defined by β (eq. [3.22]), acting on particles in the HR 4796 disk can be found from their optical properties. Fig. 8.1 shows the β of particles with the optical properties assumed in this model (§7.2.1). Thus, particles in the disk with $D < 8$ μm are β meteoroids (even the submicron particles have $\beta > 0.5$), and a good approximation for the non-β meteoroids is:

$$\beta \approx 4/D, \tag{8.1}$$

where D is measured in μm (in agreement with eq. [3.23]). Fig. 7.7 shows that the emitting particles have $D_{typ} \approx 2.5$ μm; these particles have $\beta = 1.7$. So, the modeling implies that the emitting particles are β meteoroids, i.e., that they are blown out of the system on hyperbolic orbits. Since the lifetime of β meteoroids is $O(370$ years) for those created at ~ 70 AU, which is much shorter than the age of the HR 4796 system, any β meteoroids that are currently in the disk cannot be primordial particles, rather they must be continuously created from a reservoir of larger particles; i.e., the existence of β meteoroids implies the existence of a dynamically stable population of larger particles.

If the emitting particles are on hyperbolic orbits, we can use the mass of the disk's emitting particles, $\sim 1.4 \times 10^{-3} M_\oplus$, and the emitting lifetime of these particles, ~ 370 years, to estimate the mass loss rate of the disk to be $\sim 4 \times 10^{-6} M_\oplus$/year. If this mass loss rate has been sustained over the age of the system, the original disk must have been $\sim 40 M_\oplus$ more massive than it is today. In fact, a more massive disk would have had a higher mass loss rate, since this rate increases proportionally with the total cross-sectional area in the disk (i.e., $\propto m_{tot}^{2/3}$). This means that if the current disk has a mass $1.0 M_\oplus$, the original disk must have had a mass $\sim 7 \times 10^4 M_\oplus$ (see eq. [3.41]); i.e., the HR 4796 disk may provide evidence for the type of collisional mass loss that may have happened in the early Kuiper belt (Stern & Colwell 1997).

8.1.2 Collisional Processes

The collisional lifetime of the disk's emitting particles can be calculated directly from the disk model using equations (3.12) and (3.17): $t_{coll}(D_{typ}) < 10^4$ years across most of the disk (55-85 AU), with a minimum at ~ 70 AU of ~ 4500 years. This collisional lifetime is much less than the age of the HR 4796 system. Thus, the emitting particles cannot be primordial particles (irrespective of whether they are β meteoroids). The collisional lifetime of the emitting particles can be corroborated

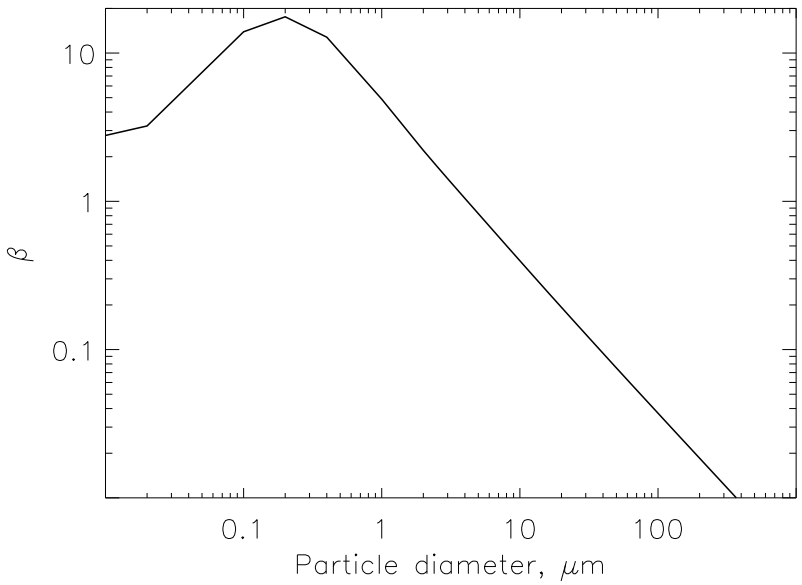

Figure 8.1: The ratio, β, of the radiation pressure force to the gravitational force acting on astronomical silicate Mie spheres of different sizes in the HR 4796 disk.

using equation (3.18). The model's effective optical depth (eq. [3.13]) is its surface density, plotted in Fig. 7.2, multiplied by the cross-sectional area of a particle in the model, $\sigma = \pi D_{typ}^2/4$. This peaks at 70 AU, where $\tau_{eff}(70 \text{ AU}) = 5 \times 10^{-3}$, and $t_{per} = O(370 \text{ years})$, giving a collisional lifetime that has a minimum of $t_{coll}(D_{typ}) \approx 6000$ years. The disk's effective optical depth at 70 AU, $\tau_{eff}(70$ AU), can also be corroborated directly from the observation using equation (3.15). The observed edge-on, smoothed lobe brightness is ~ 1.40 mJy/pixel; this can be scaled to the unsmoothed face-on brightness by the factor 1.10/1.40 (see Figs. 7.5 and 7.6b), which, since each pixel subtends $(0.0616 * \pi/648000)^2$ sr, gives a brightness of $F_\nu(18.2\ \mu\text{m}, 70 \text{ AU})/\Omega_{obs} = 12 \times 10^9$ Jy/sr. For 2.5 μm particles, Figs. 7.3c and 7.3d give $P(18.2\ \mu\text{m}, 70 \text{ AU}) \approx 2.2 \times 10^{12}$ Jy/sr, thus confirming that $\tau_{eff}(70$ AU$) \approx 5 \times 10^{-3}$; this is also in agreement with $\tau \approx 5 \times 10^{-3}$ found by Jura et al. (1995). In fact, assuming that the disk's total IHW18 flux density, 857 mJy (T2000), comes from particles between 70 ± 15 AU, the unsmoothed face-on brightness of the disk can also be corroborated; equation (3.16) with $R_\star = 67$ pc gives $F_\nu(18.2\ \mu\text{m}, 70 \text{ AU})/\Omega_{obs} = O(10^{10}$ Jy/sr).

Since particles are only broken up by collisions with particles that have diameters more than a tenth of their own (eq. [3.7]), the collisional lifetime of the disk's large particles must be longer than that of the smaller emitting particles. Assuming the cross-sectional area distribution to follow equation (3.5) with $q = 11/6$ down to particles of size D_{typ}, the collisional lifetime of particles with $D \gg D_{typ}$ can be estimated to be (eq. [3.21]):

$$t_{coll} \approx 4 \times 10^7 \sqrt{D}, \tag{8.2}$$

where t_{coll} is measured in years, and D in km. Since particles for which $t_{coll} < t_{sys}$ cannot be primordial, this implies that particles currently in the HR 4796 disk that are smaller than 60 m cannot be original, rather they must have been created in the break-up of larger particles; i.e., these disk particles form a collisional cascade, through which the spatial distributions of the smaller particles are related to that of the larger particles. Particles in the disk that are larger than 60 m could be primordial.

8.1.3 P-R Drag

The disk's high effective optical depth means that $\beta_{pr} = 132$ at 70 AU (eq. [3.31]), which in turn means that there is not expected to be significant P-R drag evolution for any of the disk's particles. Analysis of the P-R drag evolution of disk particles shows that even the most affected particles, those with $\beta = 0.5$, have a P-R drag lifetime of $t_{pr} = O(1.6$ Myr) at 70 AU (eq. [3.30]), and that these particles would only make it to ~ 69.8 AU before they are broken up by collisions and blown out of the system by radiation pressure.

But, P-R drag could still be important for disks in which the individual particles of that disk are not affected significantly by P-R drag in their lifetime. While the inner edge of a disk's largest particles may be at a_{min}, the cumulative effect of P-R drag on all of the stages of the collisional cascade that a primordial particle goes through before the fragments are small enough to be blown out of the system by radiation pressure could mean that the inner edge of these blow-out particles is further in than a_{min}. To assess whether the cumulative effect of P-R drag has an impact on the inner edge of the emitting particles in the HR 4796 disk, consider its size distribution to follow that assumed in equation (3.19), where $D_{min} = D_{typ} = 2.5$ μm, and $q = 11/6$. The lifetime of an intermediate particle can be found using equations (3.14) and (3.20), and the amount of P-R drag evolution in its lifetime is given by (eqs. [3.28] and [8.1]):

$$da \approx -0.0125 t_{coll}(D, r)/Da, \tag{8.3}$$

where da and a are measured in AU, D in μm, and $t_{coll}(D, r)$ in years. Assuming that the largest fragment created in a collision has a diameter half that of the original particle, a β meteoroid particle (e.g., a 2.5 μm particle) at 62 AU, assuming it to have originated from a gravitationally bound particle (i.e., one with $\beta < 0.5$), can at the very most be removed by 27 generations from its primordial ancestor, which would at the very most have been originally at 62.1 AU.

8.1.4 The Dynamic HR 4796 Disk

Since P-R drag is not an important process in the HR 4796 disk's evolution, there are just three categories of particles in the disk: large particles, β critical particles, and β meteoroids. If the modeled emitting particle size is to be believed (discussed further in §8.3), the particles that are seen in both the IHW18 and the N band observations are the disk's β meteoroids. Since the disk was modeled as if the emitting particles are large particles, this inconsistency needs to be borne in mind in the interpretation of the model.

While the modeling used a distribution of orbital elements that is only appropriate for the disk's large particles, it was the spatial distribution of the disk's emitting material, $\sigma(r, \theta, \phi)$, that was constrained by the modeling, not the distribution of orbital elements, $\sigma(a, e, I, \Omega, \tilde{\omega})$. Therefore, the inferred distribution, $\sigma(r, \theta, \phi)$, which is that shown in Fig. 7.2, is an accurate description of the spatial distribution of the disk's emitting particles, whatever their size. Indeed, it is in excellent agreement with that inferred from other observations of the HR 4796 disk (Jayawardhana et al. 1998; Koerner et al. 1998; Schneider et al. 1999). If the emitting particles are the disk's large particles, then the inferred model variables have physical interpretations for the distribution of the orbits of the disk's large particles. If, as appears to be the case, the emitting particles are β meteoroids, then further modeling of $\sigma(r, \theta, \phi)$ needs to be done to infer the distribution of the orbits of these particles.

However, since the disk's β critical and β meteoroid particles are created from its large particles, the spatial distributions of all of these particles share a great deal in common (see §§3.4 and 4.1.3): they all have the same plane of symmetry, the same flaring, and the same offset and warp asymmetries, but the radial distributions of the smaller particles are more extended than that of the large particles. This means that if we are seeing the disk's β meteoroids, then the spatial distribution of its large particles has a plane of symmetry that is defined by I_{obs}, and an inner edge that is at the same radial location, and that is offset by the same amount and in the same direction, as that shown in Fig. 7.2; their radial distribution, however, would not be as extended as that of Fig. 7.2.

Thus, the model parameters a_{min}, e_f, and $\tilde{\omega}_f$ have physical interpretations for the distribution of the orbits of the disk's large particles, irrespective of the size of the emitting particles.

8.2 Interpretation of Lobe Asymmetry: HR 4796's Secular Perturbations

The lobe asymmetry in the model of Chapter 7 is due solely to the offset inner edge of the disk. The model shows that secular perturbations amounting to a comparatively small forced eccentricity, $e_f = 0.02$, imposed on the orbits of large particles at the inner edge of the disk, $a = 62$ AU, would cause the disk's inner edge to be offset by a sufficient amount to cause the observed 5% lobe asymmetry. This section considers what kind of a perturber system would impose such a forced eccentricity on the inner edge of the disk, and whether such a system is physically realistic. A discussion of the system's secular perturbations also allows interpretation of the disk's inferred orientation, defined by the parameters $\tilde{\omega}_f$ and I_{obs}.

If HR 4796A's binary companion, HR 4796B, is on an eccentric orbit, it would have imposed a forced eccentricity on the disk particles. However, a forced eccentricity could also have been imposed on the disk by an unseen planet close to the inner edge of the disk, a planet which could be responsible for clearing the inner region (e.g., Artymowicz & Lubow 1994; Roques et al. 1994). The secular perturbations imposed on the HR 4796 disk by a perturber system that includes HR 4796B and a putative planet located at the inner edge of the disk are shown in Fig. 8.2 for the four cases: $M_{pl} = 0$, $M_{pl} = 0.1 M_J$, $M_{pl} = 10 M_J$, and just planet. The parameters of the two perturbers are assumed to be:

HR 4796B $M_B = 0.38 M_\odot$(Jayawardhana et al. 1998); the orbit of HR 4796B is unknown at present (Jura et al. 1993), so the semimajor axis of its orbit is arbitrarily taken as its projected distance, $a_B = 517$ AU (Jura et al. 1998; note that this is not the same as assuming that this is the semimajor axis of the ellipse that the star's orbit traces on the sky) — this gives an orbital period of ~ 7000 years (eq. [3.2]), and a timescale for secular perturbations from HR 4796B to have built up at 62 AU of $O(1$ Myr) (eq. [4.18]); $e_B = 0.13$, the eccentricity necessary to cause $e_f = 0.02$ at $a = 62$ AU if there were no unseen perturbers (eq. [4.16]); $I_B = 0°$, defining the reference plane for the analysis.

Planet M_{pl} is a variable measured in Jupiter masses, where $M_J = 10^{-3} M_\odot$ (current observations have limited the size of a planet in the system to $M_{pl} < 200 M_J$, Jura et al. 1998); $a_{pl} = 47$ AU (see §8.4); $e_{pl} = 0.023$, the eccentricity necessary to cause $e_f = 0.02$ at $a = 62$ AU if the planet was the only perturber (eq. [4.16]); $I_{pl} = 5°$, an arbitrary choice that represents the fact that the orbital plane of the planet is not necessarily be aligned with that of HR 4796B.

8.2.1 Just HR 4796B

For the cases when there is just one perturber in the system, the forced elements in the system can be found from equations (4.16) and (4.17): the forced eccentricity, e_f, is determined by the ratio of the semimajor axes of the perturber and the particle, and by the eccentricity of the perturber's orbit, but is independent of the perturber's mass; the forced pericenter, $\tilde{\omega}_f$, is aligned with the pericenter of the perturber; and the plane of symmetry of the disk, y_f, is constant across the disk, and is the orbital plane of the perturber.

So, if the only perturber is HR 4796B, then to impose $e_f = 0.02$ at $a = 62$ AU, the eccentricity of its orbit would have to be $e_B = 0.13$; the consequent forced eccentricity imposed on the disk is plotted in Fig. 8.2a. This also means that if $e_B > 0.1$, then a brightness asymmetry in this disk of $> 5\%$ would be expected unless adverse geometrical conditions prevented it. The position angle from north of HR 4796B relative to HR 4796A is 225° (Jayawardhana et al. 1998), while that of the SW lobe (i.e., the least bright lobe) is 206° (T2000). For the lobe asymmetry to be the consequence of perturbations from HR 4796B only, HR 4796B must currently be close to its apastron, and its orbital plane must be the plane of symmetry of the disk, i.e., inclined at 13° to

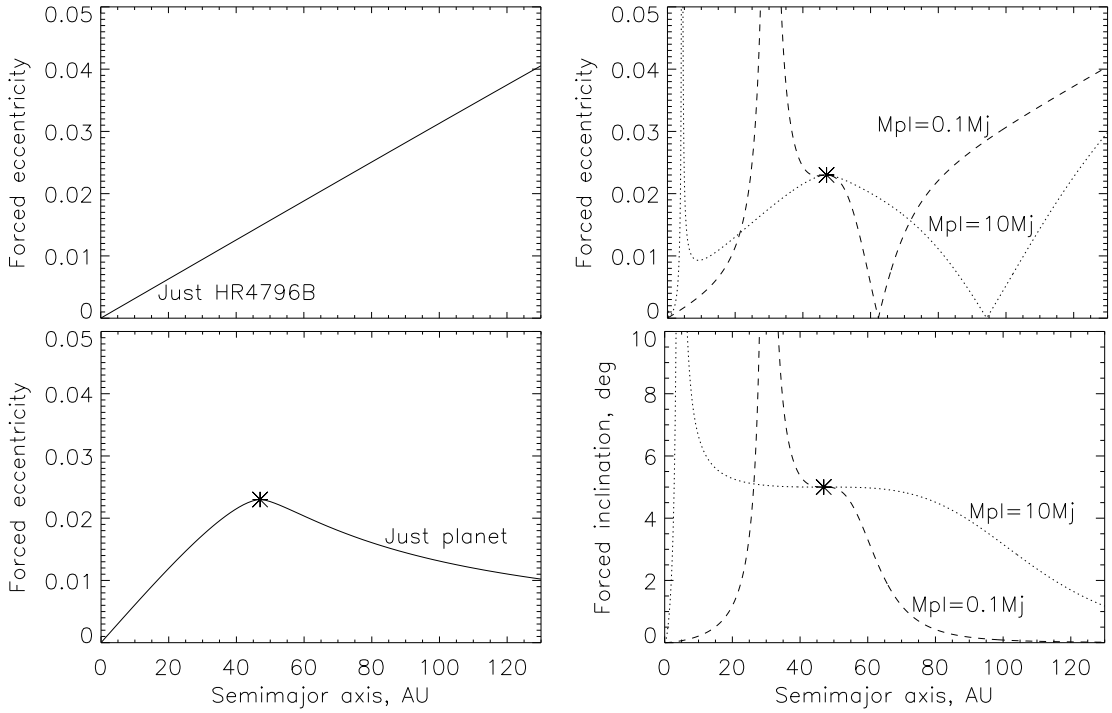

Figure 8.2: Plots of the forced eccentricities imposed on the orbits of particles in the HR 4796 system as a function of their semimajor axes, assuming different combinations of perturbers in the system: (**a**) HR 4796B only; (**b**) HR 4796B and a planet at the inner edge of the disk; (**c**) a planet only. The forced inclinations imposed by the two perturber system are shown in (**d**). The inner edge of the disk is at $a = 62$ AU. HR 4796B and the planet are assumed to have: $M_B = 0.38 M_\odot$, $a_B = 517$ AU, $e_B = 0.13$, and $I_B = 0$; $M_{pl} = 0.1$ and 10 M_J, where M_J is the mass of Jupiter, $a_{pl} = 47$ AU, $e_{pl} = 0.023$, and $I_{pl} = 5°$. The orbital elements of the planet are marked by an asterisk on the forced elements plots. In a one perturber system the forced eccentricity is independent of the mass of the perturber, and the forced inclination is the plane of the perturber's orbit. In a two perturber system, the shapes of the forced element plots depend on the mass of the planet, and the forced eccentricity also depends on the orientations of the perturbers' orbits. The forced eccentricity is plotted in (**b**) assuming that $\tilde{\omega}_{pl} = \tilde{\omega}_B + 180°$. This means that $\tilde{\omega}_f = \tilde{\omega}_{pl}$ for $a < a_{crit}$, and $\tilde{\omega}_f = \tilde{\omega}_B$ for $a > a_{crit}$, where a_{crit} is the semimajor axis of a particle's orbit for which $e_f = 0$; a similar alignment with the perturbers' orbital planes seen in the plot of the particles' forced inclinations. Thus, the lobes have both their asymmetries and their plane of symmetry aligned with the orbit of the planet if $M_{pl} > 0.1 M_J$, and with the orbit of HR 4796B if $M_{pl} < 0.1 M_J$.

the line of sight. All of these conclusions are consistent with the initial estimate that the semimajor axis of the star's orbit is equal to its observed projected distance, 517 AU.

8.2.2 HR 4796B and a Planet

Consider the effect of adding a planet at the inner edge of the disk into the HR 4796 system[1]. If there are two perturbers in the system, then the forced element variation with semimajor axis depends both on the masses of the perturbers and on the orientations of their orbits. In the plot of Fig. 8.2b, $\tilde{\omega}_{pl} = \tilde{\omega}_B + 180°$ was chosen so that the forced eccentricity (and hence the lobe asymmetry) is aligned with the planet's pericenter for $a < a_{crit}$, and aligned with HR 4796B's pericenter for $a > a_{crit}$, where a_{crit} is the semimajor axis for which $e_f = 0$. Since the two perturbers were also chosen to have different orbital planes, a similar change in the disk's alignment is seen in the plot of I_f (Fig. 8.2d): the disk's plane of symmetry is aligned with the planet's orbital plane at its inner edge, and with the orbital plane of HR 4796B at its outer edge; this could cause an image of the disk to appear warped. Such a warp could be modeled using the same modeling techniques that are described in this dissertation, and would provide further constraints on the perturbers in the system (even if no warp was observed).

So, it is possible that the brightness asymmetry, and the symmetry plane of the lobes, are determined by a planet close to the edge of the disk that has $M_{pl} > 0.1 M_J$, rather than by HR 4796B. Using such an analysis, the pericenter glow phenomenon could be used to test for the existence of a planet in the HR 4796 system, but only after the orbit of HR 4796B has been determined; e.g., if $\tilde{\omega}_B$, e_B or the plane of HR 4796B's orbit contradicted the observed asymmetry orientation, brightness asymmetry magnitude, or the plane of symmetry of the lobes, then the existence of a planet at the inner edge of the disk with $M_{pl} > 0.1 M_J$ could be inferred.

8.2.3 Just Planet

A double-lobed disk structure could also be observed in a system with no observable companion. The only possible perturber in such a system is an unseen planet, the secular perturbations of which warrant the same kind of discussion as for the case when HR 4796B was the only perturber (§8.2.1). Depending on the planet's mass, radial location and eccentricity, it too could give rise to a detectable pericenter glow. The only constraint on the planet's mass is that the disk must be old enough for its secular perturbations to have affected the distribution of orbital elements of the disk particles over the age of the system. Since it takes of the order of one precession timescale to distribute the complex eccentricities of collisional fragments around the circle centered on the forced eccentricity, the constraint on the planet's mass can be approximated as that for which is that the age of the system, t_{sys}, is greater than the secular timescale, $t_{sec} \propto 1/M_{pl}$ (eq. [4.18]); for the HR 4796 system this limit is $M_{pl} > 10 M_\oplus$. The constraint on the planet's eccentricity is even less stringent than for the binary companion because the planet is closer to the edge of the disk: a planet in the HR 4796 system would only need an eccentricity of $e_{pl} > 0.02$ to produce the observed 5% lobe asymmetry, and the forced eccentricity imposed on the disk by a planet with $e_{pl} = 0.023$ is plotted in Fig. 8.2c. So, the signature of even a low-mass planet would not escape detection and symmetrical double-lobed features are unlikely to be observed in systems that contain planets.

8.2.4 Other Considerations

If the disk itself is massive enough to cause significant gravitational perturbations to the orbits of the disk particles, then the mass of the disk should be incorporated into the analysis of the secular perturbations in the system. A massive disk could dampen the eccentricity of a planet at the inner edge of the disk (Ward & Hahn 1998), thus reducing the offset asymmetry.

[1] The orbital elements of a low-mass planet in the system would, just like the disk particles, have forced and proper components, while a high-mass planet would perturb the orbit of HR 4796B.

8.3 Discussion of Emitting Particle Category

The emitting lifetime of the disk's β meteoroids, $O(370$ years), is less than the emitting lifetime of their parents, $O(10^4$ years); equivalently, $\tau_{eff} < 0.1$. Thus, our understanding of the dynamic disk implies that the disk's cross-sectional area distribution should not contain a significant amount of β meteoroids. Rather, since there are no P-R drag affected particles in the disk, the disk's emission is expected to come from its β critical particles and its smallest large particles (§3.4.2). Not all disk particles have the same composition and morphology; even if this were a close approximation, there is, as yet, no evidence to suggest whether the particle properties chosen in this model (§7.2.1) are correct. Are we indeed seeing the disk's β meteoroid particles, or did the assumptions of the modeling lead us to this conclusion?

Consider the initial crude estimate of the particle size (§7.2.2); this proved to be an accurate method for estimating the particle size (§7.4.2). If different assumptions had been made about the particles' properties (e.g., if the particles had been assumed to have silicate cores with organic refractory mantles) or morphologies (e.g., if the particles had been assumed to be like the bird's nest structures of Gustafson 1994), both Figs. 7.4 and 8.1 would have been different, and a different conclusion might have been drawn about the β of the emitting particles. If a size distribution had been included in the modeling, this would also have affected the conclusion. These are considerations that need to be modeled before any firm conclusion about the dynamics of the emitting particles can be reached. However, since irrespective of their assumed properties large particles have black body temperatures and brightness ratios similar to those of the $D > 100$ μm particles in Fig. 7.4, a flexible interpretation of the observed brightness ratio is that the emitting particles must have temperatures that are hotter than black body. Thus, the emitting particles are either small (e.g., the simple analysis of §7.2.1 implies that $D < 10$ μm), in which case they are likely to be β meteoroids (e.g., 10 μm particles have $\beta > 0.5$ unless they have densities > 3000 kg/m^3, eq. [3.23]), or they are large particles that are made up of smaller hotter particles.

A preliminary investigation was carried out to determine the effects of the assumptions about the particles' optical properties on the conclusion about their dynamical category. It was worried that the choice of astronomical silicates for the particle composition might have biased the particle size estimate since the wavebands that were used to estimate that size lie on the silicate emission features, and so this size was re-estimated assuming the particles to be made of organic refractory material (Li & Greenberg 1997). The optical properties of organic refractory grains in HR 4796 are shown in Fig. 8.3, which is analogous to Fig. 7.3 for astronomical silicate grains; an explanation of the shape of the plots in Fig. 8.3 is similar to that for Fig. 7.3 (see §7.2.1). A crude estimate for the emitting particle size was found using Fig. 8.4, which is analogous to Fig. 7.4. Fig. 8.4 shows that if the particles in the HR 4796 disk had been modeled as organic refractory Mie spheres, then D_{typ} would have been estimated to lie in the range 12-20 μm. This was confirmed when the grain size was estimated more accurately using Fig. 8.5, which is analogous to Fig. 7.7. This would have implied that the emitting particles have a β in the range 0.2-0.5, i.e., that the emitting particles are the disk's β critical particles, as expected from dynamical considerations. This appears to be inconsistent with the statement in the last paragraph that because the emitting particles are hotter than black body, they should be smaller than 10 μm. It is not, however, since Fig. 8.4a shows that even large (up to 1000 μm) organic refractory particles have temperatures that are higher than black body, and this is because these large particles do not emit efficiently at their black body temperatures; e.g., Fig. 5.3 shows that 100 μm particles do not have $Q_{abs} \approx 1$ for $\lambda < \pi D$, rather for $\lambda < D/\pi$. Note that the temperature of 2.5 μm astronomical silicate grains at 70 AU from HR 4796A is 103.5 K, while that of 16 μm organic refractory grains is 108.4 K.

The assumptions about the particle properties in the model could also have affected the conclusion about the disk's effective optical depth and consequently that for the collisional lifetime of its emitting particles (see eq. [3.14]). Consider the estimate of $\tau_{eff}(70$ AU) derived from the IHW18 lobe brightness (§8.1.2). Changing the properties of particles in the model would change the estimate of $\tau_{eff}(70$ AU), because of the resultant changes in $P(18.2$ μm,70 AU); e.g., if the disk had

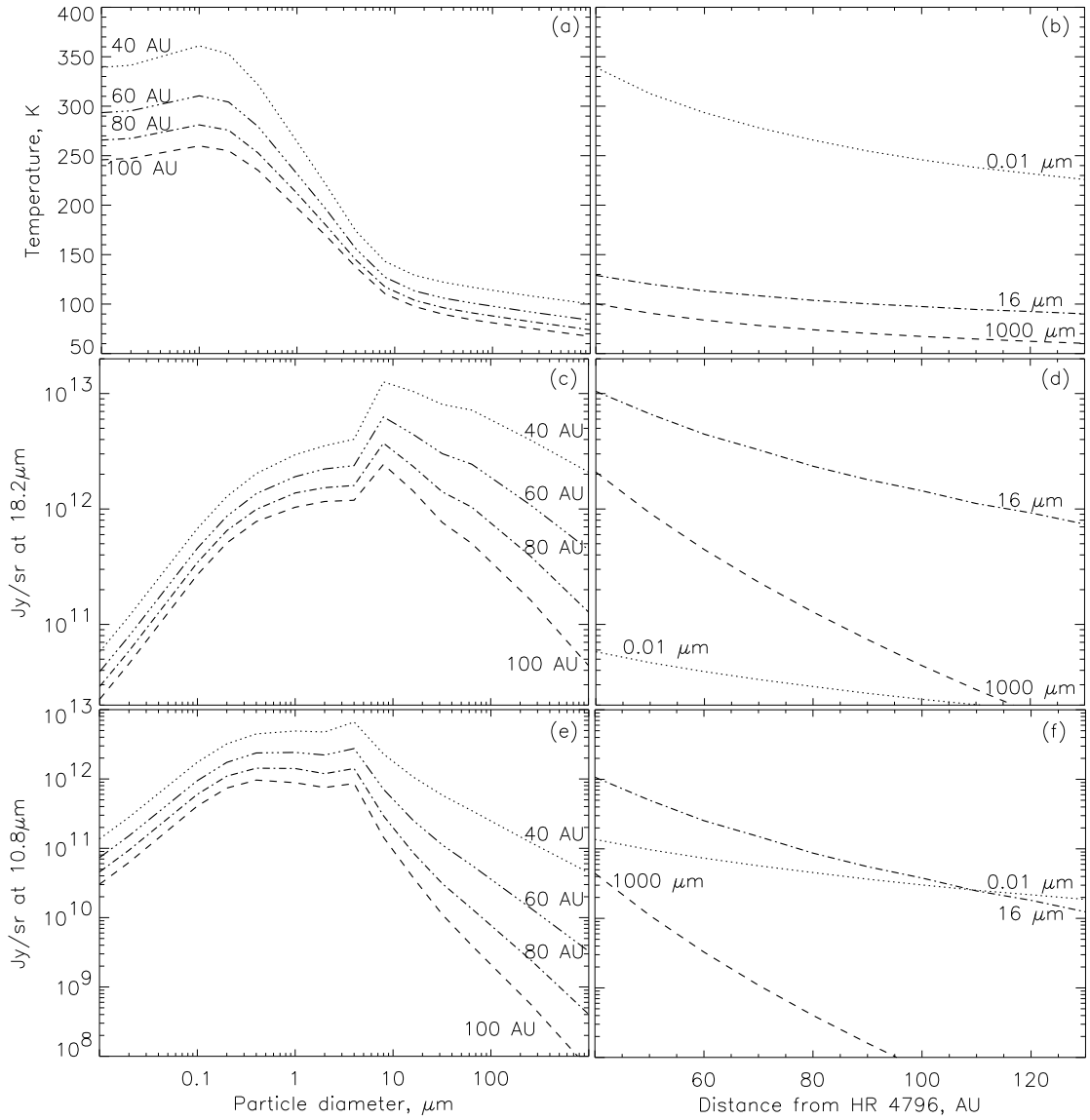

Figure 8.3: The thermal properties of organic refractory Mie spheres in the HR 4796 disk, plotted for particles of different sizes at 40, 60, 80, and 100 AU from HR 4797A (**a**), (**c**), and (**e**), and for 0.01, 16, and 1000 μm diameter particles at different distances from HR 4796A (**b**), (**d**), and (**f**). The temperatures that these particles attain is plotted in (**a**) and (**b**). The contribution of a particle's thermal emission to the flux density received at the Earth per solid angle that its cross-sectional area subtends there, $Q_{abs}(D,\lambda)B_\nu[T(D,r),\lambda]$ (eq. [2.3]), is plotted for observations in the IHW18, 18.2 μm, (**c**) and (**d**), and N, 10.8 μm, (**e**) and (**f**) wavebands.

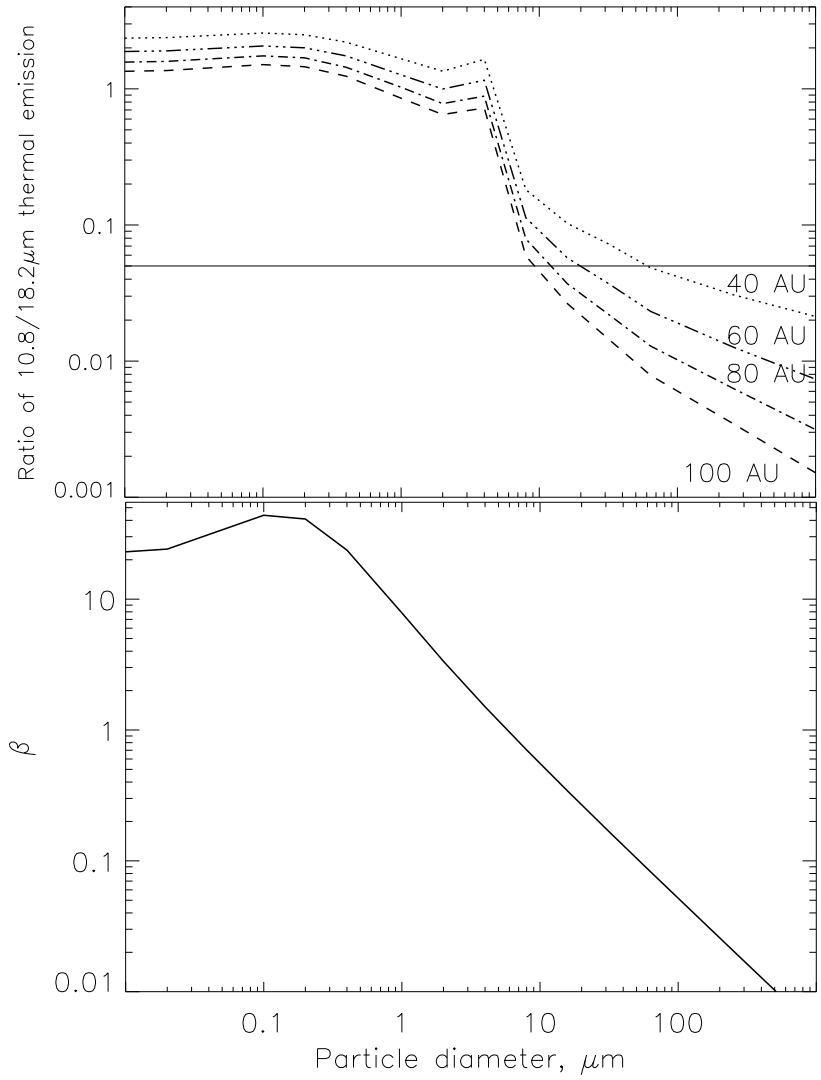

Figure 8.4: Estimate of the dynamical category of the mid-infrared emitting particles in the HR 4796 disk if they are made of organic refractory material. *Top* - The ratio of the thermal emission in the N, 10.8 μm, and IHW18, 18.2 μm, wavebands, of organic refractory Mie spheres of different sizes at 40, 60, 80, and 100 AU from HR 4796A (cf. Fig. 7.4). Assuming the disk's flux densities in the two wavebands to be dominated by the emission of particles at 60-80 AU, the observed ratio of flux densities, $O(0.05)$ (T2000; §7.2.2), can be used to estimate that the disk's emitting particles have $D_{typ} = 12 - 20$ μm. *Bottom* - The ratio, β, of the radiation pressure force to the gravitational force acting on organic refractory Mie spheres of different sizes in the HR 4796 disk (cf. Fig. 8.1). The size estimate implies that the particles have a β between 0.2 and 0.5, i.e., that they are the disk's β critical particles.

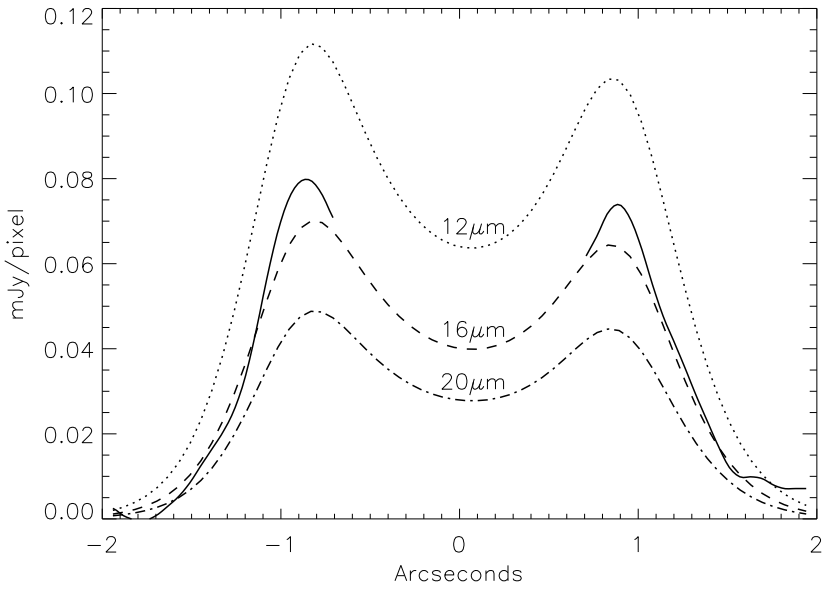

Figure 8.5: Horizontal line-cuts along the plane of the lobes in the N (10.8 μm) band. The observation is shown with a solid line and models with organic refractory Mie spheres with diameters of D_{typ} = 12, 16, and 20 μm are shown with dotted, dashed, and dash-dot lines. This is analagous to Fig. 7.7 which shows the same plot, but for models with astronomical silicate Mie spheres of different sizes.

been modeled using 30-50 μm astronomical silicate particles, more cross-sectional area would have had to have been put in the model for it to give the observed lobe brightness, resulting in a higher effective optical depth. Since for 16 μm organic refractory particles, P(18.2 μm,70 AU)= 3.3×10^{12} Jy/sr, which is just $\sim$ 1.4 times that of the 2.5 μm diameter astronomical silicates (Fig. 7.3c), if organic refractory material had been used in the modeling rather than astronomical silicate, the inferred effective optical depth of the disk would have been smaller by a factor of $\sim$ 1.4, and the collisional lifetime of the emitting particles would have been longer by the same factor (i.e., not much different). It is possible that different optical properties would affect this estimate of τ_{eff}(70 AU) by a greater amount, since P(18.2 μm,70 AU) has the potential to cover a wide range of values; e.g., astronomical silicate Mie spheres that are larger than 0.01 μm imply a possible range of $0.034 - 2.3 \times 10^{12}$ Jy/sr (Fig. 7.3c), while the same range for organic refractory Mie spheres is $0.033 - 4.8 \times 10^{12}$ Jy/sr (Fig. 8.3c). However, given the temperature of the emitting particles inferred from the observed brightness ratio, $\sim 5 \times 10^{-3}$ remains the best estimate for the disk's effective optical depth at 70 AU, and $O(10^4$ years) the best estimate for the emitting particles' collisional lifetime there. A further note of caution is necessary about the inferred collisional lifetime: §3.2.2 assumes collisions between disk particles to be either catastrophic or irrelevant. While this may be appropriate for the disk's larger particles, since these are likely to be solid bodies, collisions between its smaller particles, which may have fluffy bird's nest structures (Gustafson 1994), could be more erosive than destructive.

Thus, both the conclusion about the dynamical category of the disk's emitting particles and, to some extent, the conclusion about their collisional lifetime are sensitive to the assumptions about the particles' composition. Since the particles' composition cannot be determined from just two points on the disk's SED, this really just emphasizes the ambiguity of conclusions drawn in such a way. However, interpretation of the spectrum of the HR 4796 disk emission could be used to reveal properties of its particles. Particles with different properties have different spectral signatures in the mid-IR because the wavelengths at which they emit most efficiently are different (see Figs. 5.2 and 5.3); e.g., the spectrum of the thermal emission of 2.5 μm astronomical silicate particles and that of

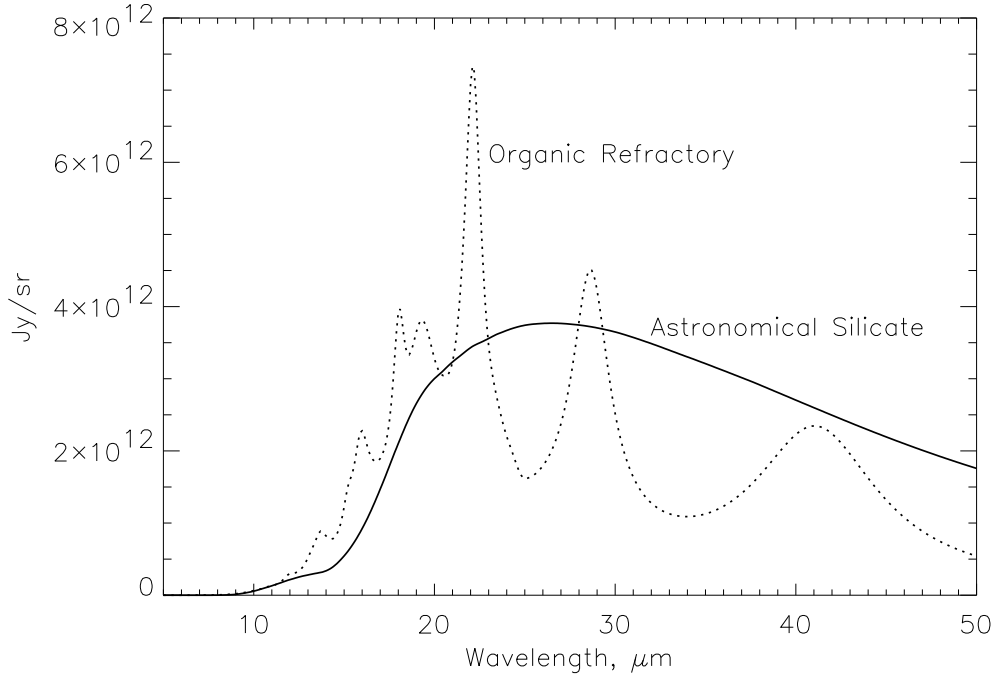

Figure 8.6: Mid-infrared thermal emission spectra of particles at 70 AU from HR 4796A. The solid line depicts 2.5 μm diameter astronomical silicate particles, and the dotted line depicts 16 μm diameter organic refractory particles.

16 μm organic refractory particles at 70 AU from HR 4796A is shown in Fig. 8.6. A spectrum with such well-defined features as those of Fig. 8.6 is not expected, since the observed spectrum contains the emission from a range of particle sizes, and from particles at different distances from the star; however, such a spectrum could be modeled, and this would reveal information not only about the particles' properties, but also about their size distribution. While the spectrum of HR 4796 is not yet available, its SED has been observed (see, e.g., Fig. 6.3), and this would be the starting point of such modeling.

In conclusion, without further study, neither observational nor theoretical considerations can provide a definitive answer as to the dynamics of the mid-IR emitting particles in the HR 4796 disk. However, because of the short collisional lifetime of these particles, it is certain that they are not primordial, and that there are no P-R drag affected particles in the disk. Because of the inferred temperature of the particles, it is most likely that these particles are either β meteoroids or β critical particles. β critical particles are preferred from theoretical considerations, however a disk with mid-IR emitting particles that are on hyperbolic orbits is not an outlandish possibility. Such particles have been inferred from observations of the disks around both β Pictoris (Telesco et al. 1988) and, possibly, HD 141569 (Fisher et al. 2000). The disk around BD+31°643 has also been interpreted as a radiation pressure outflow (Lecavelier des Etangs et al. 1998); however this disk is quite unlike the HR 4796 disk, since it is around a binary star, there is a significant amount of gas in the system, and the disk particles are thought to be created $\sim$ 2300 AU from the star.

8.4 Origin of the Inner Hole

Whatever the size of the emitting particles, analysis of the optical depth of the disk's inner region shows that it is a few hundred times less than that of the outer disk (T2000), and so there must be very few emitting particles in this region. Because this central hole is necessary for the secular perturbation offset asymmetry to be observed (without the hole only the radial offset could

be observed), its physical origin requires attention. Since the existence of small emitting particles in the disk requires the existence of large particles, the question to answer is why there are so many large particles in the outer disk, but so few in the inner disk? Either the physical conditions were such that they were able to form in the outer region, but not in the inner region, or they formed across the whole disk, but those formed in the inner region have since been removed. Rather than discussing the planetary formation process and the stage of the system's evolution (although these are of utmost importance in determining the physics of the disk), this section offers possible dynamical explanations for the removal of the large particles.

If a planetary system did form in the inner region, then a lack of debris material in this region is to be expected, most obviously because much of the debris material that did form there would have been swept up by the growing planets. Also, a lot of the material in the inner region that did not end up accreted onto a planet by the end of the planetary formation process would be ejected from this region due to resonant perturbations from the planetary system (see discussions of resonance overlap and secular resonance in §4.2). For resonant mechanisms to remove all of the remaining material, the system would have to consist of either many planets, or just one planet that is either very large, or on a very eccentric orbit. Radial migration by the planets, however, would allow them to affect a larger fraction of the disk than equations such as equation (4.21) imply. Note that none of these removal mechanisms would cause the inner edge of the disk to have a sharp cut-off in radial distance from the star, rather, since all of these removal mechanisms take longer than a particle's orbital period to take effect, they would cause an inner cut-off in the disk particles' semimajor axes, which causes a sloping radial cut-off (see §7.1.2).

To estimate the orbit of a putative planet at the inner edge of the HR 4796 disk that is causing the cut-off, consider the inner edge of the Kuiper belt, which is located at the **2:3** resonance with Neptune (§4.2.2). By analogy, assuming that the inner cut-off of the disk's large particles occurs at the planet's **2:3** resonance location, and that this cut-off can be described by $a_{min} = 62$ AU, equation (4.19) can be used to estimate that the orbit of the planet has a semimajor axis of

$$a_{pl} = a_{min}[\mathbf{2/3}]^{2/3}, \tag{8.4}$$

giving $a_{pl} = 47$ AU, and an orbital period of ~ 200 years (eq. [3.2]).

8.5 Interpretation of the Residual Structure

So far, no explanation has been offered for the structure of the residuals (what is left after subtracting the model from the observation; see Fig. 8.7). Analogy with the zodiacal cloud implies that there could be a population of warm dust in the inner region that may be unrelated to the cold dust in the outer disk. Indeed, many authors have argued for the existence of such a population (Koerner et al. 1998; Augereau et al. 1999), although their claims do not appear to concur with the observations of T2000 (see Chapter 6). Depending on the perturbers in the inner region, such a population could contain considerable structure. Analysis of the emission from such regions would reveal a great deal about the system's perturbers, however, the detection of this emission would not be easy, since the resolution required to map such small-scale structure is at the limit of current technological capabilities. In addition, such emission is masked by that of both the stellar photosphere and the outer disk, the subtraction of which is unlikely to be perfectly accurate (see Chapter 2).

There may also be residual structure associated with the outer regions of the disk. If there is a planet orbiting HR 4796A close to the inner edge of the disk, then the distribution of large particles in the outer disk would contain structure associated with the planet's gravitational perturbations in addition to the secular perturbations already discussed (Dermott et al. 1994; Malhotra 1996; Dermott et al. 1998; Ward & Hahn 1998). Some of the emitting particles might be trapped in its resonant ring, which would be analogous to the Kuiper belt resonant ring (§4.2.2) rather than the Earth's resonant ring (§4.2.1). Such a ring could be responsible for some of the observed lobe asymmetry. The existence of such a ring would give the inner edge of the disk structure that co-orbits with the planet; i.e., observations of this structure would vary on timescales of $O(200$ years),

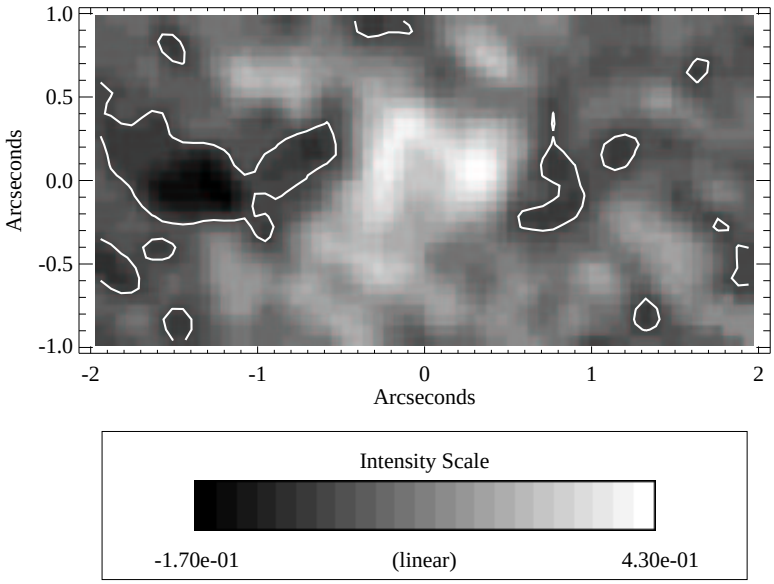

Figure 8.7: Image of the residual IHW18 (18.2 μm) waveband emission from the HR 4796 disk. These residuals are the observed image (Telesco et al. 2000) minus the model image (Wyatt et al. 1999; see Fig. 7.6). The intensity scale is in mJy/pixel, and the contour line is that of zero residual emission.

offering a method of distinguishing between this structure and the large-scale background structure, which would vary on secular timescales of O(1 Myr). The amount of disk material that is trapped in an anolgous Kuiper belt ring, and the structure of that ring, depends on the extent of radial migration of the planet's orbit. The edge-on viewing geometry of the HR 4796 disk makes it more difficult to detect such resonant structure.

CHAPTER 9
CONCLUSION

9.1 Conclusion

This dissertation provides a physical model for the evolution of circumstellar debris disks that is based on our understanding of the physics affecting the evolution of the particles in such disks. The physical processes that are included in this model are those that affect the evolution of the debris disk in the solar system, the zodiacal cloud, but generalized for disks that may be at different evolutionary stages. It was shown how disk particles can be grouped into one of four categories (large, P-R drag affected, β critical, and β meteoroid) depending on the dominant physical processes affecting their evolution, and how the spatial distribution of material in each of these categories is related. The relative proportion of each of these categories in a disk depends on its evolutionary status (and in particular on the disk's density); e.g., the thermal emission from a relatively old (tenuous) disk such as the zodiacal cloud is dominated by emission from its P-R drag affected particles.

This model allows predictions to be made about the evolution of a particular system, but it is always constrained by the initial conditions of that system (i.e., the outcome of the planetary formation process). The outcome of the planetary formation process is not generally known, and it is one of the primary motives behind circumstellar disk observations to infer that outcome. The effect of the gravitational perturbations from a planetary system on the dynamical evolution of a disk's particles was included in the model, and it was shown how the planets cause certain signatures to be imprinted on the disk's structure. The signatures that were discussed are the same as those that are observed in the structure of the zodiacal cloud: an offset center of symmetry, a warp, and asymmetric resonant ring structures co-orbiting with individual planets.

The model can be used to interpret debris disk observations in a manner that can provide quantitative information about the physics of that disk, and in particular about the outcome of the planetary formation process in that system. The necessary modeling techniques were demonstrated by their application to observations of the HR 4796 disk (W99; T2000). This disk provides an important opportunity for studying the planetary formation process, since the system's age, ~ 10 Myr, places it at an evolutionary epoch when any planetary system should be substantially formed. Both the mid-IR and the near-IR emission from this disk has been shown to be concentrated in two lobes, one either side of the star. This indicates that the disk is being observed nearly edge-on, and that its inner region (~ 40 AU in radius, the same size as the solar system) is almost completely devoid of dust. The observations of T2000 show another interesting feature: the mid-IR lobes appear to be of unequal brightness. This dissertation presented a model of the T2000 observations that not only reproduced the large-scale structure of the disk's 18.2 μm emission, but also showed that the lobe brightness asymmetry is to be expected if there is another body orbiting HR 4796A that is on an eccentric orbit, since the long-term effect of the gravitational perturbations from this body would force the center of symmetry of the disk to be offset from the star in a direction away from the pericenter of the body's orbit, thus causing the dust near this forced pericenter to glow; this model was previously presented in W99.

The modeling showed that a forced eccentricity as small as 0.02 is all that is necessary to cause the observed 5% lobe brightness asymmetry. This forced eccentricity could have been caused by perturbations from either the binary companion, HR 4796B, or from an unseen planet orbiting close to the inner edge of the disk. If the eccentricity of the orbit of HR 4796B is larger than 0.13, then a forced eccentricity of 0.02 is to be expected. However, if there is a planet of mass $> 0.1 M_J$

located close to the inner edge of the disk, then the forced eccentricity, and hence the asymmetry, imposed on material in the disk's lobes is controlled by the planet rather than the binary companion. If a forced eccentricity is indeed the cause of the observed lobe asymmetry then observations that constrain the orbit of HR 4796B would help to clarify whether such a planet exists. If the HR 4796 system had no binary companion, a forced eccentricity of 0.02 could have been imposed on the disk by a lone planet with a mass of $> 10 M_{\oplus}$, and an eccentricity of > 0.02 orbiting at 47 AU from HR 4796A.

The statistical significance of the HR 4796 disk's lobe asymmetry in the observations of T2000 is only at the 1.8σ level, however, it is also apparent in the observations of other authors (Koerner et al. 1998; Schneider et al. 1999). Also, it would take one good night on a 10 meter telescope to get a clear observation of the HR 4796 asymmetry. Thus, the signatures of even small mass planets orbiting far from the star that are hiding in circumstellar disks are observable with current technology, and these modeling techniques have the potential to be used to infer the existence of otherwise undetectable planetary systems. This is particularly important, since the direct detection of planets around even nearby stars is well beyond current capabilities (Backman 1998), and indirect detection techniques permit detection only of very massive planets that are close to the star (§1.2; see Fig. 1.1). This could be the only currently available method of detecting terrestrial-mass extrasolar planets.

If there is a massive (e.g., $> 0.1 M_J$) planet close to the inner edge of the disk, then the offset asymmetry would not be the only planetary signature that we would expect to observe in the disk's structure. Many of the disk's particles could be trapped in resonance with that planet, thus forming a resonant ring, and the disk could be warped. Such a resonant ring would give the inner edge of the disk structure that orbits the star with the same orbital period as that of the planet (i.e., ~ 200 years). This structure could be contributing to the observed lobe asymmetry, and may also be present in the residuals of the observation. These possibilities could be explored with further observations and modeling.

Because of the physical nature of the modeling process, it revealed much information about the disk system, and in particular about the dynamic properties of its emitting particles. Assuming the particles to be astronomical silicate Mie spheres, the diameter of the mid-IR emitting particles was estimated to be $D_{typ} = 2-3$ μm. Particles this small have radiation forces that are characterized by $\beta \approx 2$, and so are blown out of the system on hyperbolic orbits on timescales of ~ 370 years (i.e., they are the disk's β meteoroids). However, if the particles had been assumed to be organic refractory Mie spheres, their diameter would have been estimated to be $12 - 20$ μm, with a β of between 0.2 and 0.5, implying that these particles are the disk's β critical particles. From a theoretical point of view, the disk's inferred optical depth, $\tau_{eff}(70 \text{ AU}) \approx 5 \times 10^{-3}$, supports the view that the emitting particles are the disk's β critical particles, however, no firm conclusion about whether the emitting particles are β meteoroids or β critical particles can be reached without further observations and modeling. Other conclusions about the dynamic HR 4796 disk were that, because the HR 4796 disk is very dense, and the collisional lifetime of its emitting particles is $\sim 10^4$ years, these particles cannot be primordial, rather they must be continuously created from a reservoir of larger particles. Also, because the collisional lifetimes of all of the disk's particles are shorter than their P-R drag lifetimes, none of the disk's particles are affected by P-R drag.

Thus, the HR 4796 disk modeling demonstrates the current status of our interpretation of debris disk observations: the complexity of these systems far outstretches the scope of the observations; i.e., there is too little information about these disks to be able to completely infer their physics, rather conclusions are necessarily speculative. This physical model is a step forward, however, since it puts the conclusions on a firm physical basis.

9.2 Further Work

Since the field of imaging debris disk structure is so young, many more disks with resolved structure are likely to be discovered in the coming years. With 10 meter class telescopes such as

Gemini becoming widely available, the quality of these disk observations will be similar to that of the observations described in T2000. Such observations are bound to test the limits of the model for the evolution of debris disks that is described in this dissertation. Many ways have already been discussed to develop the model for the HR 4796 disk, and these are summarized in §9.2.1. Since each disk is unique in that it describes the outcome of the planetary formation process at a different epoch and with different starting conditions, it will test the model in a unique way. Thus, the developments that will be necessary to the theoretical model cannot be predicted, since they will follow the observations. §9.2.2 describes just two debris disks to which this modeling technique can be applied and against which it can be tested. With a better understanding of the evolution of debris disks, and the possibility of indirect detections of terrestrial mass planets, this modeling technique should allow a greater understanding of the formation and evolution of planetary systems.

9.2.1 HR 4796

Several observational tests and model improvements have already been discussed that would provide a clearer understanding of the HR 4796 disk:

- First, more accurate observations of the disk emission at 10 and 18 μm are needed. One good night on a 10 meter telescope (preferably one without an asymmetric PSF like the Keck telescope) would suffice for this. This would allow the following:
  - to unconditionally confirm the lobe asymmetry and its magnitude;
  - to confirm a radial offset asymmetry for the lobes that agrees with the lobe asymmetry;
  - to test for the presence of a disk warp, which could be modeled using techniques similar to those described in this disseration (and W99);
  - and to determine the residuals with sufficient accuracy for them to be modeled, possibly as resonant structure associated with a planet at the inner edge of the disk.

  Residual structure associated with a planet at the inner edge of the disk would co-orbit with the planet. If the lobe asymmetry, even in part, was caused by such resonant structure, its magnitude would vary with a period of $\sim$ 200 years. Subsequent observations at intervals of $\sim$ 3 years would be able to ascertain whether the residual structure is truly associated with an orbiting planet, since the structure would have moved by one pixel on the image in this timescale.

- Either new observations, or careful study of archived observations, of the separation and position angle of HR 4796B relative to HR 4796A are needed to determine the orbit of this binary system. This would allow a much more unambiguous interpretation of the lobe asymmetry, and of any potential warp.

- The model needs to include a distribution of particle sizes, and a better model for the optical properties of the particles (including their scattering properties). Possible physical models for these were discussed in this dissertation. These can be constrained using the disk's SED (see, e.g., Augereau et al. 1999) and its mid-IR spectrum. This will allow a better understanding of the dynamics of the emitting particles, and is vital if we are to constrain the model for the evolution of debris disks. Ideally, a disk model should be able to explain images and spectra at all wavelengths simultaneously.

- With a better understanding of the dynamics of the emitting particles, it may be necessary to expand the theoretical model to model the dynamics of particles that are on hyperbolic or highly eccentric orbits. The theory for this has already been described in the dissertation, however, it has not yet been translated into the realm of the modeling.

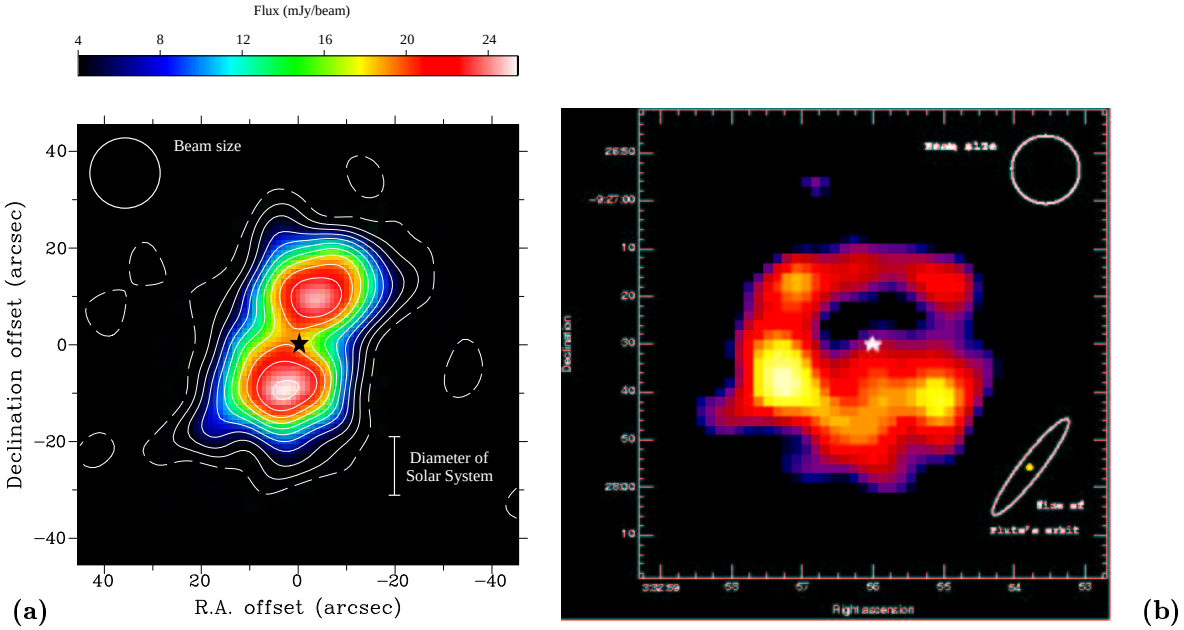

Figure 9.1: Submillimeter, 850 μm, images of the disks of dust around (**a**) Fomalhaut (Holland et al. 1998) and (**b**) ϵ Eridani (Greaves et al. 1998).

9.2.2 Other Disks

9.2.2.1 Fomalhaut

A double-lobed feature similar to that observed in the HR 4796 disk has also been observed in the disk around the star Fomalhaut (Holland et al. 1998; see Fig. 9.1a). A similar explanation (planetary formation) has been proposed for its origin (Holland et al. 1998). The brightnesses of the Fomalhaut disk's lobes also appear to be asymmetric (Holland et al. 1998), but the statistical significance of this asymmetry is low. Fomalhaut is a wide visual binary system. Gliese 879 is Fomalhaut's common proper motion companion (Barrado Y Navascués et al. 1997); the two stars are separated by $\sim 2°$, which corresponds to a projected separation of O(55,000 AU) at 7.7 pc. At such a distance, the forced eccentricity imposed on the disk by the binary star is insignificant (see eq. [4.16]). A secular perturbation offset asymmetry in this disk would be expected only if there is a planet in the disk that has a non-circular orbit. This disk could be modeled using the same techniques that were used to model the HR 4796 disk.

9.2.2.2 ϵ Eridani

ϵ Eridani is one of the prototype debris disks. It was imaged at 850 μm by SCUBA at JCMT, and these observations show that the disk's structure is clumpy (Greaves et al. 1998; see Fig. 9.1b). In fact, the observations seem to show the tri-lobed structure expected from an analogue Kuiper belt the particles of which are trapped in the 1:2 and 2:3 resonances of a planet located at the inner edge of the disk (see §4.2.2). Modeling of this structure will reveal whether this is a plausible explanation for the observed structure. It would be very exciting if resonant rings were the predominantly observable structures of some exosolar systems, since such rings would be good indirect indications of extrasolar planets.

REFERENCES

Artymowicz, P., & Lubow, S. H. 1994, ApJ, 421, 651

Artymowicz, P. 1997, Annu. Rev. Earth Planet. Sci., 25, 175

Artymowicz, P., & Clampin, M. 1997, ApJ, 490, 863

Augereau, J. C., Lagrange, A. M., Mouillet, D., Papaloizou, J. C. B., & Grorod, P. A. 1999, A&A, 348, 557

Aumann, H. H. 1985, PASP, 97, 885

Aumann, H. H., Gillett, F. C., Beichman, C. A., De Jong, T., Houck, J. R., Low, F. J., Neugebauer, G., Walker, R. G., & Wesselius, P. R. 1984, ApJ, 278, L23

Backman, D. E. 1998, in Exozodiacal Dust Workshop Conference Proceedings, eds. D. E. Backman, L. J. Caroff, S. A. Sandford, & D. H. Wooden (NASA/CP-1998-10155), 13

Backman, D. E., & Paresce, F. 1993, in Protostars & Planets III, eds E. H. Levy, & J. Lunine (Tucson: Univ. Ariz. Press), 1253

Backman, D. E., Dasgupta, A., & Stencel, R. E. 1995, ApJ, 450, L35

Barrado Y Navascués, D., Stauffer, J. R., Hartmann, L., & Balachandran, S. C. 1997, ApJ, 475, 313

Barrado Y Navascués, D., Stauffer, J. R., Song, I., & Caillault, J.-P. 1999, ApJ, 520, L123

Beaugé, C., & Ferraz-Mello, S. 1994, Icarus, 110, 239

Beckwith, S. V. W. 1999, to appear in The Physics of Star Formation and Early Evolution II, eds. C. J. Lada, & N. D. Kylafis (astro-ph/9905003)

Beckwith, S. V. W., Henning, T., & Nakagawa, Y. 1999, to appear in Protostars & Planets IV (astro-ph/9902241)

Beckwith, S. V. W., & Sargent, A. I. 1996, Nature, 383, 139

Beckwith, S. V. W., Sargent, A. I., Chini, R. S., & Gusten, R. 1990,AJ, 99, 924

Beichman, C. A. 1996, A Road Map for the Exploration of Neighboring Planetary Systems (ExNPS) (JPL Publ. 96-22, Tech. Rep., Pasadena, CA)

Berkhuijsen, E. M., Halsam, C. G. T., & Salter, C. J. 1971, A&A, 14, 252

Black, D. C. 1997, ApJ, 490, L171

Blum, J., Wurm, G., Poppe, T., & Heim, L.-O. 1999, in Laboratory Astrophysics and Space Research, Astrophysics and Space Science Library, eds. P. Ehrenfreund, K. Krafft, H. Kochan, & V. Pirronello (Dordrecht: Kluwer), 236, 399

Bohren, C. F., & Huffman, D. R. 1983, Absorption and Scattering of Light by Small Particles (New York: Wiley)

Boss, A. P. 1995, Science, 267, 360

Bowell, E. 1996, Asteroid Orbital Elements Database (Lowell Observatory)

Brouwer, D., & Clemence, G. M. 1961, Methods of Celestial Mechanics (New York: Academic Press)

Burns, J. A., Lamy, P. L., & Soter, S. 1979, Icarus, 40, 1

Burrows, C. J., Stapelfeldt, K. R., Watson, A. M., Krist, J. E., Ballester, G. E., Clarke, J. T., Crisp, D., Gallagher, J. S. III, Griffiths, R. E., Hester, J. J., Hoessel, J. G., Holtzman, J. A., Mould, J. R., Scowen, P. A., Trauger, J. T., Westphal, J. A. 1996, ApJ, 473, 437

Cameron, A. G. W. 1997, Icarus, 126, 126

Clarke, C. J., & Pringle, J. E. 1991, MNRAS, 249, 588

de Geus, E. J., de Zeeuw, P. T., & Lub, J. 1989, A&A, 216, 44

Dent, W. R. F., Matthews, H. E., & Ward-Thompson, D. 1998, MNRAS, 301, 1049

Dermott, S. F., Gomes, R. S., Durda, D. D., Gustafson, B. Å. S., Jayaraman, S., Xu, Y. L., & Nicholson, P. D. 1992, in Chaos, Resonance and Collective Dynamical Phenomena in the Solar System, ed. S. Ferraz-Mello (Dordrecht: Kluwer), IAU Symposium, 152, 333

Dermott, S. F., Grogan, K., Gustafson, B. Å. S., Holmes, E. K., Jayaraman, S., & Wyatt, M. C. 2000, in Interplanetary Dust, eds. E. Grun, B. Å. S. Gustafson, S. F. Dermott, & H. Fechtig (Tucson: Univ. Ariz. Press), in press

Dermott, S. F., Grogan, K., Holmes, E. K., & Kortenkamp, S. 1999, in Formation and Evolution of Solids in Space, eds. J. M. Greenberg, & A. Li (Dordrecht: Kluwer), 565

Dermott, S. F., Grogan, K., Holmes, E. K., & Wyatt, M. C. 1998, in Exozodiacal Dust Workshop Conference Proceedings, eds. D. E. Backman, L. J. Caroff, S. A. Sandford, & D. H. Wooden (NASA/CP-1998-10155), 59

Dermott, S. F., Jayaraman, S., Xu, Y. L., Grogan, K., & Gustafson, B. Å. S. 1996, in Unveiling the Cosmic Infrared Background, ed. E. Dwek (New York: AIP), 25

Dermott, S. F., Jayaraman, S., Xu, Y. L., Gustafson, B. Å. S., & Liou, J. C. 1994, Nature, 369, 719

Dermott, S. F., Malhotra, R., & Murray, C. D. 1988, Icarus, 76, 295

Dermott, S. F., & Murray, C. D. 1983, Nature, 301, 201

Dermott, S. F., & Nicholson, P. D. 1986, Nature, 319, 115

Dermott, S. F., Nicholson, P. D., Burns, J. A., & Houck, J. R. 1984, Nature, 312, 505

Dermott, S. F., Nicholson, P. D., Burns, J. A., & Houck, J. R. 1985, in Properties and Interactions of Interplanetary Dust, eds. R. H. Giese, & P. Lamy (Dordrecht: Reidel), 395

Dohnanyi, J. S. 1969, J. Geophys. Res., 74, 2531

Dominik, C., & Tielens, A. G. G. M. 1997, ApJ, 480, 647

Draine, B. T., & Lee, H. M. 1984, ApJ, 285, 89

Duncan, M., Quinn, T., & Tremaine, S. 1989, Icarus, 82, 402

Dunkin, S. K., Barlow, M. J., & Ryan, S. G. 1997, MNRAS, 286, 604

Durda, D. D., & Dermott, S. F. 1997, Icarus, 130, 140

Durda, D. D., Greenberg, R., & Jedicke, R. 1998, Icarus, 135, 431

Egger, R. J., & Aschenbach, B. 1995, A&A, 294, L25

Fajardo-Acosta, S. B., Telesco, C. M., & Knacke, R. F. 1993, ApJ, 417, L33

Farinella, P., Vokrouhlicky, D., & Hartmann, W. K. 1998, Icarus, 132, 378

Ferlet, R. 1999, A&A Rev., 9, 153

Fernández, J. A., & Ip, W.-H. 1984, Icarus, 58, 109

Fisher, R. S., Telesco, C. M., Piña, R. K., Knacke, R. F., & Wyatt, M. C. submitted, ApJ, 2000

Gatewood, G. 1987, AJ, 94, 213

Gerbaldi, M., Faraggiana, R., Burnage, R., Delmas, F., Gómez, A. E., & Grenier, S. 1999, A&AS, 137, 273

Gold, T. 1975, Icarus, 25, 489

Goldreich, P., & Tremaine, S. 1980, ApJ, 241, 425

Gomes, R. S. 1997a, AJ, 114, 396

Gomes, R. S. 1997b, AJ, 114, 2166

Gonczi, R., Froeschle, Ch., & Froeschle, C. 1982, Icarus, 51, 633

Gorkavyi, N. N., Ozernoy, L. M., Mather, J. C., & Taidakova, T. 1997, ApJ, 488, 268

Greaves, J. S., Holland, W. S., Moriarty-Schieven, G., Jenness, T., Dent, W. R. F., Zuckerman, B., McCarthy, C., Webb, R. A., Butner, H. M., Gear, W. K., & Walker, H. J. 1998, ApJ, 506, L133

Greaves, J. S., Mannings, V., & Holland, W. S. submitted, Icarus, 1999

Greenberg, J. M. 1998, A&A, 330, 375

Greenberg, J. M., & Gustafson, B. Å. S. 1981, A&A, 93, 35

Greenberg, J. M., & Hage, J. I. 1990, ApJ, 361, 260

Grogan, K., Dermott, S. F., Durda, D. D. submitted, Icarus, 2000

Grogan, K., Dermott, S. F., & Gustafson, B. Å. S. 1996, ApJ, 472, 812

Grogan, K., Dermott, S. F., Jayaraman, S., & Xu, Y. L. 1997, Planet. Space Sci., 45, 1657

Grün, E., Zook, H. A., Fechtig, H., & Giese, R. H. 1985, Icarus, 62, 244

Gurnett, D. A., Ansher, J. A., Kurth, W. S., & Granroth, L. J. 1997, Geo. Res. Lett., 24, 3125

Gustafson, B. Å. S. 1994, Annu. Rev. Earth Planet. Sci., 22, 553

Hage, J. I., & Greenberg, J. M. 1990, ApJ, 361, 251

Hahn, J. M., & Malhotra, R. 1999, AJ, 117, 3041

Hayashi, C. 1981, Prog. Theor. Phys. Suppl., 70, 35

Henning, Th., & Stognienko, R. 1996, A&A, 311, 291

Henry, G. W., Marcy, G. W., Butler, R. P., & Vogt, S. S. 2000, ApJ, in press

Hirayama, K. 1918, AJ, 31, 185

Holland, W. S., Greaves, J. S., Zuckerman, B., Webb, R. A., McCarthy, C., Coulson, I. M., Walther, D. M., Dent, W. R. F., Gear, W. K., & Robson, I. 1998, Nature, 392, 788

Ishiguro, M. 1999, December 8, Zodiacal Light, http://zodi.planet.sci.kobe-u.ac.jp/~ishiguro

Jackson, A. A., & Zook, H. A. 1989, Nature, 337, 629

Jayaraman, S., & Dermott, S. F. submitted, Icarus, 2000

Jayawardhana, R., Fisher, R. S., Hartmann, L., Telesco, C. M., Piña, R. K., & Fazio, G. 1998, ApJ, 503, L79

Jayawardhana, R., Hartmann, L., Fazio, G., Fisher, R. S., Telesco, C. M., & Piña, R. K. 1999, ApJ, 521, L129

Jewitt, D. C. 1999, AREPS, in press

Jura, M. 1991, ApJ, 383, L79

Jura, M., Ghez, A. M., White, R. J., McCarthy, D. W., Smith, R. C., & Martin, P. G. 1995, ApJ, 445, 451

Jura, M., Malkan, M., White, R., Telesco, C. M., Fisher, R. S., & Piña, R. K. 1998, ApJ, 505, 897

Jura, M., Zuckerman, B., Becklin, E. E., & Smith, R. C. 1993, ApJ, 418, L37

Kalas, P. 1998, Science, 281, 182

Kalas, P., & Jewitt, D. C. 1995, AJ, 110, 794

Kelsall, T., Weiland, J. L., Franz, B. A., Reach, W. T., Arendt, R. G., Dwek, R., Freudenreich, H. T., Hauser, M. G., Moseley, S. H., Odegard, N. P., Silverberg, R. F., & Wright, E. L. 1998, ApJ, 508, 44

Kenyon, S. J., & Hartmann, L. W. 1987, ApJ, 323, 714

Kenyon, S. J., & Luu, J. X. 1999, AJ, 118, 1101

Kenyon, S. J., Wood, K., Whitney, B. A., & Wolff, M. J. 1999, ApJ, 524, L119

Kessler, D. J. 1981, Icarus, 48, 39

Kimura, H., & Mann, I. 1998, ApJ, 499, 454

Kirkwood, D. 1876, On the Distribution of the Asteroids (Salem, MA: Salem Press)

Koerner, D. W., Ressler, M. E., Werner, M. W., & Backman, D. E. 1998, ApJ, 503, L83

Kortenkamp, S. J., & Dermott, S. F. 1998, Icarus, 135, 469

Lachaume, R., Dominik, C., Lanz, T., & Habing, H. J. 1999, A&A, 348, 897

Lagrange, A.-M., Ferlet, R., & Vidal-Madjar, A. 1987, A&A, 173, 289

Laor, A., & Draine, B. T. 1993, ApJ, 402, 441

Lazzaro, D., Sicardy, B., Roques, F., Greenberg, R. 1994, Icarus, 108, 59

Lecar, M., & Franklin, F. 1997, Icarus, 129, 134

Lecavelier des Etangs, A., Deleuil, M., Vidal-Madjar, A., Ferlet, R., Nitschelm, C., 1995, A&A, 299, 557

Lecavelier des Etangs, A., Vidal-Madjar, & Ferlet, R. 1998, A&A, 339, 477

Leinert, C., & Grün, E. 1990, in Space and Solar Physics, Vol. 20, Physics and Chemistry in Space: Physics of the Inner Heliosphere I, eds. R. Schween, & E. Marsch (Berlin: Springer), 207

Leisawitz, D., Bash, F. N., & Thaddeus, P. 1989, ApJS, 70, 731

Levison, H. F., & Duncan, M. J. 1997, Icarus, 127, 13

Li, A., & Greenberg, J. M. 1997, A&A, 323, 566

Li, A., & Greenberg, J. M. 1998, A&A, 331, 291

Li, D. N. C., & Papaloizou, J. C. B. 1979, MNRAS, 186, 799

Liou, J. C. 1993, Ph.D. Thesis, Univ. Florida

Liou, J. C., Dermott, S. F., & Xu, Y. L. 1995, Planet. Space Sci., 43, 717

Liou, J. C., & Zook, H. A. 1999, AJ, 118, 580

Liou, J. C., Zook, H. A., & Dermott, S. F. 1996, Icarus, 124, 429

Liseau, R. 1999, A&A, 348, 133

Lissauer, J. J. 1993, ARA&A, 31, 129

Love, S. G., & Brownlee, D. E. 1993, Science, 262, 550

Low, F. J., Beintema, D. A., Gautier, T. N., Gillet, F. C., Beichman, C. A., Neugebauer, G., Young, E., Aumann, H. H., Rowan-Robinson, M., Soifer, B. T., Walker, R. G., & Wesselius, P. R. 1984, ApJ, 278, L19

Malhotra, R. 1995, AJ, 110, 420

Malhotra, R. 1996, AJ, 111, 504

Mannings, V., & Barlow, M. J. 1998, ApJ, 497, 330

Marcy, G. W., & Butler, R. P. 1998, ARA&A, 36, 57

Marcy, G. W., Butler, R. P., Vogt, S. S., & Fischer, D. 1999, December 8, Discovery of Extrasolar Planets, http://cannon.sfsu.edu/~gmarcy/planetsearch

Mayor, M., & Queloz, D. 1995, Nature, 378, 355

Mouillet, D., Lagrange, A.-M., Beuzit, J.-L., & Renaud, N. 1997, A&A, 324, 1083

Mouillet, D., Larwood, J. D., Papaloizou, J. C. B., & Lagrange, A. M. 1997, MNRAS, 292, 896

Murray, C. D., & Dermott, S. F. 1999, Solar System Dynamics (Cambridge: Cambridge University Press)

Padgett, D. L., Brandner, W., Stapelfeldt, K. R., Strom, S. E., Terebey, S., & Koerner, D. 1999, AJ, 117, 1490

Pantin, E., Lagage, P. O., & Artymowicz, P. 1997, A&A, 327, 1123

Papaloizou, J. C. B., & Terquem, C. 1999, ApJ, 521, 823

Pollack, J. B., Hollenbach, D., Beckwith, S. V. W., Simonelli, D. P., Roush, T., & Fong, W. 1994, ApJ, 421, 615

Reach, W. T., Franz, B. A., Weiland, J. L., Hauser, M. G., Kelsall, T. N., Wright, E. L., Rawley, G., Stemwedel, S. W., & Spiesman, W. J. 1995, Nature, 374, 521

Roques, F., Scholl, H., Sicardy, B., & Smith, B. A. 1994, Icarus, 108, 37

Schneider, G., Smith, B. A., Becklin, E. E., Koerner, D. W., Meier, R., Hines, D. C., Lowrance, P. J., Terrile, R. J., Thompson, R. I., & Rieke, M. 1999, ApJ, 513, L127

Schultz, A., & Heap, S. 1998, January, 3, Astronomers Have Found a New Twist in a Suspected Protoplanetary Disk, http://oposite.stsci.edu/pubinfo/pr/1998/03/

Shu, F. H., Adams, F. C., & Lizano, S. 1987, ARA&A, 25, 23

Shu, F. H., Najita, J., Galli, D., Ostricker, E., & Lizano, S. 1993, in Protostars & Planets III, eds E. H. Levy, & J. Lunine (Tucson: Univ. Ariz. Press), 3

Sitko, M. L., Grady, C. A., Lynch, D. K., Russell, R. W., & Hanner, M. S. 1999, ApJ, 510, 408

Skinner, C. J., Sylvester, R. J., Graham, J. R., Barlow, M. J., Meixner, M., Keto, E., Arens, J. F., & Jernigan, J. G. 1995, ApJ, 444, 861

Smith, B. A., & Terrile, R. J. 1984, Science, 226, 1421

Soderblom, D. R., King, J. R., Siess, L., Noll, K. S., Gilmore, D. M., Henry, T. J., Nelan, E., Burrows, C. J., Brown, R. A., Perryman, M. A. C., Benedict, G. F., McArthur, B. J., Franz, O. G., Wasserman, L. H., Jones, B. F., Latham, D. W., Torres, G., & Stefanik, R. P. 1998, ApJ, 498, 385

Stauffer, J. R., Hartmann, L. W., & Barrado Y Navascués, B. 1995, ApJ, 454, 910

Stern, S. A. 1995, AJ, 110, 856

Stern, S. A., & Colwell, J. E. 1997, ApJ, 490, 879

Strom, K. M., Newton, G.,& Strom, S. E. 1989, Ap&SS, 71, 183S

Sykes, M. V., Lebofsky, L. A., Hunten, D. M., & Low, F. J. 1986, Science, 232, 1115

Sykes, M. V. 1990, Icarus, 84, 267

Sylvester, R. J., Skinner, C. J., & Barlow, M. J. 1997, MNRAS, 289, 831

Sylvester, R., J., Skinner, C. J., Barlow, M. J., & Mannings, V. 1996, MNRAS, 279, 915

Telesco, C. M., Decher, R., Becklin, E. E., & Wolstencroft, R. D. 1988, Nature, 335, 51

Telesco, C. M., Fisher, R. S., Piña, R. K., Knacke, R. F., Dermott, S. F., Wyatt, M. C., Grogan, K., Holmes, E. K., Ghez, A. M., Prato, L. A., Hartmann, L. W., & Jayawardhana, R. 2000, ApJ, in press

Telesco, C. M., & Knacke, R. F. 1991, ApJ, 372, L29

Trilling, D. E., Benz, W., Guillot, T., Lunin, J. I., Hubbard, W. B., & Burrows, A. 1998, ApJ, 500, 428

Trilling, D. E., & Brown, R. H. 1998, Nature, 395, 775

Vedder, J. D. 1998, Icarus, 131, 283

Venn, K. A., & Lambert, D. L. 1990, ApJ, 363, 234

Walker, H. J., & Wolstencroft, R. D. 1988, PASP, 100, 1509

Ward, W. R., & Hahn, J. M. 1998, ApJ, 116, 489

Webb, R. A., Zuckerman, B., Platais, I., Patience, J., White, R. J., Schwartz, M. J., & McCarthy, C. 1999, ApJ, 512, L63

Wehry, A., & Mann, I. 1999, A&A, 341, 296

Weidenschilling, S. J., & Cuzzi, J. N. 1993, in Protostars & Planets III, eds. E. H. Levy, & J. I. Lunine (Tucson: Univ. Ariz. Press), 1031

Weidenschilling, S. J., & Jackson, A. A. 1993, Icarus, 104, 244

Wetherill, G. W. 1980, ARA&A, 18, 77

Wisdom, J. 1980, AJ, 85, 1122

Wisdom, J. 1982, AJ, 87, 577

Wolszczan, A., & Frail, D. A. 1992, Nature, 355, 145

Woolf, N., & Angel, J. R. 1998, ARA&A, 36, 507

Wyatt, M. C., Dermott, S. F., Telesco, C. M., Fisher, R. S., Grogan, K., Holmes, E. K., & Piña, R. K. 1999, ApJ, in press

Xu, Y. L., & Gustafson, B. Å. S. 1999, ApJ, 513, 894

Yoshioka, S., & Ikeuchi, S. 1990, ApJ, 360, 352

BIOGRAPHICAL SKETCH

Mark Wyatt was born 15 November 1972 in Rainham, a town in Kent, England. He grew up mostly in Bath, where he moved in 1979, and where he attended school from age 7 to 18. In 1991 he went up to Peterhouse College, Cambridge University, to read Engineering, and graduated with a first class degree in 1994. After spending a year in Barranquilla, Colombia, he went to Queen Mary and Westfield College, University of London, to study for an M.Sc. in Astrophysics, which he was awarded with distinction. He then spent four months working as a Human Resources Analyst for J. P. Morgan in London before moving to Gainesville, Florida, to study for a Ph.D. in Astronomy under the tutelage of Dr. Stan Dermott. Once the Ph.D. is completed he will return to the UK to continue with his research as a postdoctoral fellow at the University of Edinburgh. He is getting married in July 2000 to Maxine Neill, whom he met while at Peterhouse.